THE DESIGN OF LOW POWER ULTRA-WIDEBAND TRANSCEIVERS

Wang Lei

NATIONAL UNIVERSITY OF SINGAPORE

2013

THE DESIGN OF LOW POWER ULTRA-WIDEBAND TRANSCEIVERS

Wang Lei

(*B. Sci, Beijing Technology and Business University, China*)

(*M. Eng, Tsinghua University, China*)

A THESIS SUBMITTED

FOR THE DEGREE OF DOCTOR OF PHILOSOPHY

DEPARTMENT OF ELECTRICAL AND COMPUTER ENGINEERING

NATIONAL UNIVERSITY OF SINGAPORE

2013

DECLARATION

I hereby declare that the thesis is my original work and it has been written by me in its entirety. I have duly acknowledged all the sources of information which have been used in the thesis.

This thesis has also not been submitted for any degree in any university previously.

_____

Wang Lei

15 Aug. 2013

ACKNOWLEDGEMENT

TABLE OF CONTENTS

SUMMARY

The last decade has witnessed a tremendous growth in wireless communications. Among various types of wireless transceivers, the Impulse Radio ultra-wideband (IR UWB) transceiver offers exciting opportunities due to its amenability to fully digital implementation and duty cycling. Because of its digital pulse like nature, IR UWB can benefit from the scalability of CMOS technology and the tremendous digital signal processing power available. In this thesis, we will present three works that are related to different aspects of UWB. In the first work, we will present a sub 1 GHz on-off keying (OOK) UWB transceiver based on threshold detection targeting for low data rate energy efficient wireless communication. In the second work, a UWB beamforming transmitter is proposed in view of the voltage headroom reduction due to device downscaling. In the third work, a UWB beamforming receiver is proposed. With beamforming, much efficient energy could be achieved by directing the transmitter or receiver power in the desired direction.

The sub 1 GHz UWB transceiver was implemented in standard 0.35 μm CMOS technology. Due to the digital intensive architecture proposed, the transceiver achieves high energy efficiency of 100 pJ/bit and 600 pJ/bit during transmitting and receiving, respectively. The implemented transceiver can achieve BER smaller than 0.1% with communicating range less than 27 cm.

The 3-5 GHz UWB beamforming transmitter is implemented in 0.13 μm CMOS. Through the proposed vernier delay line and delta-sigma delay locked loop ($\Delta\Sigma$ DLL) based calibration, we achieve delay resolution of 10 ps, which is 10 times smaller than the currently reported state-of-the-art. Similarly,

through digital intensive architecture, and careful optimization of various paths, the resulting beamformer only consumes 9.6 mW which is also 10 times smaller than other reported UWB beamformer.

The 0.1-10 GHz UWB beamforming receiver is implemented in 65 nm CMOS. Post layout simulation results show that we could achieve 225 ps delay range with 1.44 mm^2 area through the proposed Q compensated approach. This area is seven times smaller than the other UWB beamforming receiver based on passive LC true time delay.

LIST OF FIGURES

LIST OF TABLES

LIST OF ABBREVIATIONS

4G	Fourth Generation
BER	Bit Error Rate
CMOS	Complementary Metal-Oxide Semiconductor
DAC	Digital to Analog Converters
DCO	Digital Controlled Oscillator
DLL	Delay Locked Loop
DSP	Digital Signal Processing
EEG	Electroencephalogram
EIRP	Effective Isotropically Radiated Power
FCC	Federal Communications Commission
FS	Free Space
FSM	Finite State Machine
IC	Integrated Circuit
IF	Intermediate Frequency
IM3	Third-order Inter-Modulation
IP3	Third-order Intercept Point
IR UWB	Impulse Radio UWB
LO	Local Oscillator
LFSR	Linear Feedback Shift Register
LTE	Long-Term Evolution

MICS	Medical Implant Communications Service
OFDM	Orthogonal Frequency Division Multiplexing
OOK	On-Off Keying
P1dB	1-dB Compression Point
PA	Power Amplifier
PD	Phase Detector
PLL	Phase Locked Loop
PSDC	Power Spectral Density Calibration
PVT	Process, Voltage and Temperature
RF	Radio Frequency
SAR	Successive Approximation Register
SNR	Signal to Noise Ratio
SPI	Serial-Peripheral Interface
UWB	Ultra Wide Band
VCDL	Voltage Controlled Delay Line
VCO	Voltage Controlled Oscillator
WBAN	Wireless Body Area Network
WLAN	Wireless Local Area Networks
WPAN	Wireless Personal Area Network
WSN	Wireless Sensor Network

CHAPTER 1 INTRODUCTION

1.1 Background

1.1.1 The Attractiveness of IR UWB Transceiver

The customers' demand for ubiquitous wireless connectivity has opened up a new wave of challenges and opportunities for Radio Frequency (RF) integrated circuit design. In addition to high throughput Wireless Local Area Networks (WLAN), attention is now also being focused on lower power and lower data rate, indoor communications which mainly include home automation, smart toys, and medical cares [1], [2]. For example, for wireless body area network (WBAN) used for biomedical applications, the sensor nodes need to constantly collect, process, store and transmit the data to the servers. This places a stringent power requirement on the employed transceiver.

For sensor node application, Bluetooth and ZigBee with well-developed transceiver and protocol are commonly employed. However, their conventional narrow band RF architecture limits the achievable power consumption to tens of mW. Recently, transceiver based on medical implant communications service (MICS) band has also been developed [3]. Due to the narrow spectrum allocated (401 - 405 MHz), they are normally used for applications with data rate lower than a few 100 kbps. For these narrow band approaches, a large portion of power is consumed by frequency translation and synthesis. If the continuous sinusoidal waveform could be replaced by pulses, up/down converters can be eliminated and result in carrierless architecture.

Ultra-wideband (UWB) has emerged as a promising candidate for low power sensor node application since the Federal Communications Commission (FCC) allocated 8 GHz bandwidth (0 - 960 MHz and 3.1 - 10.6 GHz, as shown in Figure 1.1) for such application, where any transmitting signal with its fractional bandwidth greater than 0.2 or its -10 dB bandwidth greater than or equal to 500 MHz can be classified as UWB [4]. The fractional bandwidth is defined as $2(f_H - f_L)/(f_H + f_L)$, where f_H is the spectrum upper -10 dB frequency and f_L is the lower -10 dB frequency. The maximum power level is -41 dBm/MHz.
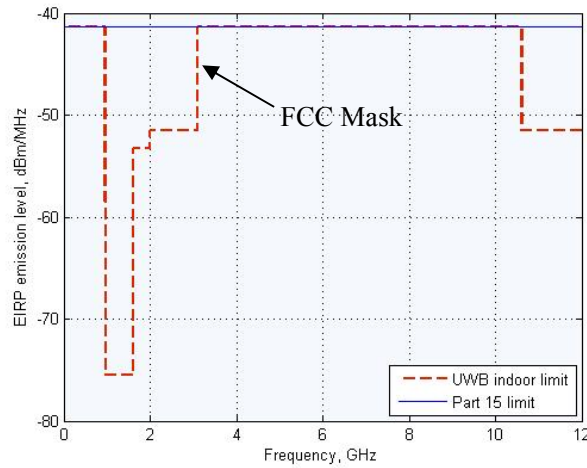
Figure 1.1. FCC Mask for UWB regulation.

There are two competing UWB standards, i.e. the Orthogonal Frequency Division Multiplexing (OFDM) standard and the Impulse Radio UWB (IR UWB) standard. OFDM standard has been adopted by Wi-media alliance for implementing high data rate communication. OFDM system divides the entire 7.5 GHz (3.1-10.6 GHz) bandwidth to sub bands with each bandwidth slightly larger than 500 MHz and performs frequency hopping, like narrow band

approach. Therefore, its complexity and PA linearity requirement do not lead to energy efficient implementation.

On the other hand, IR UWB adopts short pulses, instead of continuous sinusoidal waveform. This carrierless feature can potentially offer high energy efficiency solution by eliminating frequency translation blocks and exploiting heavy duty cycling. It is also promising for mostly digital transceiver architecture.

In addition, the IR UWB narrow pulse in the time domain also offers accurate location and ranging capability. Its ranging resolution is given by

$$R = \frac{c}{2BW},$$
(1.1)

where BW is the bandwidth of the signal and c is the speed of light. If utilizing the 7.5 GHz bandwidth from 3.1 - 10.6 GHz, IR UWB radar resolution can achieve as high as 2 cm.

1.1.2 The Principle and Advantages of UWB Beamforming

The pulse like nature of IR-UWB makes it amenable to CMOS digital technologies. The resulting transceiver could thus benefit from the down-scaling of CMOS devices by tapping on faster digital logic and tremendous digital signal processing power available [5]. The digital nature also provides programmability which is needed for calibration and tuning. On the other hand, transistors suffer from voltage headroom reduction due to down-scaling of CMOS devices. Although the down-scaling improves the transistor speed for RF requirement, it deteriorates the achievable output power due to the voltage headroom reduction and reliability concern.

One way of overcoming output power limitation is through on-chip or off-chip passive power combiners [5]. However, they are generally lossy and incur additional area or cost. Spatial power combination illustrated by narrowband phase array system offers a promising solution in terms of efficiency and cost-effectiveness [6]. Phased arrays have uniformly spaced antennas and produce beamforming in target direction with high gain while rejecting other direction interferers. The object movement could be detected by this beamsteering ability which is desirable for imaging and radar application. The multi-antenna technique is also adopted by Long-Term Evolution (LTE) and Fourth Generation (4G) digital cellular technologies as part of their standard. Therefore, phased array systems are attractive for both radar and communication application.

For narrow band system, the antenna array factor is given by the equation

$$AF(\theta) = \frac{\sin(N(kd\sin\theta - \beta)/2)}{N\sin((kd\sin\theta - \beta)/2)}, \tag{1.2}$$

where θ is the polar co-ordinate, N is the number of antenna elements, d is the spacing between the antenna elements, β is the angle at which the main lobe of the beam is focused and $k=2\pi/\lambda$ is the propagation vector of the transverse electromagnetic wave which is inversely proportional to wavelength (λ).

Due to the impulse like nature, UWB signal has a different array pattern expression [7]

$$AF(\theta) = \frac{erf(\sqrt{\pi}(N-1)d\sin\theta/(2\Delta Tc))}{(\sqrt{\pi}(N-1)d\sin\theta/(2\Delta Tc))}, \tag{1.3}$$

where θ is the polar coordinate, c is the velocity of light, ΔT is the pulse width, N is the number of antenna array elements, and each element is separated by a distance of d.

In narrowband phased arrays, there are typically side lobes and grating lobes in the antenna pattern due to the potential zero in the denominator of Equation (1.1). On the other hand, UWB beamformer does not suffer from such issue.

The 4-channel UWB beamformer is illustrated in Figure 1.2. In order to steer the main beam in the desired direction θ, the relative delay between the signals fed to the adjacent antenna elements is given by

$$\Delta T = \frac{d\sin\theta}{c}.$$ (1.4)

Equation (1.4) indicates that the electromagnetic beam can be scanned electronically by controlling the relative delay between signals (ΔT) and distance between adjacent antennas. By keeping the relative delay between different signal path constant, the signals only add up coherently in the air along a particular direction and lead to beam steering in that direction which enables directional point-to-point communication and minimizes the interference to and from other narrow band systems [8]. For N-path phase array transmitter, the Effective Isotropically Radiated Power (EIRP) is improved by $20\log(N)$ [9]. For N-path phased array receiver, the SNR could be improved by $10\log(N)$ (dB) due to signal coherent addition [10].
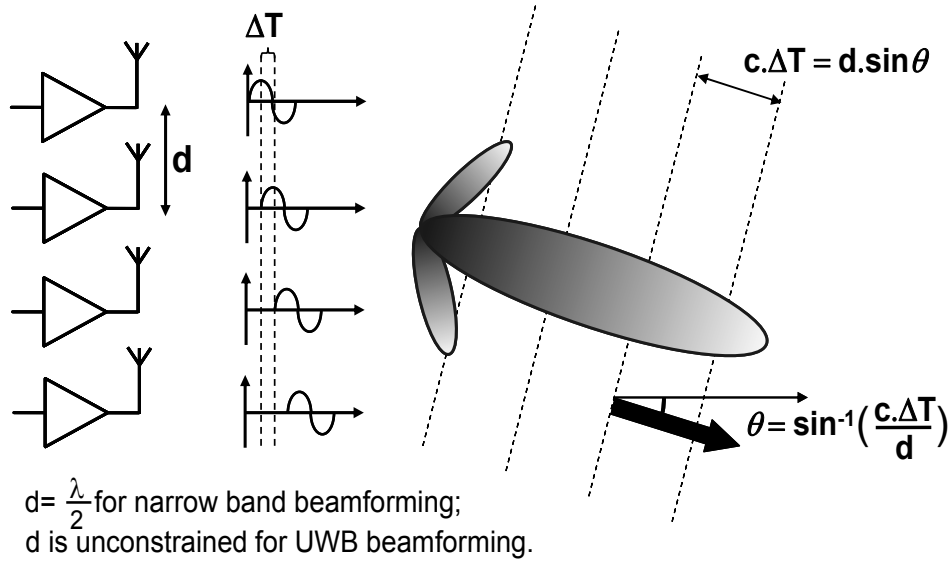
Figure 1.2. UWB beamforming transmitter principle.

Due to the wide band of IR UWB signal, UWB beamforming could also achieve high depth resolution and range resolution at the same time [11]. UWB beamforming can also achieve possible sidelobe pattern shaping through pulse shape tuning [11], and eliminate the antenna spacing dependency on carrier wavelength [7]. Therefore, when compared to narrow band systems, beamforming in UWB also provides an additional degree of freedom in choosing the antenna spacing.

1.2 Motivation

As mentioned earlier, IR UWB transceiver is a promising candidate to enable low power sensor node applications. IR UWB beamformer also has several unique advantages for imaging and radar applications. However, there is still room for improvement for both sub GHz IR UWB transceiver, and IR UWB beamformer, which are summarized as follows:

1. For transceivers, some reported architectures [12], [13], [14] do not fully exploit the digital nature of IR-UWB. Although these analog approaches could achieve high output power, they suffer from poor energy efficiency.

2. For digital intensive architecture, the circuit blocks are not optimized for high speed operation [15], [16], which often results in lower output amplitude and compromising communication range.

3. It is challenging to generate UWB pulse under FCC mask, so filters are generally required which are bulky.

4. For UWB beamformers, there are limited reported works on this aspect. Most of them suffer from architecture limitation and result in poor phase resolution with limited scanning range.

5. Conventional passive L-C based delay element has lossy and bulky problems, resulting in poor energy efficiency as well as large area.

1.3 Research Contributions

Given the research gaps described above, we look into various novel ways of improving the performance of UWB transceiver and beamformer. The contributions of this research are listed below:

1. For sub 1 GHz UWB transmitter, we have proposed an all-digital solution with pulse width and amplitude programmability to achieve center frequency tuning and band shaping. Compared to existing works, we proposed technique and architecture to minimize the impact of parasitic and achieve larger output amplitude.

2. For sub 1 GHz receiver, threshold based detector with auto threshold detection scheme is proposed to improve the energy efficiency. From

measurement, the transceiver achieves 100 pJ/bit and 600 pJ/bit for transmitter and receiver respectively.

3. For UWB beamforming transmitter, we employed vernier delay cell to achieve 10 ps delay resolution, which is 10 times smaller than the currently reported works.

4. ΔΣ DLL is proposed to perform the delay calibration. Through the optimized transmitter architecture as mentioned earlier, we also achieved 10 times power reduction compared to others. The beamfomer achieves 135º phase range with 1º phase resolution, while consuming 9.6 mW @ 80 Mbps. The transmitter achieves energy efficiency of 10 pJ/bit and transmitter efficiency of 7.5%.

5. To adjust the UWB pulse shape for meeting the FCC mask, a power spectral density calibration circuit is proposed.

6. For UWB beamforming receiver, Q compensated method was proposed. The 4-channel beamformer occupies small area of 1.44 mm^2. This is seven times smaller than the other UWB beamformer based on passive delay with similar delay range.

The publications achieved to date are listed below:

[1] Lei Wang, Yong Lian and Chun Huat Heng, "A Sub-GHz Mostly Digital Impulse Radio UWB Transceiver for Wireless Body Sensor Networks," *IEEE VLSI DAT,* 2013.

[2] Lei Wang, Yong Lian and Chun Huat Heng, "3-5 GHz 4-Channel UWB Beamforming Transmitter with 1º Scanning Resolution through Calibrated Vernier Delay Line in 0.13μm CMOS," *IEEE Journal of Solid-State Circuit (JSSC)*, pp. 3145 - 3159, Dec. 2012 (Invited).

[3] Lei Wang, Yong Xin Guo, Yong Lian, and Chun Huat Heng, "3-to-5GHz 4-channel UWB beamforming transmitter with 1° phase resolution through calibrated vernier delay line in 0.13µm CMOS," *IEEE International Solid-State Circuits Conference (ISSCC)*, pp.444-446, Feb. 2012.

[4] Lei Wang, Chandrasekaran Rajasekaran, Yong Lian, "A 3–5 GHz all-digital CMOS UWB pulse generator," *Asia Pacific Conference on Postgraduate Research in Microelectronics and Electronics (PrimeAsia)*, pp.388-391, Sept. 2010.

1.4 Organization of The Thesis

The following thesis is organized as follows. Chapter 2 will give a brief literature review on the architectures of IR UWB beamforming transmitter and receiver. The sub 1 GHz UWB transceivers are discussed in Chapter 3 with detailed design explanation and measurement result. Chapter 4 described the design and measurement of 3-5 GHz UWB beamformer. The UWB beamforming receiver is presented in Chapter 5. Finally, conclusion is given in Chapter 6.

CHAPTER 2 REVIEW OF UWB TRANSCEIVER ARCHITECTURES

2.1 Existing UWB Transmitter Architectures

One of the key challenges of IR UWB transmitter design is to generate UWB pulses that meet the FCC spectral mask as mentioned. Based on the approaches, reported UWB transmitters can be easily classified into analog or digital architecture.

2.1.1 Analog UWB Transmitters

Analog UWB transmitter adopts similar approach as conventional narrow band RF design. In [12], the band shaping is achieved at baseband through DAC. After which, it is up-converted to the desired RF through mixer. Different sub-bands can be combined through RF summer before sending to a broad band amplifier as shown in Figure 2.1. Although accurate band-shaping can be obtained at baseband, it requires many power hungry blocks, such as DAC, LO, mixer and PA. Hence, they generally suffer from poor energy efficiency.
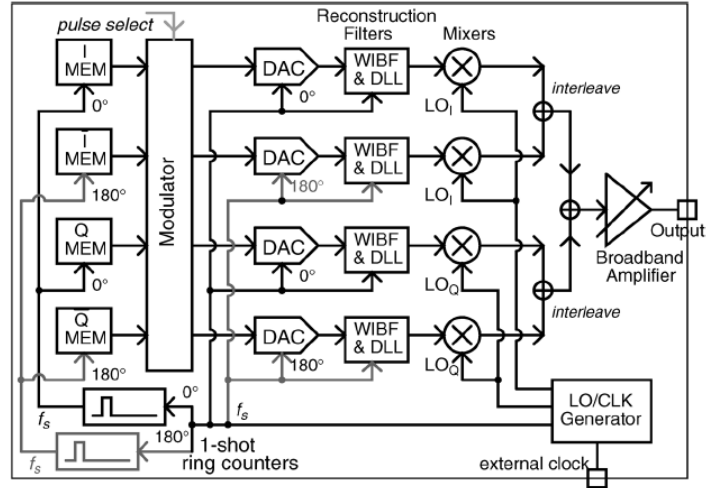
Figure 2.1. Analog UWB transmitter based on traditional analog approach.

Another analog based approach employs on-off modulation of VCO to eliminate the need of LO, mixer and DAC [13], [14], as illustrated in Figure 2.2. This approach allows large output amplitude due to the inductive peaking. However, the short turn-on-time requirement for VCO will impact its energy efficiency. In addition, additional LC filtering is often needed to achieve the desired band-shaping and thus incur area penalty.
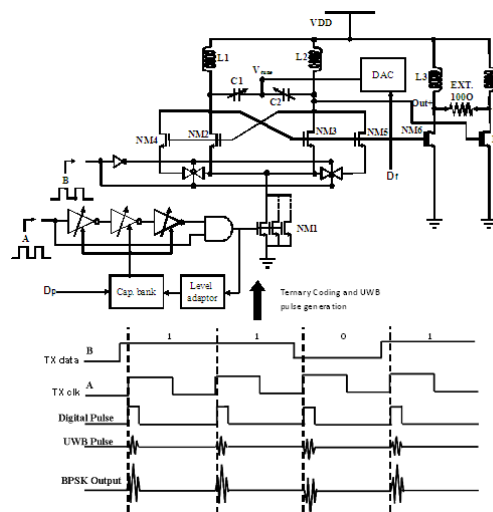
Figure 2.2. Analog UWB transmitter based on VCO.

In general, analog based approach can achieve large output amplitude with accurate band shaping. However, they generally suffer from poor energy efficiency and area penalty.

2.1.2 Digital UWB Transmitters

The pulse-like nature of IR-UWB makes it amenable to digital implementation. In general, the fundamental concept of digital architecture involves generating a string of digital pulses and modulating the amplitude of the digital pulses to achieve the desired band-shaping. Various approaches differ in their way of obtaining digital pulses. In [16] and [15], different delay edges are obtained through digital delay line. The delay edges are then combined through edge combiner to obtain the desired string of short pulses, as shown in Figure 2.3. The pulse width which determines the center frequency are adjustable through tunable delay cell. The number of pulses can be controlled by activating the desired number of edges.
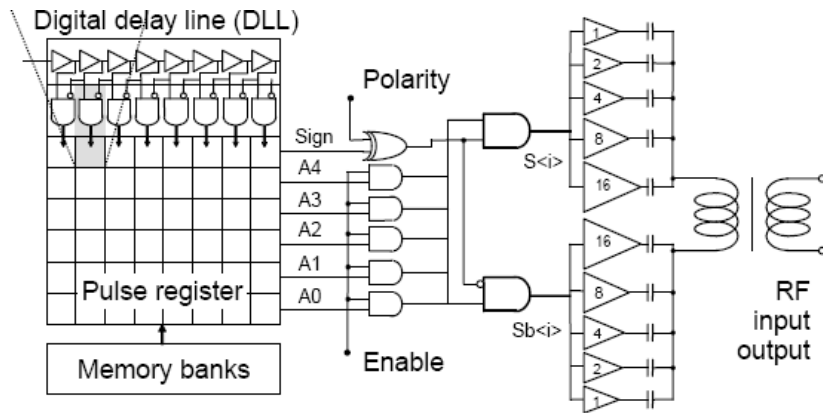
Figure 2.3. Digital UWB transmitter in [16].
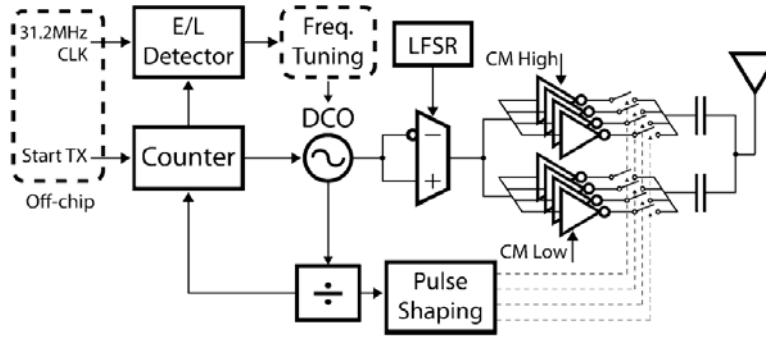
Figure 2.4. Digital UWB transmitter architectures based on DCO.

Table 2.1 The UWB transmitters comparison.

	[12]	[14]	[13]	[16]	[15]	[17]
Tech. (nm)	CMOS 90	CMOS 130	CMOS 180	CMOS 90	CMOS 180	CMOS 90
Supply (V)	1.25	1.35	1.8	1	1.8-2.2	1.2
Energy efficiecy (pJ/pulse)	1250	186	920	22.6	12	17.5
Pulse amplitude (peak-peak)	0.15V@ 4GHz	2.4V@ 7.5 GHz	2.8V@ 4GHz	0.7V (max)	0.06V@ 8GHz	0.71-0.165 V @2.1-5.7 GHz

In [17], digital ring oscillator is employed to create a string of short pulses. The center frequency of ring oscillator is digitally tuned through DAC. Once a string of short pulses have been generated, each pulse amplitude is modulated digitally through buffer amplifier with different sizing depending on the pulse position as shown in Figure 2.4. This will result in a shaped IR-UWB signal and achieve the desired band shaping to meet the spectral mask. It should be pointed out that the need to transmit the resulting short pulses through a buffer

chain could result in excessive buffer size and reduce output amplitude. Hence, in general, digital approach can achieve better energy efficiency with moderate output amplitude. To summarize, various architectures performance are compared in Table 2.1.

The performance comparison of the above mentioned UWB transmitters is listed in Table 2.1. From this comparison table, we could find that analog approach could achieve larger output pulse amplitude, even higher than supply voltage [13, 14]. However their consumed power is relatively large, so the energy efficiency is poor. Better energy efficiency could be obtained by digital approach as in [15-17]. Among these works, the all-digital UWB transmitter in [17] achieves good energy efficiency, relatively high output amplitude, and without any bulky inductors.

2.2 Existing Beamforming Transmitter Architectures

A beamforming transmitter contains an array of transmitters to generate the RF signals with beam steering in particular direction. Phase shifters are essential components for adjusting each channel phase. Depending on the phase shifter location, beamforming transmitter can be classified into following architectures.

2.2.1 IF Phase Shift Beamforming Transmitter

In this architecture, phase shifting is done at baseband before up-converting to RF, as shown in Figure 2.5 [18].
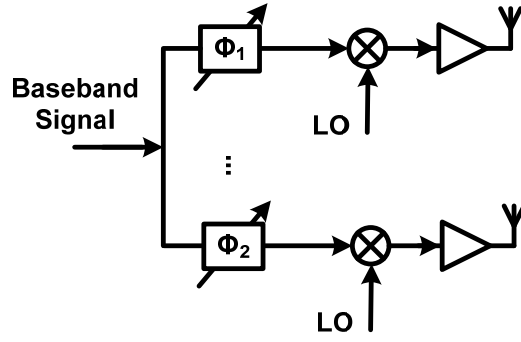
Figure 2.5. Beamforming transmitter with phase shift at IF stage.

Relatively low IF frequency could be chosen to relax the phase shifter design and make it less sensitive to parasitic. In addition, active phase shifters could be adopted instead of bulky and lossy passive ones [19]. However, active phase shifter suffers from linearity issue, especially for transmitter with large amplitude [20]. In addition, the earlier path separation implies duplication of many blocks from baseband up to the PA, which incurs both area and power penalty.

2.2.2 RF Phase Shift Beamforming Transmitter

Phase shifting can also be performed after up-conversion as shown in Figure 2.6. Due to the higher frequency, passive phase shifter is generally adopted in this case.
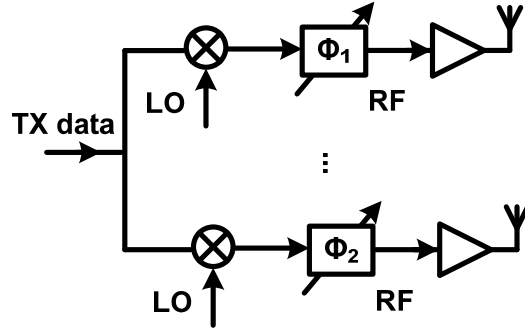
Figure 2.6. Beamforming transmitter with phase shift at RF stage.

Although high frequency blocks, such as LO and mixer can be shared for this architecture, it is generally avoided to improve isolation [21], [14], [11]. Due to the LC phase shifter employed for such high frequency, it could incur significant area penalty and insertion loss due to the on-chip inductor with poorer Q.

2.2.3   LO Phase Shift Beamforming Transmitter

Phase shifting can also be introduced at LO as illustrated in Figure 2.7. It is a popular choice for narrow band system due to its minimal impact on different path gain [22]. However, it can suffer from signal distortion due to dispersion [9]. Unfortunately, it is not suitable for IR-UWB as the phase shift introduced by LO would not result in the desired time delay in IR-UWB signal.
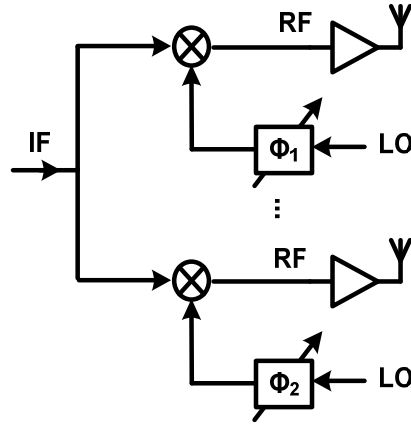
Figure 2.7. Beamforming transmitter with phase shift at LO.

2.2.4 True Time Digital Delay Beamforming Transmitter

Due to the pulse like nature of IR UWB, true time digital delay element has been proposed as phase shifter for UWB beamforming transmitter as shown in Figure 2.8 [23]. The identical delay Td between different paths could be generated when input TX data passes through the buffers. Although digital delay is simple and scalable with technology, its performance is often limited by the achievable absolute delay (T_d) of each delay cell in a given technology. As an example, 10 ps absolute delay is needed to obtain 1° phase resolution with antenna spacing of 18 cm. To achieve such fine absolute delay, it will incur large power consumption even with advanced CMOS technology. The beamforming transmitter in [23] reported phase resolution of only 10° (absolute delay of 100 ps) and its baseband phase shifter alone consumes power as high as 100 mW.
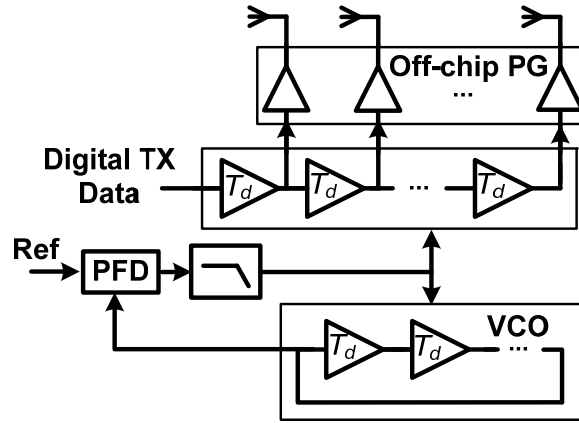
Figure 2.8. True time digital delay beamforming transmitter.

2.3 Existing Beamforming Receiver Architectures

Like beamforming transmitters, a beamforming receiver contains an array of receivers to receive the RF signals with beam steering in particular direction. Phase shifters are still essential components for adjusting each channel phase. Depending on the phase shifter location, beamforming receiver can also be classified into IF, RF and LO phase shift architectures [10], [24]. However, only RF phase shift architecture is suitable for UWB beamforming receiver due to similar reasons as beamforming transmitter. Depending on phase shifter implementation, UWB beamforming receiver could be categorized into passive or active phase shifter based architectures.

2.3.1   Passive Phase Shift Beamforming Receiver

In this architecture, true time delay is performed by passive LC element [7], [11], [25] based on the approximation of transmission line segments. The delay of this structure is approximately

$$T_d = n\sqrt{LC} \qquad\qquad (2.1)$$

where is *n* the number of LC sections as shown in Figure 2.9. To eliminate insertion loss of the passive LC elements, high Q inductors are usually adopted [7], [11], [25], resulting in bulky implementation especially when large delay range is needed.
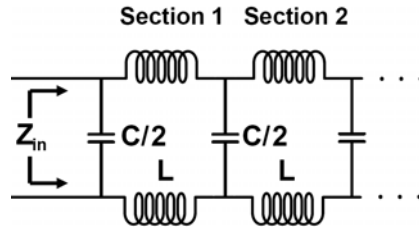
Figure 2.9. Passive phase shifter.

2.3.2   Active Phase Shift Beamforming Receiver
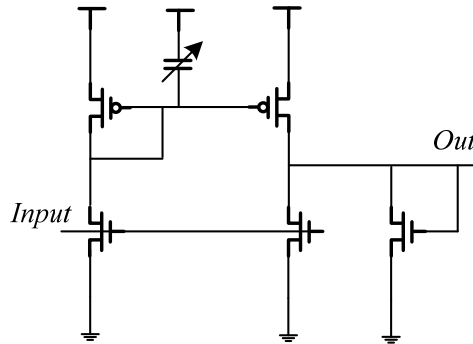
Figure 2.10. Active phase shifter.

UWB signal is phase shifted by active delay element in this architecture [26].

The high Q bulky on-chip inductors are avoided by a g_m-RC or g_m-C all-pass delay circuit as shown in Figure 2.10. However this active inductor based true time delay consumes large power and is difficult to operate for frequency higher than 3 GHz.

2.4 Findings

From the literature review, digital approach for IR-UWB transmitters is generally preferred for good energy efficiency. Besides, it is impractical for multi-channel beamforming transmitter due to excessive area penalty. In addition, reliability is also a concern due to the lower gate oxide breakdown voltage in deep sub-micron technology. Another important factor keep us away from analog UWB transmitter is that we have to adopt a Digital to Analog Convertor (DAC) to convert the beamforming delay edges into analog input to the analog UWB transmitter. References [27] and [28] predict that digital phase shift beamforming transmitter is complex and power hungry due to DACs. They did not recognize the fact that digital phase could be converted to UWB pulse directly with duty-cycled nature and lower power feature. Therefore, we choose all-digital UWB transmitter without DAC.

To achieve short pulse width without incurring significant power or the need of most advanced technology, alternative digital architecture needs to be proposed for all-digital UWB transmitter. Similarly, for beamforming transmitter, true time digital delay offers attractive compact area solution. However, we need to come out with alternative architecture to achieve the desired small phase resolution without excessive power penalty.

As for UWB beamforming receiver, we want to operate up to 10 GHz, so the

active phase shifters could not be adopted. New design approach is needed for passive phase shifter to achieve large delay range with reasonable area consumption. In the following chapters, we will elaborate our proposed design further.

CHAPTER 3   SUB 1 GHZ IR UWB TRANSCEIVER

3.1 System Requirement And Design Consideration

As mentioned earlier, IR-UWB can offer low cost and low power transceiver solution suitable for WBAN targeting for health care application. In this chapter, we will propose a sub 1 GHz IR-UWB transceiver caters for the basic ECG application. For such application, the transceiver needs to achieve 1 Mbps for a short communication range of less than 0.25 m within an office environment. Sub 1 GHz is chosen in this design to enable low power implementation by exploiting larger ratio of f/f_T. In addition, it also offers better penetration.

As analyzed in chapter 2, digital based IR-UWB transmitter offers better energy efficiency with moderate output, and is thus adopted in this design. For the receiver portion, ADC based approach [29], [30] requires high speed GHz ADC and might not be an energy efficient approach. Reference [31] employs mixer down conversion whereas reference [32] employs template correlation that requires accurate synchronization. Both approaches are also not energy efficient due to the architecture complexity.

In this chapter, a digital intensive IR-UWB transceiver with intermittent operation will be covered. Detector based approach with automatic threshold detection is employed to address the power issue and will be discussed in subsequent sections.

3.2 Link Budget

There are many different UWB channel models [33, 34]. As indicated in [33] and [35], a simple and effective model is an ideal free space path in which there is no ground reflection and multi-path. It has a path loss that is proportional to the square ($\alpha=2$) of the separation d, and inversely proportional to the wavelength (λ):

$$PL_{dB}(d) = \alpha \cdot 10 \log_{10}\left(\frac{4\pi d}{\lambda}\right) = \alpha \cdot 10 \log_{10}(d) + c \qquad (3.1)$$

where c is a power scaling constant included in calibration.

Friis formula suggests that a 1 m path loss equals 35.5 dB for a signal operating at 1 GHz. The antennas are designed by others, and we do not have the antenna gain information, so combined antenna gain of -3 dBi is assumed for the transmitter and receiver together. Therefore, from Equation (3.1), a 25 cm distance exhibits a path loss of 23.5 dB. This is a conservative estimation, because the sub-1 GHz UWB signal has lower frequency. Besides the path loss, there are other losses incurred, such as cable loss, PCB, connector and etc. In our implementation, we conservatively assume 6 dB for such combined implementation losses (*IL*).

By approximating the transmitted UWB pulse with triangular pulse shape and peak-to-peak amplitude of 2 V, we could estimate the pulse energy as follows:

$$P_{TX} = \frac{(V_{pp}/4)^2}{50} \cdot 1ns \cdot DR \qquad (3.2)$$

where DR is the data rate of 1 Mbps, and pulse duration is assumed to be 1 ns. This results in P_{TX} of -23 dBm.

Hence the transmitted power available at the receiver input is

$$P_{TXA} = P_{TX} - PL - IL \qquad (3.3)$$

where *PL* is the estimated 23.5 dB path loss, *IL* is the estimated 6 dB combined implementation losses. This results in *P$_{TXA}$* of -52.5 dBm.

The channel noise is

$$N_{channel} = -174 \frac{dBm}{Hz} + 10 \log_{10}(B) \qquad (3.4)$$

which gives rise to -84 dBm noise power under 1 GHz channel bandwidth.

The minimum detectable power at the receiver front end is

$$P_d = SNR + N_{channel} + NF \qquad (3.5)$$

where *NF* is noise figure, and *SNR* is the required signal to noise ratio. Our system *NF* is estimated to be 17 dB. To obtain reasonable BER using our proposed threshold detector, 6 dB *SNR* is required from our system studies, so *P$_d$* is estimated to be -61 dBm.

Therefore, the estimated link margin is about 8.5 dB.

3.3 A Sub 1 GHz OOK IR UWB Transceiver

3.3.1   The Proposed Architecture

The proposed IR UWB transceiver architecture is shown in Figure 3.1. To increase communication reliability, 11-bit Barker Code is incorporated as coding scheme. At the transmitter side, TX data is first encoded in the digital

back-end using Barker Code Encoder. OOK modulation is adopted here. Finally, it generates the UWB pulse by the all-digital UWB pulse generator.

The receiver incorporates low noise amplifier (LNA) to strengthen the input signal. The amplified signal is compared with a threshold voltage using a threshold detector. It is not convenient to set the threshold value manually. When there is process, voltage and temperature (PVT) changes, the preset threshold value has to be readjusted. Therefore, auto-threshold detection is adopted for this OOK IR UWB receiver. The threshold voltage is provided by a calibration circuit. Clock re-timing and data recovery is performed using a low voltage low power SAR DLL. Finally, the digital backend decodes the received signal using Barker Code decoder.
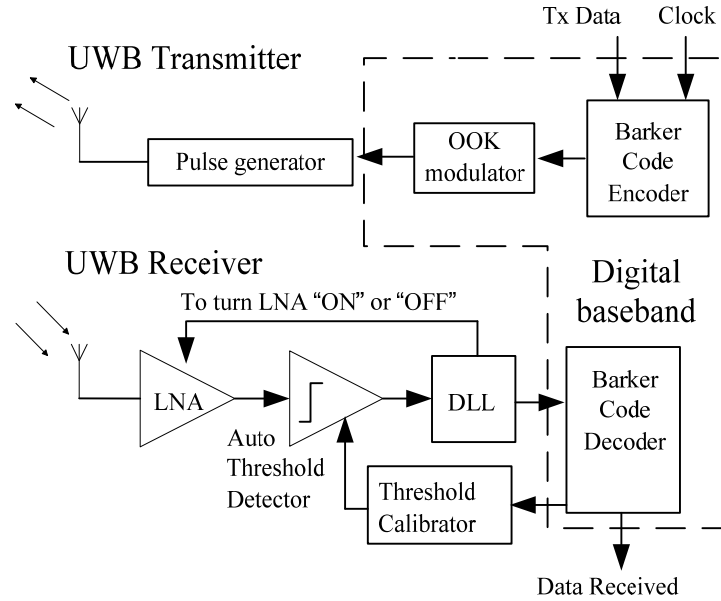
Figure 3.1. The proposed IR UWB transceiver architecture.

3.3.2 All-Digital OOK UWB Transmitter
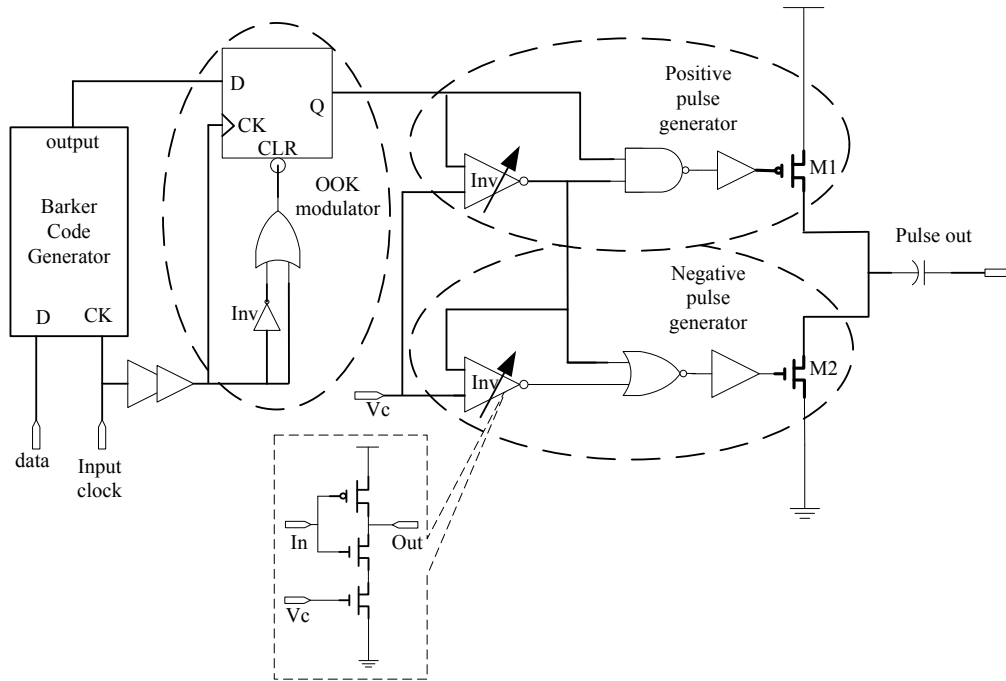
Figure 3.2. UWB transmitter structure.

The proposed OOK UWB transmitter is shown in Figure 3.2. As mentioned in Chapter 2, UWB transmitter architecture has the trade-off between energy efficiency and output power. This transmitter adopts digital architecture with improved output power. The modulated input data and its delayed version go through a NAND gate or a NOR gate to generate a narrow positive or negative pulse. The output of NAND or NOR gate turns on the PMOS or NMOS transistor respectively, which are sized to shape each pulse to the required amplitude. The buffers after NAND and NOR gates are used to drive the PMOS and NMOS. Larger pulse width and amplitude will be generated through a smaller external voltage, Vc. To generate peak to peak output amplitude of 2.5 V, the output current should be at least 50 mA. To get this large current, the sizing of output transistors is critical. The sizing of transistor M1 is determined by

$$\left(\frac{W}{L}\right)_{M1} = \frac{2I_{M1}}{K_p \cdot V_{gt}^2}$$ (3.6)

where *Kp* is a technological parameter, and *Vgt* is *(Vgs-Vt)*, the over-drive voltage. 0.35 μm technology is used here, so *Kp* is about 40 μA/V^2. Assuming the over-drive voltage to be 2 V here, we could get that the width of M1 is about 220 μm. Considering layout parasitic, bonding wire, package, PCB connection, and other losses, a larger width of 300 μm is adopted for M1. In a similar way, 150 μm is chosen as the width for transistor M2.

3.3.3   The Proposed OOK UWB Receiver
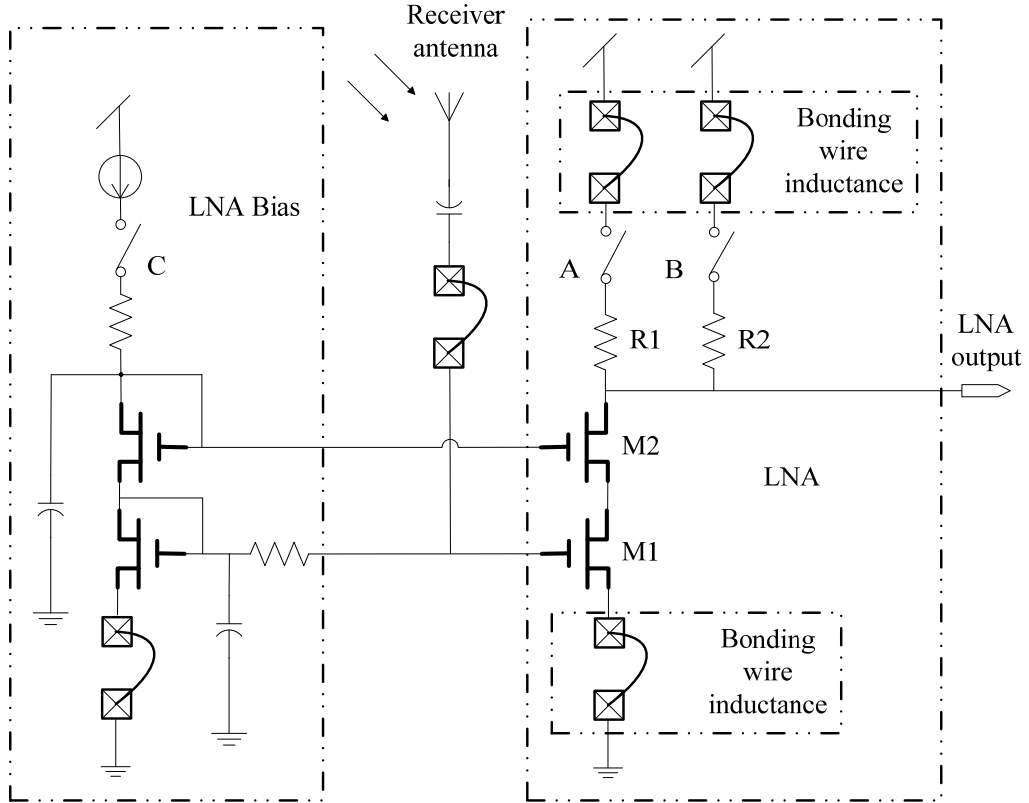
Figure 3.3. The LNA circuit.

Receiver front end has to incorporate gain stage to increase communication range. However, gain stage like LNA is typically power consuming. Therefore, the receiver front end has a trade-off between communication range and power consumption. Since the target application does not require long distance data transmission, a single stage LNA with variable gain is adopted. Reference [36] demonstrates that voltage matching generates larger signal amplitude than power matching for a sub 1 GHz LNA. Therefore, this LNA adopts voltage matching for threshold detection. It adopts cascode structure to increase its gain and bandwidth, as shown in Figure 3.3. The gain is tunable by changing the output resistance through switches A and B. Large current of 10 mA is assigned for this LNA. Actually its power consumption could be lowered by intermittent operation as shown later. According to [37], the optimum width of M1 is determined by

$$W_{opt} = \frac{1}{3\omega L C_{ox} R_s} \tag{3.7}$$

where ω (rad) is the operation frequency of 1 GHz, L is 0.35 μm, C_{ox} is 5 mF/m^2, and R_s is 50 source resistance. Therefore, 600 μm is chosen for the width of M1. Transistor M2 is cascoded to reduce the interaction of output node with input node by reducing the miler effect of M1's gate to drain capacitance. A relatively smaller size of 100 μm is chosen here. The transistor sizing in the bias circuit is about five times smaller to reduce the power consumption.

Considering voltage headroom at the output, R2 and R1 are designed to 200 Ω and 100 Ω, respectively. The post layout simulation result shows its gain could be varied from 3 dB to 12 dB, as shown in Figure 3.4. Its bandwidth covers from 100 MHz to 1 GHz. The antenna and bypassing capacitor form the high-pass filter while the low-pass filtering is achieved by the LNA output resistance and parasitic capacitance.
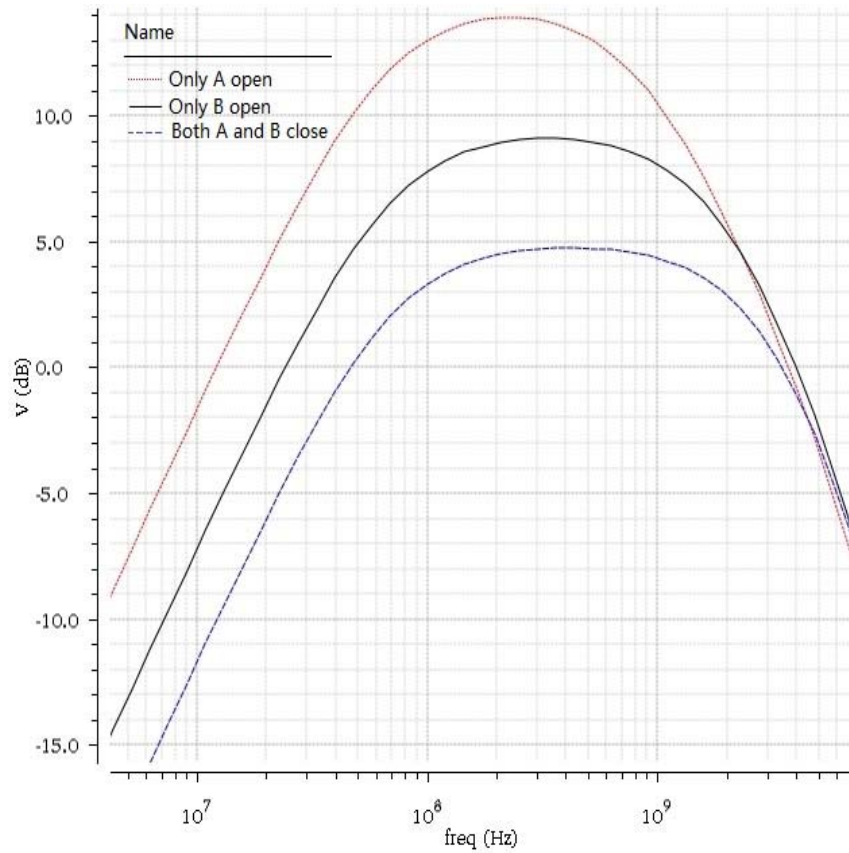
Figure 3.4. The LNA variable gain simulation results.

High Q inductor not only takes too much area, but also causes stability problem and ringing effect for the UWB pulses. The ringing effect may deteriorate the waveform and result in wrong decision for the threshold detection. Therefore, this LNA does not incorporate inductor. The receiver *NF* is dominated by the LNA which is the only RF block. The LNA's *NF* worst case simulation result is shown in Figure 3.5. Although the 1/f noise is much larger than the white noise below its corner frequency, the estimation of 17 dB *NF* is quite conservative when calculating the transceiver link budget.
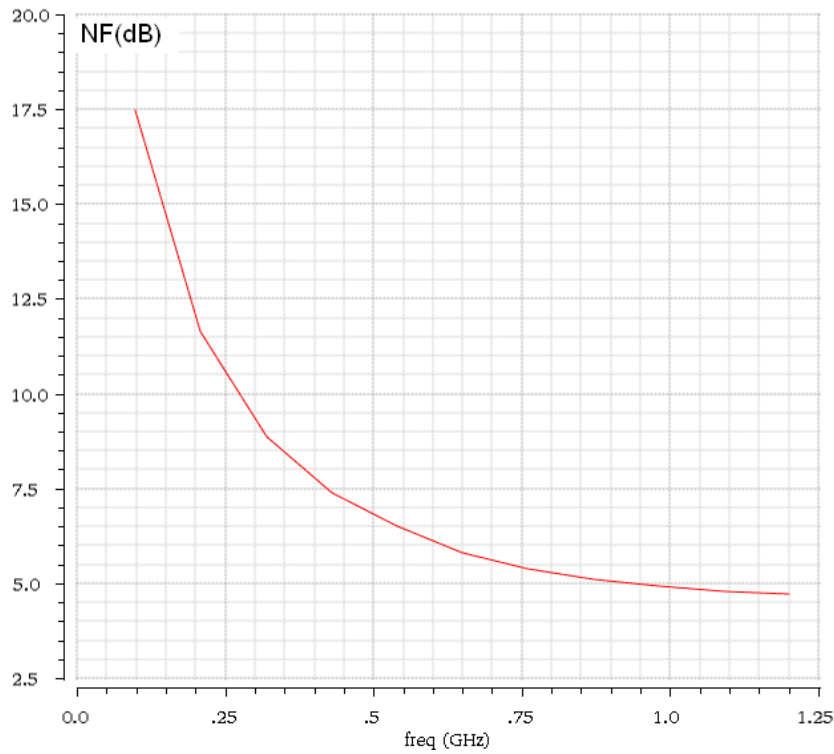
Figure 3.5. The simulated *NF* of LNA.

Due to the inherent nonlinearity of CMOS devices, unwanted beat products could be generated from third-order inter-modulation (IM3). Receiver third-order nonlinearity is commonly characterized by a third-order intercept point (IP3). IM3 may have a detrimental effect in narrow band RF communication system, because out of band signals may generate unwanted beat appearing within signal band. On the other hand, gain compression problem may arise when there is a large in band signal or an out of band blocker. The LNA IP3 performance and 1-dB compression point (P1dB) simulation result under different gain setting are shown in Figure 3.6 and Figure 3.7 respectively. The horizontal axis of Figure 3.6 represents the input power. Its vertical axis is the output power of the fundamental component and IM3. When large signal is present, the gain should be set smaller to prevent LNA saturation. Therefore, with variable gain setting, the compression problem is much relaxed.
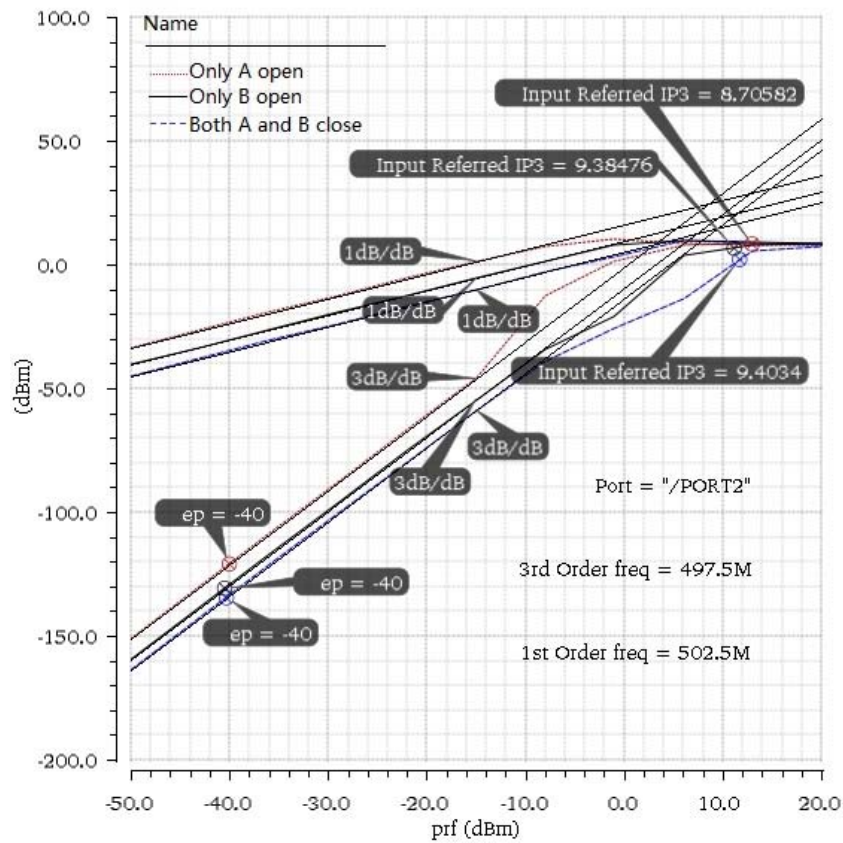
Figure 3.6. The simulated *IP3* of LNA.
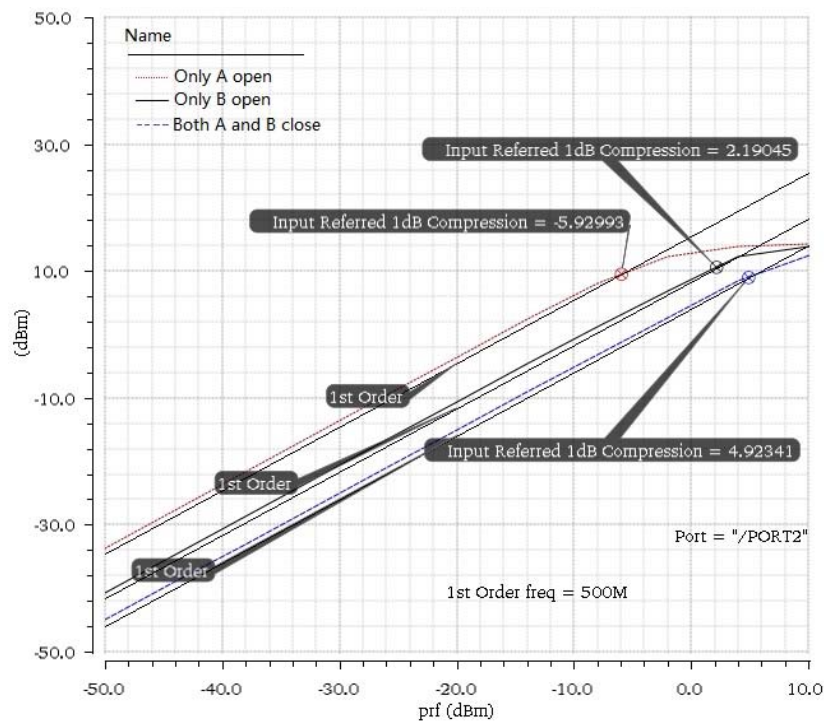
Figure 3.7. The simulated *P1dB* of LNA.

39

The receiver front end is power hungry due to LNA, so the LNA operates intermittently to reduce power consumption. It only operates during data arrival window of about 15 ns and is powered-down during other time. The data window is provided by DLL based clock retiming circuit. LNA power-down is achieved by turning off LNA operation stage and biasing through opening switches A, B and C, as shown in Figure 3.3.
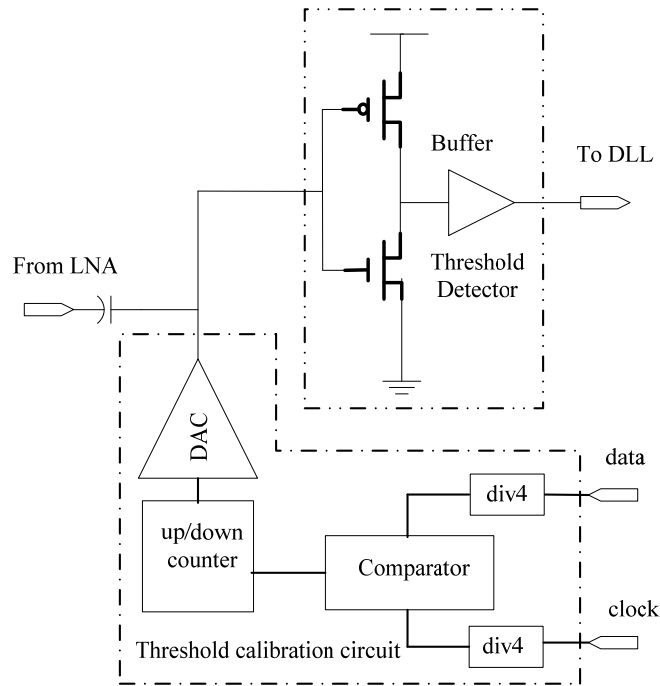
Figure 3.8. Schematic of UWB receiver frontend.

The LNA is followed by an inverter-based threshold detector which is biased with high gain, as shown in Figure 3.8. The threshold value is provided by a threshold calibration circuit through a DAC. In 11-bit Barker Code, there are no more than four consecutive logical '0's or '1's (data '0' is encoded as "11100010010" and data '1' is "00011101101"). The calibration circuit takes

advantages of this characteristic to provide the threshold level. Suppose the default threshold value is preset relatively high. During calibration, it will be decreased if more than four consecutive logical '0's are received. On the other hand, the threshold level will be increased if more than four consecutive logical '1's are received. The calibration continues until the threshold level converges to the desired level.

3.3.4 DLL Based Clock Retiming Circuit

The uncertainty of block delay makes it difficult to predict the data arrival window for proper LNA operation. Both PLL and DLL could align the received data phase to clock by VCO or delay line. DLL is chosen in this work to obtain better jitter performance.
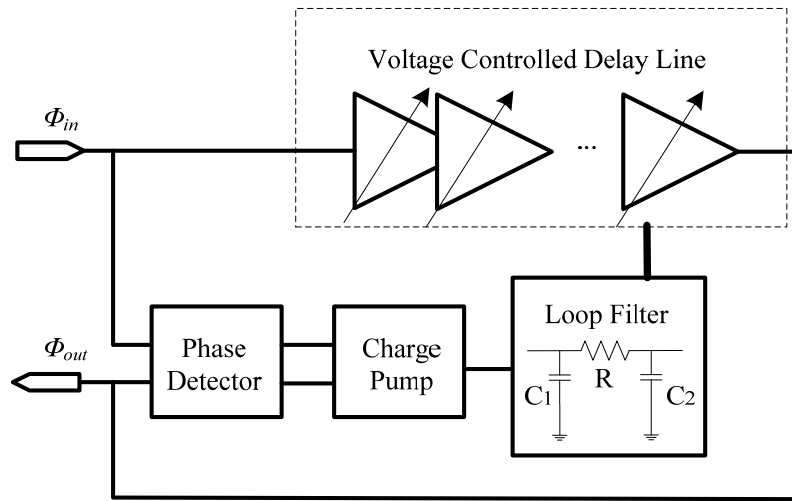
Figure 3.9. Analog DLL architecture.

Based on the delay line and control circuits, DLL architectures could be categorized into analog DLL, digital DLL, or semi-digital DLL. The analog DLL structure is shown in Figure 3.9. It matches the input and output phases

through voltage controlled delay line. The controlling voltage comes from a charge pump and loop filer. This voltage is proportional to the input and output phase difference.

Analog DLL could achieve good jitter performance due to the feedback loop with continuous delay but suffers from limited phase range [38]. Therefore, this architecture is not suitable for clock retiming circuit, because the received data phase could vary from 0 to 2π. The area of analog DLL is also typically large due to bulky passive components used in low pass filter.
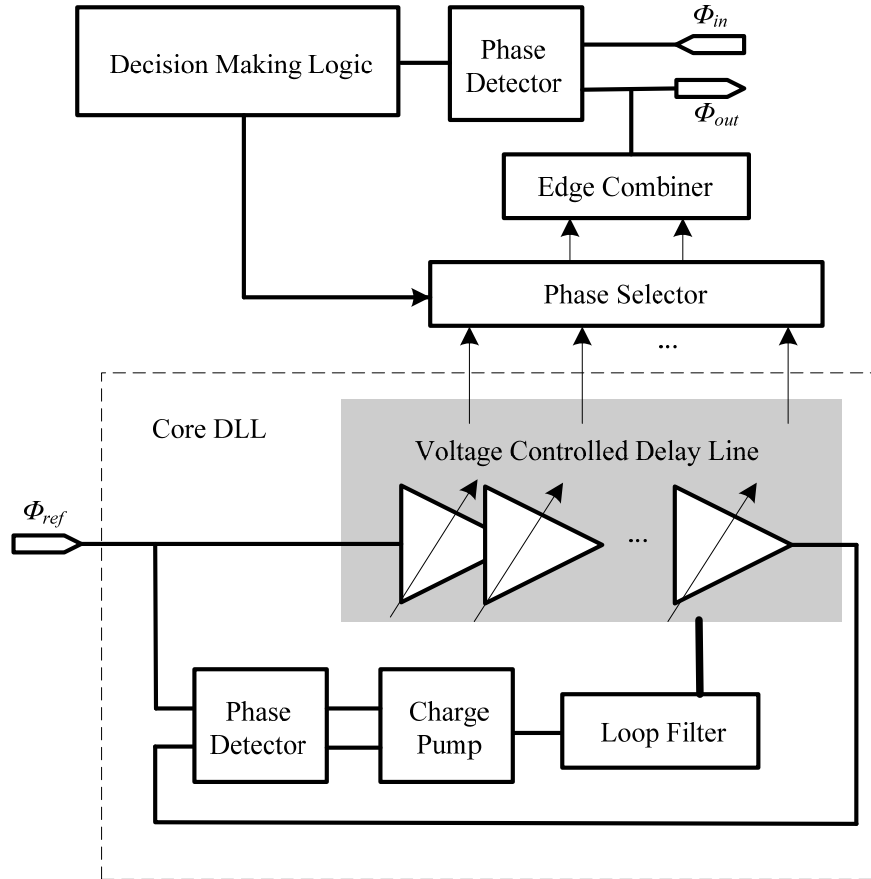
Figure 3.10. Semi-digital DLL architecture.

To widen the phase range of traditional analog DLL, semi-digital DLL has

been reported [39]. Its architecture is shown in Figure 3.10. It incorporates an analog DLL as a core DLL to generate multiple clock phases. Additional phase selector and interpolator are adopted to generate a coarse output phase. This output phase could be fine-tuned to match input phase through phase detector and decision making logic. Compared to analog DLL, its jitter performance is poorer due to the phase selector and interpolator, but its phase range is extended to 0 - 2π. Thus, semi-digital DLL could be used for receiver clock retiming circuit. However, its dual loop architecture is too complex for our application.
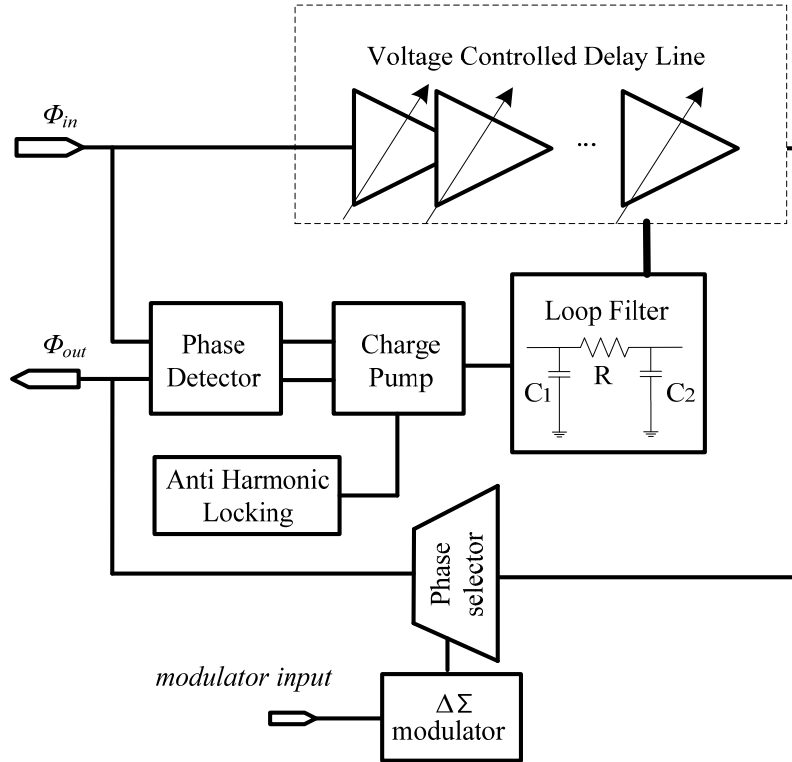
Figure 3.11. $\Delta\Sigma$ DLL architecture [40].

The emerging $\Delta\Sigma$ DLL [40] is an improved architecture of semi-digital DLL, as shown in Figure 3.11. It also generates multiple clock phases to widen the phase range of traditional analog DLL. However unlike semi-digital DLL, it

reuses the phase detector and analog decision making circuit composed of charge pump and loop filter. Therefore, it has much simplified architecture than traditional semi-digital DLL. To lower the jitter due to phase selecting process, it incorporates a $\Delta\Sigma$ modulator. Thus, it becomes a strong candidate which can achieve both fine delay resolution in the pico-second range and good jitter performance.

$\Delta\Sigma$ DLL could be adopted as receiver clock retiming circuit. However, this DLL has to be always on to provide time window, so large power will be consumed due to analog blocks.
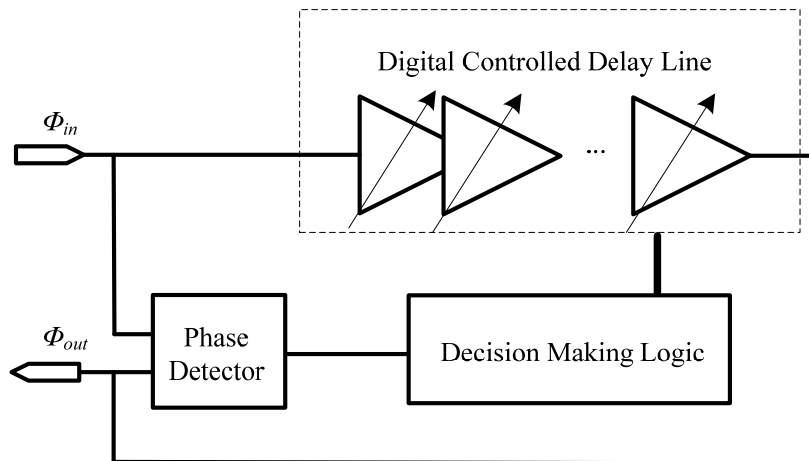
Figure 3.12. Digital DLL architecture.

Digital DLL architecture is shown in Figure 3.12. It adopts digital controlled delay line. Its control words are generated from digital logic, so this architecture is much simpler and less power consuming compared to above mentioned DLLs. Its phase shift could easily cover from 0 to 2π due to fully digital control. It is also amenable to digital CMOS. Its delay resolution usually depends on absolute delay, so it is not very good and determined by

technology [41]. Actually, for our receiver clock retiming circuit, the delay resolution and jitter performance is not critical, because the time window provided by DLL only need to be large enough to cover the LNA set-up, amplification, and settling down. The timing resolution is not too much a concern for our intended application. Hence, digital DLL is adopted in this work.

The digital decision making logic could be implemented by shift registers, up/down counters, or successive approximation register (SAR) [42]. The DLL in this thesis adopts SAR controlled all-digital structure to achieve the short locking time. It adopts binary search scheme. The locking-in procedure of the SAR DLL is shown in Figure 3.13. The delay generated approaches the desired value in a binary way. For N-bit SAR DLL, it only takes N-step to lock in. Therefore, it has very short locking time. With shorter locking time, the LNA could be more quickly duty cycled to save power.
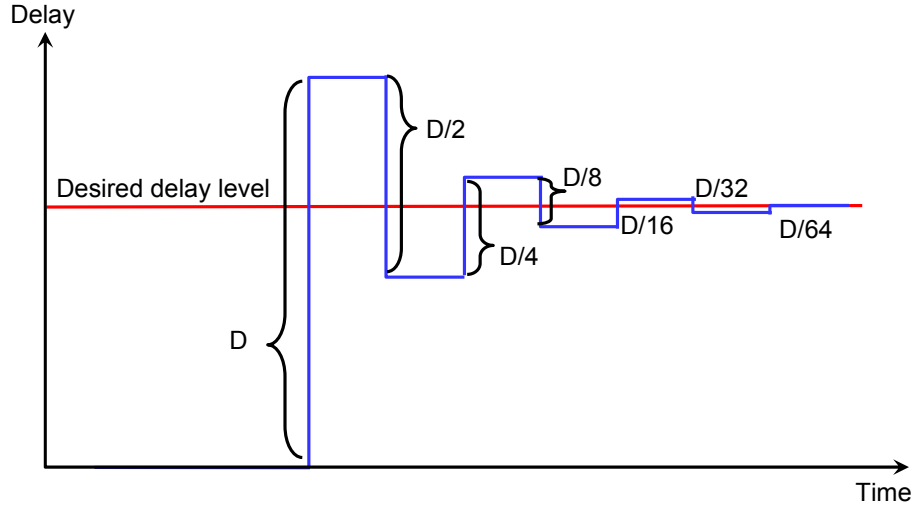
Figure 3.13. The locking in procedure of the SAR DLL.

The SAR DLL based clock retiming circuit is shown in Figure 3.14. It has a 1

MHz clock as input. Another input is the threshold detected data. This circuit is able to align the "*input clock*" with the received "*data*" by delaying the input clock properly. The "*in-phase clock output*" signal is delayed version of the input clock after it passes through the digital controlled delay line. A phase detector compares the phases between "*data*" and "*in-phase clock output*". Based on this phase information, the SAR controller will decide whether to increase or decrease the delay.
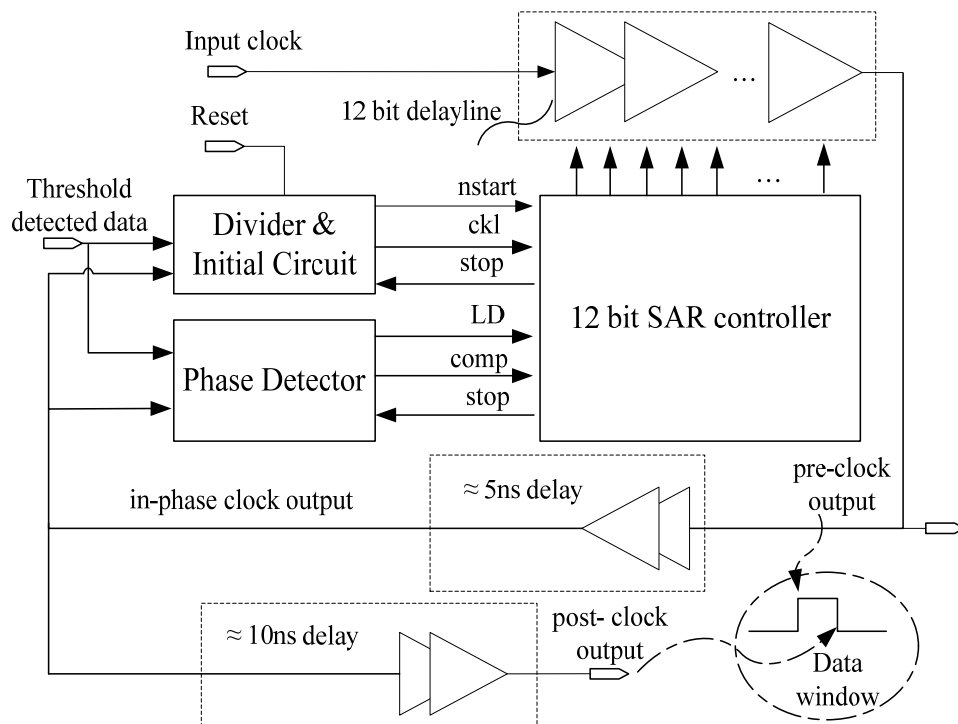
Figure 3.14. The architecture of DLL-based clock re-timing circuit.
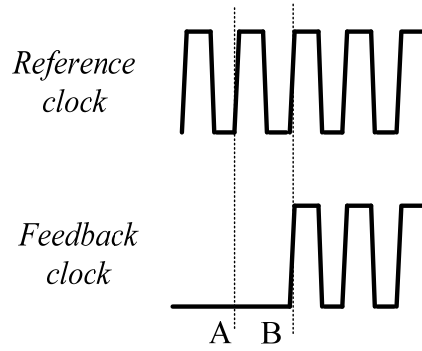
Figure 3.15. Harmonic locking problem in DLL.

Harmonic locking is a common problem in traditional DLL [40]. As shown in Figure 3.15, there is potential that the feedback clock can be delayed by more than one reference clock and result in harmonic locking. Anti-harmonic locking detection circuit could be adopted to avoid this problem [40], but it will incur additional complexity in control. This problem is circumvented in this work by using divided "*threshold detected data*" as clock signal for decision making logic. The simple circuit is shown in Figure 3.16. No decision is made when there is no threshold detected data initially. In this way, the harmonic locking problem is eliminated during circuit start-up. It could also make sure SAR decision making logic has a 4 times slower clock than the other circuit. This is crucial for DLL, because every decision should be made based on circuit fully responded state.
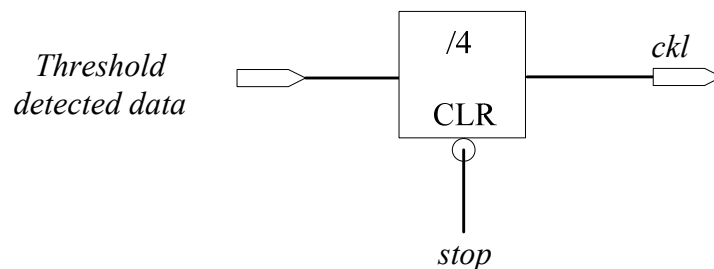
Figure 3.16. Clock signal generation for SAR decision making logic.

The DLL delay resolution is about 0.2 ns. After this DLL is locked, the signal "*pre-clock output*" comes about 5 ns earlier than "*data*", "*post-clock output*" arriving about 10 ns later than "*data*". These two signals could generate a time window with an edge combiner to enable LNA to operate intermittently. If this window is too short, the BER will be affected. If this window is too long, the power consumption will too large. Therefore, this 15 ns time window is based on the trade-off between BER performance and power consumption. To make the DLL itself low power, low supply voltage is adopted. By reducing the supply voltage from 3 V to 1 V, only one ninth of dynamic power is needed to operate this DLL. Smaller supply voltage also reduces the charging current. This indicates the value of capacitors could be decreased to generate the same delay, so area could also be smaller.

3.3.5 Synchronization Scheme
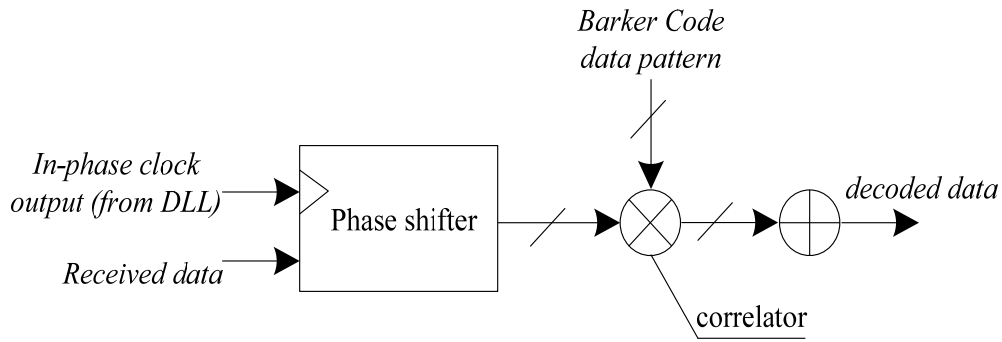
Figure 3.17. The implementation of digital back-end.

As mentioned, Barker Code is adopted in this system. A data '0' is encoded as "11100010010", while a data '1' is encoded as "00011101101". The use of

Barker Code enhances the communication reliability because the bitwise shifted version of the Barker Code has poor auto-correlation sum compared to its original version. The rising edge of the encoded data triggers the UWB pulses.

Decoding is performed in the receiver digital back-end, as shown in Figure 3.17. It incorporates a digital correlator. The received data is decoded by being correlated with Barker Code data pattern. The system declares synchronization only after three consecutive data '1's are detected with bit error rate of 2^{-33} (every data '1' is encoded as 11-bit Barker Code).

3.3.6   Measurement Results

The OOK IR UWB transceiver circuit was implemented using a standard 0.35 μm CMOS technology. Its floor plan on the die photo is shown in Figure 3.18. With all-digital structure, the transmitter area is very small. It occupies an area of 0.09 mm². The only passive component in the transmitter is the bypass capacitors. The receiver, including LNA, threshold detector, threshold calibration circuit and DLL, occupies an area of 1.2 mm². The prototype is packaged using CQFP 80 package.
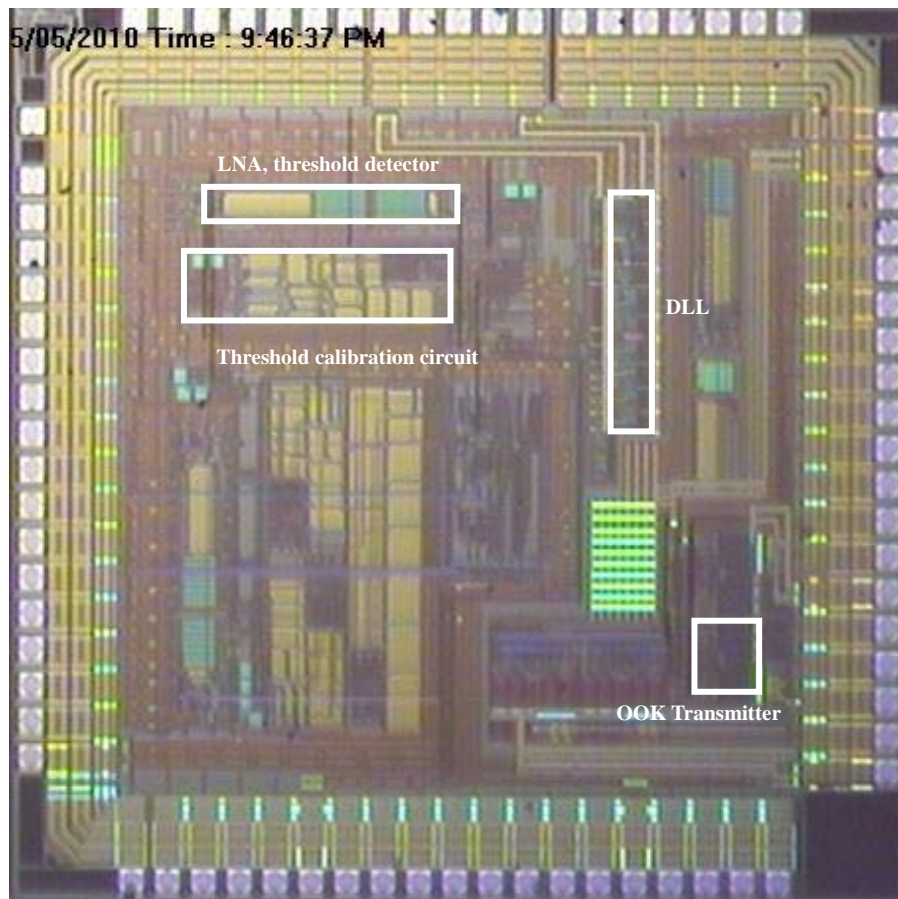
Figure 3.18. Die photo of the IR UWB transceiver.
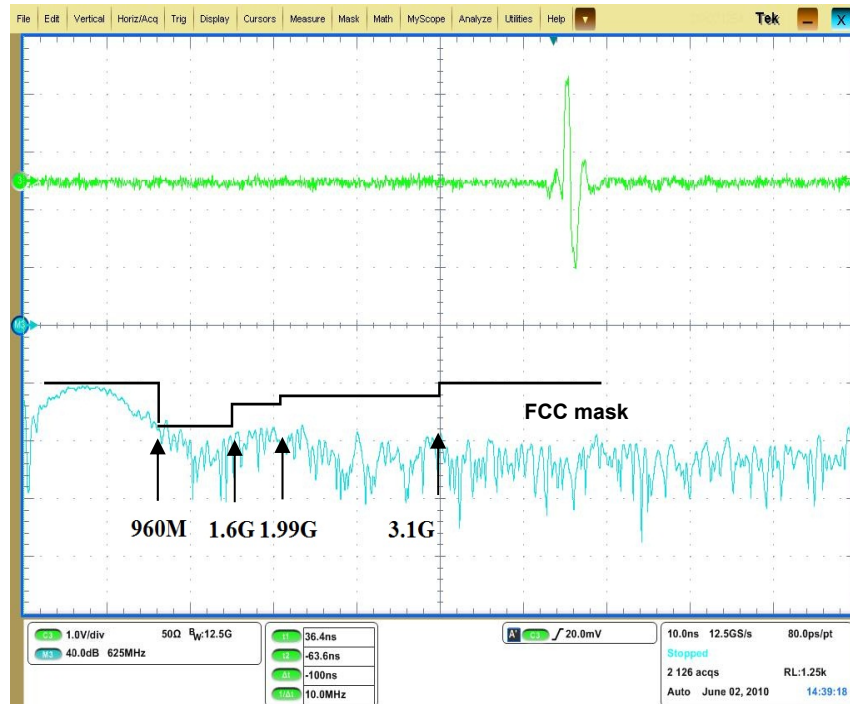
Figure 3.19. Measured transmitter output with spectrum.

The UWB transmitter is tested with Tektronix DPO71254 Digital Oscilloscope. The transmitted UWB pulse and its spectrum are shown in Figure 3.19. The FCC spectrum mask is satisfied with tunable UWB pulse width and amplitude. Its center frequency is around 500 MHz. Under a 3.3 V supply, 2.9 V_{PP} output amplitude could be obtained as shown. It consumes about 30 μA under 3.3 V supply at 1 MHz data rate. Therefore, the transmitter achieves an energy efficiency of 100 pJ/pulse.

The test set up for the whole transceiver with ECG recording interface is shown in Figure 3.20. An ECG signal generator sends the cardiac waveforms to ECG recording circuit. After amplifying, digitizing and processing these signals, the ECG recording circuit generates digital TX input data for UWB transmitter.
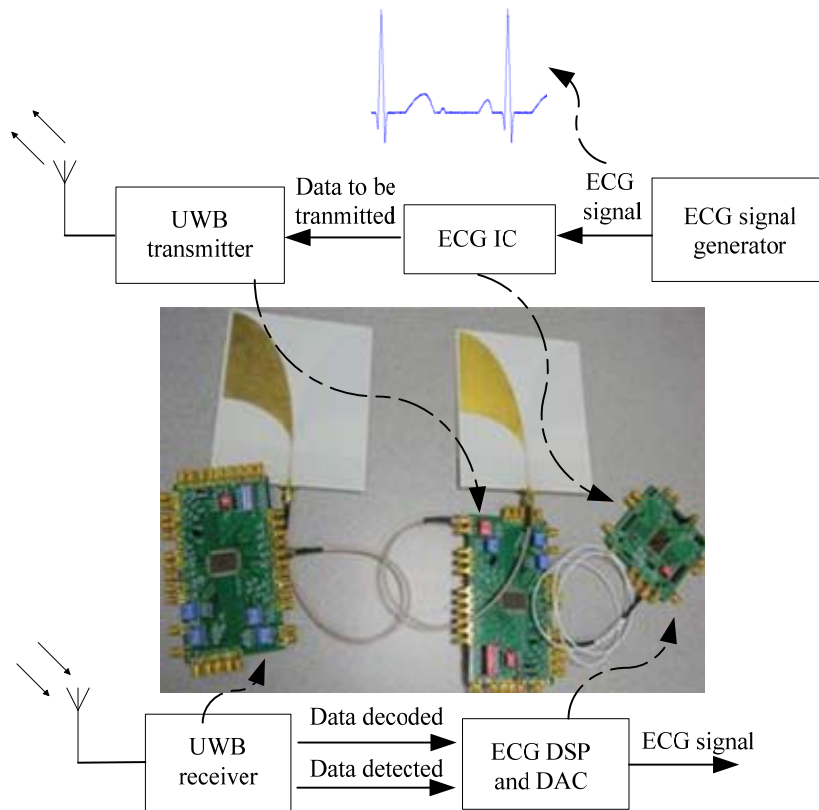
Figure 3.20. UWB transceiver testing.

The transceiver system is tested wirelessly in office environment. The receiver main points testing results are shown in Figure 3.21. The data from ECG output is first encoded with Barker Code in the pulse generator. After receiver antenna and LNA, the threshold detected signals are shown as narrow pulses. Due to the limited IO pin number, the LNA is not tested separately. We could see the modulated data pattern in the threshold detector output (w/o decoding), i.e., data '0' being encoded as "11100010010" and data '1' being encoded as "00011101101".
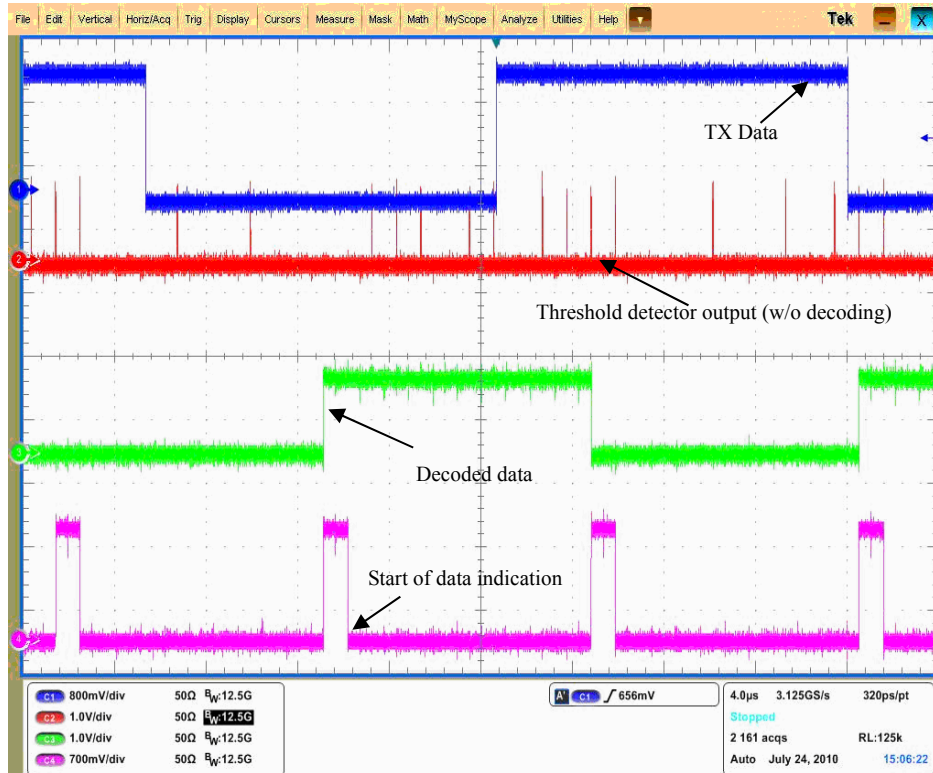
Figure 3.21. Receiver testing results.

After the receiver digital back-end decoding, the transmitted data is recovered. The start of data indication is used for communication interface with the following ECG chip which could processes the RX data. Figure 3.22 shows the Matlab reconstructed ECG waveform from collected RX data of 25 cm wireless reception. By comparing the decoded RX data with TX data, BER could be calculated.

The measured BER performance is shown in Figure 3.23. Within 25 cm antenna distance in office environment, there is no error bit. Smaller than 10^{-3} BER could be achieved if the communication distance increases to 27 cm. If longer distance is required for communication, more amplification stages should be designed to compensate the path loss. The receiver consumes 0.6

mW under intermittent operation at 1 Mbps. The measured receiver sensitivity is -53 dBm when the BER is below 10^{-3} at 1 MHz data rate and communication distance of 25 cm.
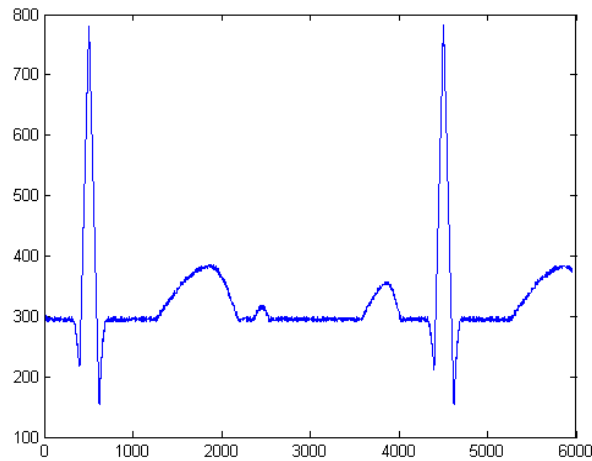
Figure 3.22. Reconstructed ECG waveform from RX data.
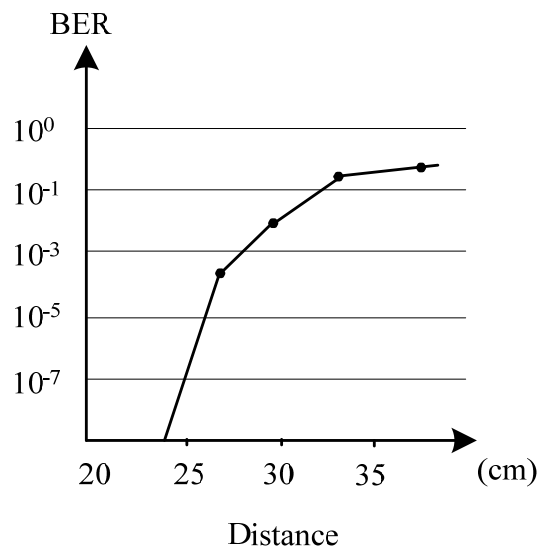
Figure 3.23. The measured BER performance.

3.3.7 Comparison with other recent works

Table 3.1 Comparison with other recent transmitter works

Transmitter	[43]	[44]	[45]	This work
Tech. (μm)	CMOS 0.15	CMOS 0.18	CMOS 0.18	CMOS 0.35
Supply (V)	1	1.8	1.8	3.3
Power (mW)	<0.001@ 25kbps	0.3@ 1Mbps	--	0.1@1Mbps
Energy efficiency (pJ/pulse)	<40	300	27	100
Output amplitude (V_{PP})	0.7	1.6	0.6	2.9
Peak-peak output voltage/ Energy efficiency (V/pJ)	>1.75%	0.53%	2.22%	2.9%
Modulation	BPSK	OOK	DPSK	OOK

Table 3.1 shows the performance summary of proposed UWB transmitter and its comparison with other recently published CMOS UWB transmitters operating in 0-960 MHz. All these transmitters adopt digital structure. Work [44] consumes the highest power of 0.3 mW at 1 Mbps data rate, because its pulse width is as wide as 2 ns and it transmits differential signal to antenna. Work [43] consumes less power due to smaller amplitude of about 0.7 V_{PP}. Work [45] gets output amplitude of 0.13 to 0.6 V_{PP} with 23 μW to 74 μW power consumption. Higher peak to peak output voltage is desirable because it indicates higher output power and longer communication range. Therefore, to make a fair comparison, both energy efficiency and output voltage should be considered. Our work achieves the best results, when the peak to peak output voltage over energy efficiency is compared. Among these designs, this work is the simplest in structure and achieves the highest output pulse amplitude with medium power consumption.

The down-scaling improves the transistor speed for RF requirement. The advanced technology provides higher f_T and smaller parasitic for the transistors, so good energy efficiency could typically be achieved. On the other hand, it deteriorates the achievable output power due to the voltage headroom reduction and reliability concern.

The receiver performance summary and comparison with other recent sub 1 GHz receivers are shown in Table 3.2. Both work [44] and this work intermittently operate LNA, thus consuming much lower power than work [43]. The static power is as large as 1.7 mW in [43], so we can expect a lot of power reduction by intermittent operation. This comparison shows that UWB transceiver could be duty cycled and a lot of power could be saved in this way. It is its architectural advantage. Work [44] consumes low power of 0.3 mW at 1 Mbps data rate, as half small as power consumption in this work, due to the use of more advanced technology and smaller time window for intermittent operation.

Table 3.2 Comparison with other recent receiver works

Receiver	[43]	[44]	This work
Tech. (μm)	CMOS 0.15	CMOS 0.18	CMOS 0.35
Supply (V)	1	1.8	3.5
Power (mW)	1.9@25kb/s	0.3@1Mb/s	0.6@1Mb/s
Energy efficiency (pJ/pulse)	1900	300	600

CHAPTER 4   3-5 GHz UWB BEAMFORMING TRANSMITTER

Based on the literature review on various beamforming architectures discussed in Chapter 2, beamforming transmitter with baseband digital true time delay element is adopted here for its small area and potential high energy efficiency. To overcome the delay resolution and power trade-off, we have proposed the use of Vernier delay line to achieve relative delay rather than absolute delay. This eliminates the trade-off involving delay resolution and power. We also proposed the use of $\Delta\Sigma$ DLL and SAR DLL to achieve the desired frequency and delay calibration. The details of the proposed 4-channel 3-5 GHz UWB beamformer will be discussed next.

4.1.   The Proposed UWB Beamforming Transmitter System

As shown in Figure 4.1, the proposed system consists of beamforming delay chain, four identical all-digital UWB transmitters, delay calibration circuit, and Power Spectral Density Calibration (PSDC) circuit. The baseband TX data is first delayed by the beamforming delay chain to generate equal path delay difference between adjacent channels. The delayed input edges in each path will then trigger the UWB transmitter to generate UWB pulses. There is also a digitally controlled inverter based delay line determining the UWB pulse center frequency. Local edge combining method is proposed to lower the power consumption. To minimize the static power consumption and increase the transmitter energy efficiency, fully digital delay cells are employed in this work. In order to obtain accurate path delay and UWB pulse center frequency,

these digital delay cells are calibrated by ΔΣ DLL together with SAR DLL. Pulse shaping is also provided through eight levels amplitude tuning to achieve the desired UWB spectrum. A PSDC is also incorporated to provide automatic spectrum tuning to meet the desired UWB spectrum mask.
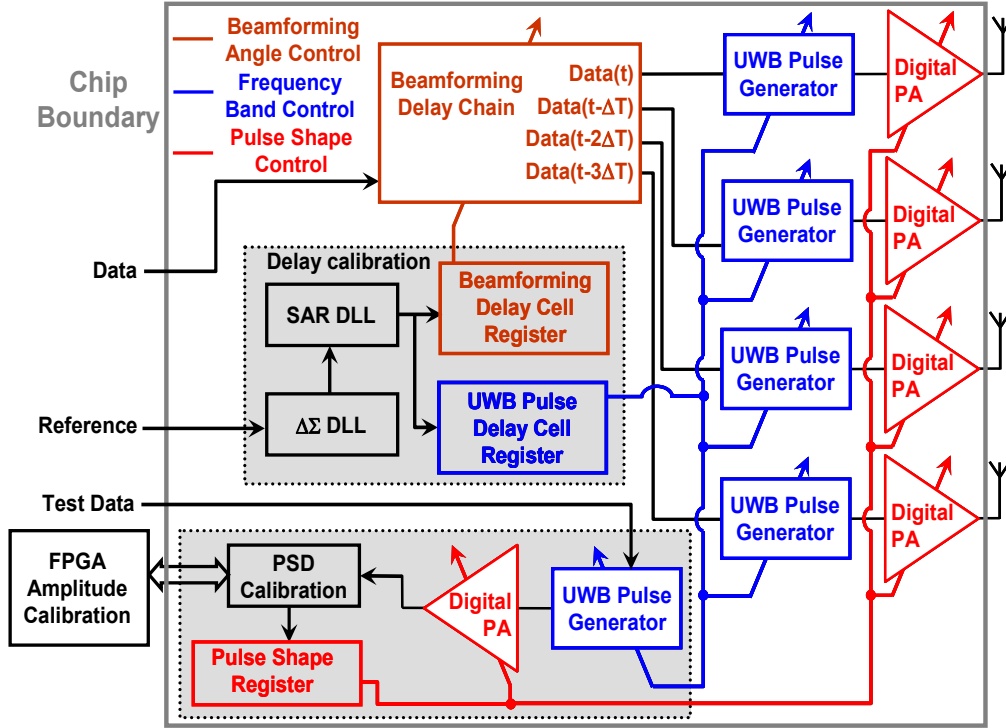
Figure 4.1. The proposed system architecture.

Based on the UWB beamforming analysis in Chapter 1, to achieve a fine scanning resolution, a small delay step is needed. To have a wide scanning range, a large delay range is required for certain antenna space. Our system chose 18 cm antenna space for testing. This antenna spacing is selected to make a fair comparison with other works. Fine delay resolution is desirable on two aspects. Firstly, it gives rise to small scanning resolution which is important for localization. Given a transmission radius of 2 m, 1° scanning resolution will correspond to 3.5 cm scanning range. If 10° scanning resolution is used, the scanning range degrades to about 35 cm. Secondly, the

small delay resolution can be traded off with smaller antenna spacing to achieve a given scanning resolution. For example, if the scanning resolution of 3° can be used, a 10 ps delay resolution will only require antenna spacing of 6 cm, which results in more compact UWB beamforming system. In the following subsection, we will discuss our proposed solution to achieve such a challenging specification.

4.1.1.   Delay Generation

Of the whole system structure, beamforming delay chain is the most crucial part. To generate 1° phase resolution at 18 cm antenna space, the delay step should be as small as 10 ps. To increase the scanning angle as large as 90°, the delay range should be as large as 600 ps.
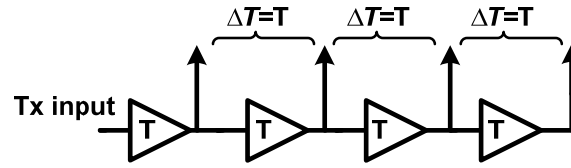
(a)
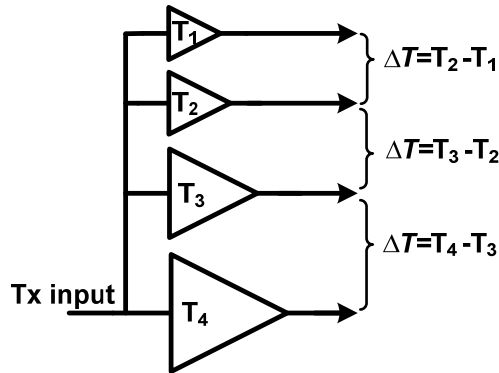
(b)

Figure 4.2. (a) Absolute delay generation. (b) Relative delay generation.

There are various ways of creating identical delay difference between each path. In references [11], [23] and [46], the delay difference is generated through cascading the delay cells in series like Fig. 4.2 (a). Simple delay matching and calibration will be achieved, because there is only one kind of delay cell. However, it is difficult to have one delay cell covering delay range from 0 to 600 ps with 10 ps delay step. In addition, to achieve the small delay region, excessive power would be required which will reduce the transmitter energy efficiency. An alternative approach is to connect the delay cell with different sizing in parallel as shown in Figure 4.2 (b). As the path delay is generated by relative delay difference, i.e. $\Delta T=T_2-T_1=T_3-T_2=T_4-T_3$, the delay cell design can be much relaxed with smaller power consumption. However, adopting four different delay cells in the design will complicate the path matching and calibration. Therefore, there is a trade-off between delay resolution and path matching for these delay architectures.

(a)

(b)
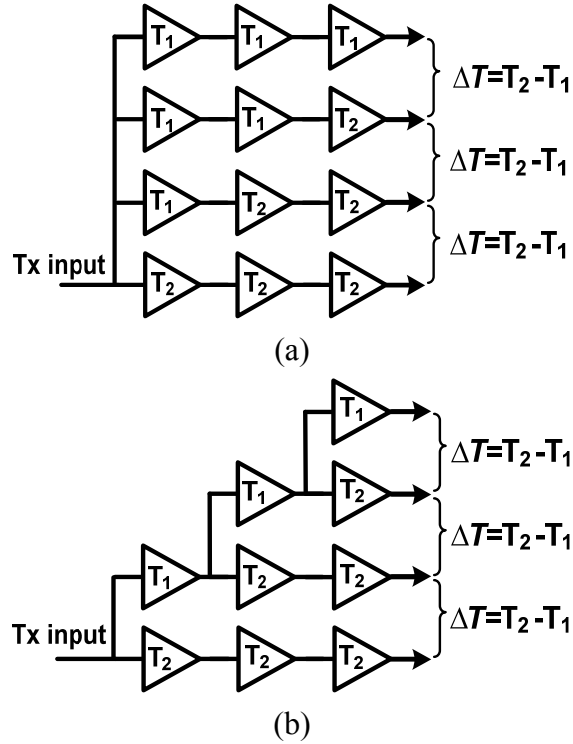
Figure 4.3. (a) The principle of vernier delay line. (b) Delay cells sharing.

To achieve fine delay resolution, easy path matching and easy delay calibration at the same time, we propose the use of vernier delay line. The concept is shown in Figure 4.3 (a). Compared to Figure 4.2 (b), only half number of delay cells is needed for calibration and it is easier to control the delay. To avoid path mismatch in Figure 4.3 (a) (T_1 and T_2 see different loading depending on their position), delay cells sharing scheme shown in Figure 4.4 (b) is adopted and good path matching is achieved with additional dummy delay cells as discussed later. This approach also reduces the number of delay cells needed. We also achieve fine delay resolution, easier calibration and easier path matching. Unlike the true time delay element architecture employed in [23], our approach relies on relative delay concept which eliminate the trade-off between delay resolution and power.

The final beamforming delay chain subsystem is shown in Figure 4.4. To extend the delay range, multiplexer is employed to include more delay elements. When input A of the multiplexer is chosen, the generated relative path delay of T_1-T_2 can vary from -420 ps to 420 ps. This will cover the fine scan range from -45° to 45° at 18 cm antenna space. If input B of the multiplexer is selected, the resulting absolute path delay of T_2 can further extend the delay range to 420 ps - 600 ps. This will cover the course scanning range 45° to 90° at 18 cm antenna space. It should be pointed out that each digitally controlled delay cell (T_1 or T_2) are designed to vary from 300 ps to 720 ps in step of 10 ps to cover phase range from -45° to 90° in step of 1° with antenna spacing of 18 cm. This delay range not only covers the relative delay of -420 ps to 420 ps, but also covers the absolute delay of 600 ps. As the smallest achievable path delay no longer depends on the absolute delay, significant power saving can be achieved.
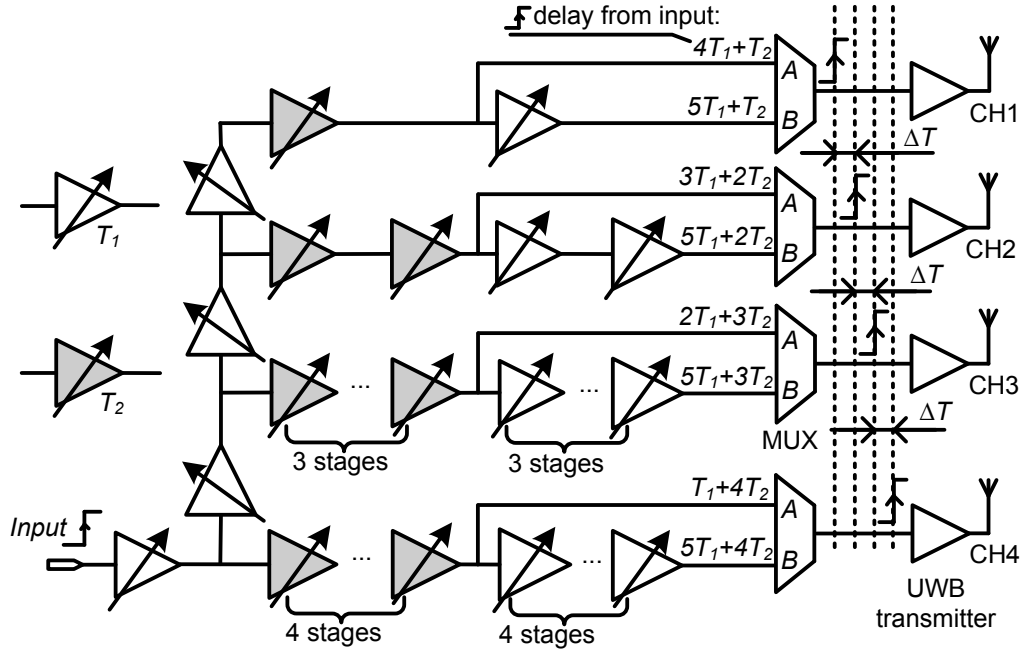
Figure 4.4. Beamforming delay chain subsystem.

4.1.2. Delay Calibration

The proposed relative delay concept enables energy efficient implementation without the need of very fast delay cell which is power hungry. However, in order to achieve accurate phase control, accurate delay needs to be defined. Conventionally, a fixed external reference with counter based approach is commonly employed to provide the required calibration. This often poses a trade-off between calibration accuracy and calibration time. In our proposed architecture, we employed a novel $\Delta\Sigma$ DLL to provide an accurate timing reference. Together with SAR DLL, our proposed approach would eliminate the trade-off between calibration accuracy and time. During normal operation, the $\Delta\Sigma$ DLL could be powered off to achieve greater power saving.

4.1.3. Spectrum Calibration

Most digital based IR-UWB transmitter provide spectrum shaping by tuning the amplitude of the transmitted pulse as described in Chapter 2. This is often done manually by tuning the amplitude based on the observation of the measured spectrum. Our proposed architecture incorporates PSDC to provide ways of achieving auto spectrum calibration. From our observation, we noticed that a conforming UWB spectrum exhibit certain amplitude ratio for component at transmitting frequency and component at low frequency range. By measuring such amplitude ratio, we can then fine tune the desired pulse shape amplitude accordingly.

4.2. The Circuit Implementation

4.2.1. UWB Beamforming Delay Cell

A. Linear Delay Generation

As mentioned earlier, digitally controlled delay cells are needed to cover from 300 ps to 720 ps in steps of 10 ps or smaller. This is achieved through the proposed linear delay generation circuit shown in Figure 4.5. Also shown is the individual beamforming delay cell T_1 and T_2. They have the same schematic and layout (as shown later in Figure 4.6), but the two biases are different. Two separate Digital Controlled Current Sources (DCCS) are used to generate the two biases for the two different delays. These two DCCS are robust in terms of the temperature and process variations and the delay of the circuit could change monotonically with digital input vector [47].
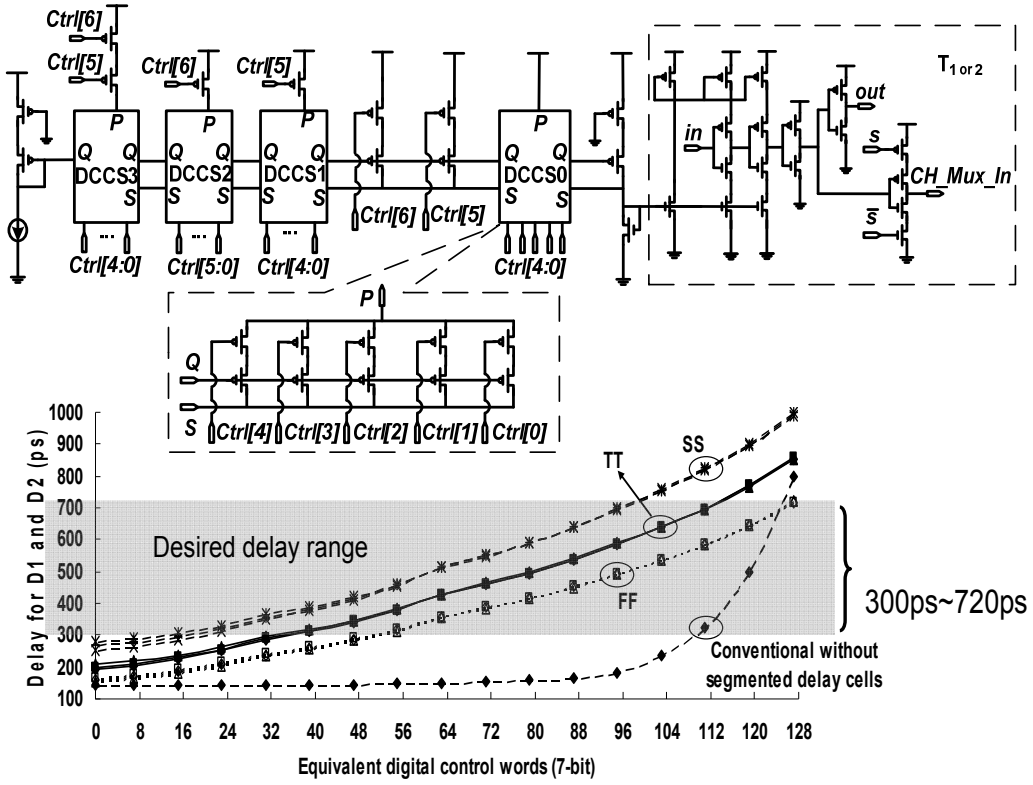
Figure 4.5. The proposed linear delay generation and simulation results in different corner and temperatures.

When both the delay elements have the same input code word, a relative delay of 0 ps can be obtained in the design. Hence, the delay resolution depends on the minimum delay difference between the two delay elements. The relative delay of 10 ps between each path will be generated when the delays of the two delay cells differ by 10 ps. Conventional DCCS with binary transistor sizing will result in linear current variation but non-linear delay time due to the inverse square root dependency between delay and current, as illustrated in the conventional delay cell without segmentation as shown in Figure 4.5. This is undesirable as the large delay variations occur over a relatively narrow control word range and results in poorer delay resolution.

In order to linearize and spread the whole delay range more evenly across the

control word range, we divide the desired delay range into four smaller segments, separately controlled by four different DCCS. Non-binary transistors sizing within each DCCS blocks are employed to linearize the delay characteristic. Monotonicity is still ensured as the increasing control word will result in increasing current mirrored from combined DCCS blocks. As the sizing is critical, post layout simulations with various process corners and temperatures are carried out extensively to ensure the delay cell covers the desired delay range from 300 ps to 720 ps with delay resolution of about 5 ps throughout all process corners. It is also noted from Figure 4.5 that the delay characteristics are sensitive to process variation but less sensitive to temperature variation.
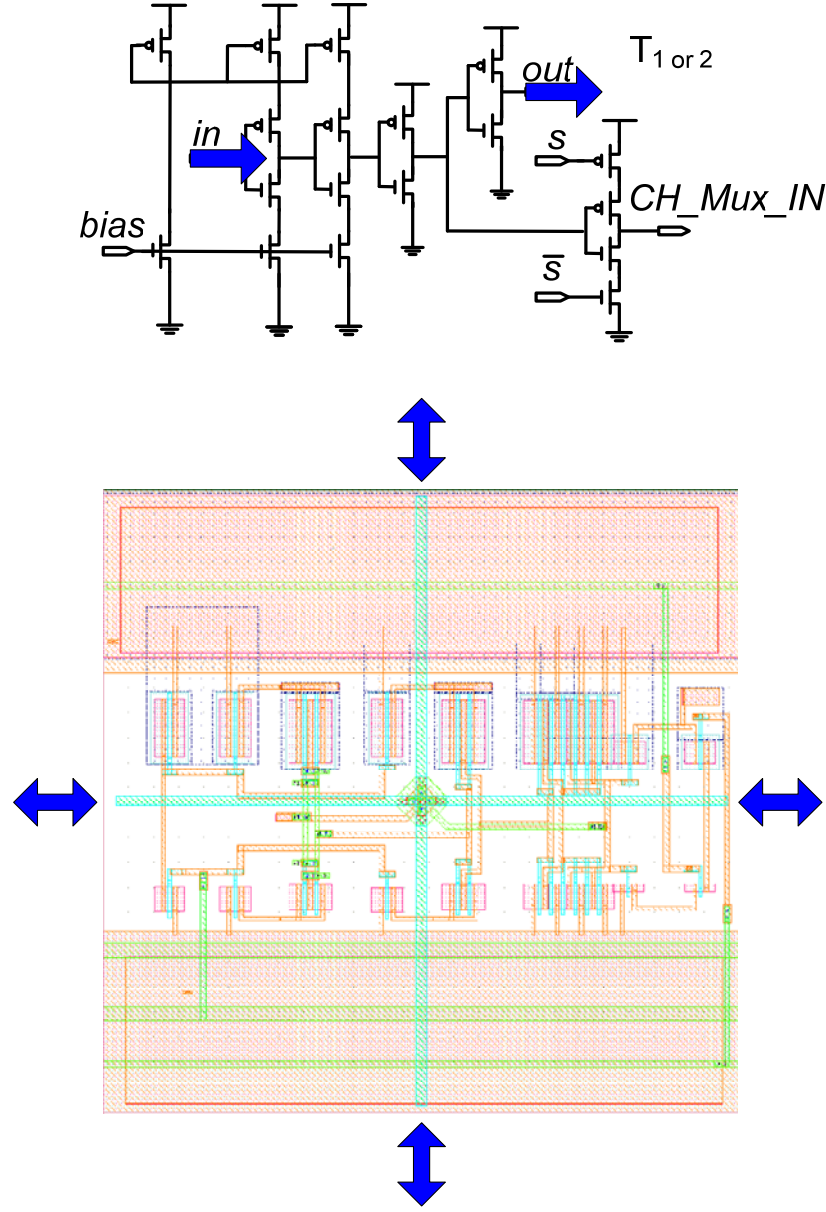
Figure 4.6. The schematic and layout of beamforming delay cell.

Both individual delay cell layout and floor planning have been considered carefully to minimize the path mismatch within the beamforming delay chain. For individual delay cell, both the input (metal 2) and output (metal 4) paths cut through the center of the cell like a cross to facilitate easy interface with neighboring cells along four directions as shown in Figure 4.6.
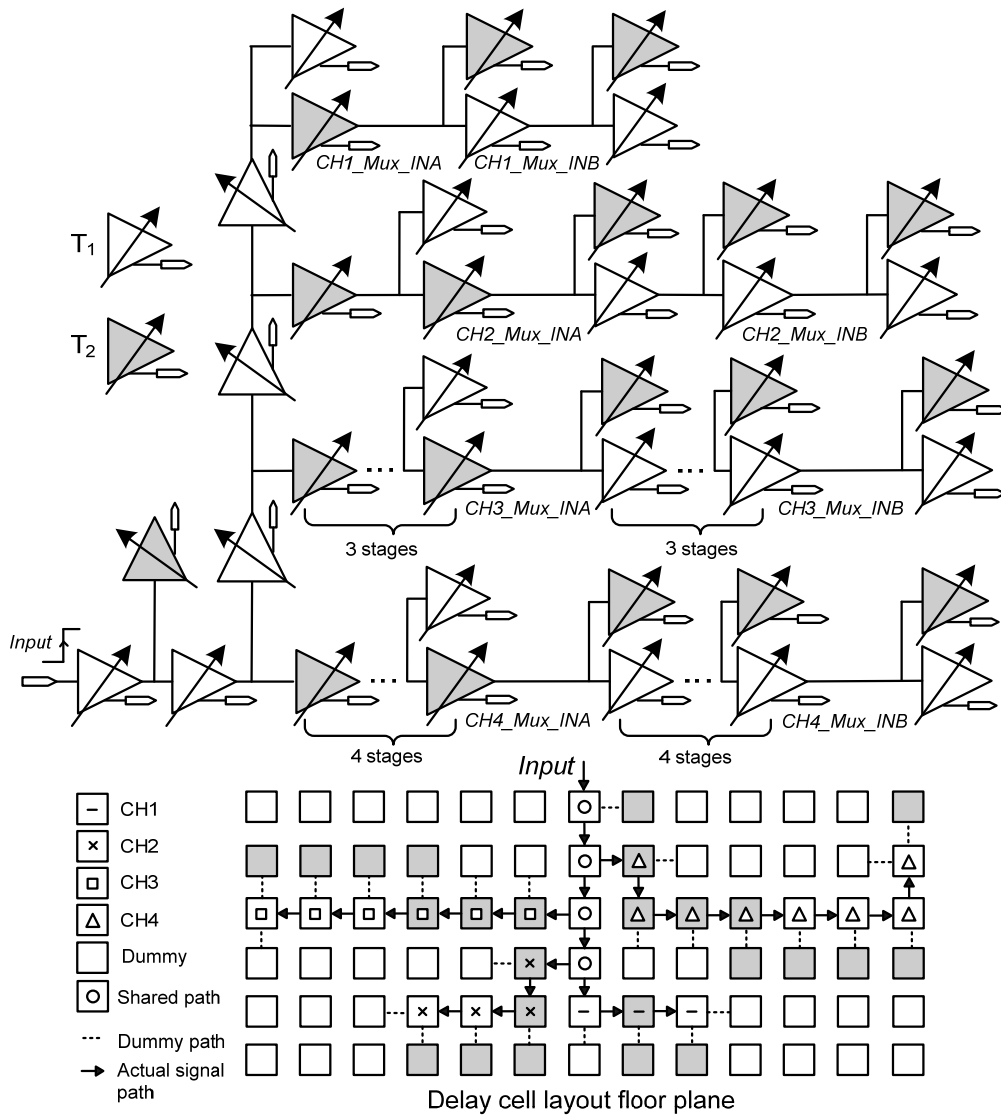
Figure 4.7. The 4-channel matching.

In addition, each delay cell has embedded multiplexer to ensure delay cell matching even though it is only functionally needed at the output delay cell along each path. The floor planning of the delay cells and path connections are shown in Figure 4.7, which clearly illustrates the symmetric loading seen by each delay cells. Through these efforts, 5 ps delay offset is achieved between the four channels in post layout simulation.

4.2.2.   ΔΣ DLL Based Delay Calibration

A. *Counter Based Delay Calibration*

Both the beamforming path delay and UWB center frequency depends on accurate digital delay. Therefore, delay calibration is crucial for our design. As mentioned earlier, counter based with external reference is commonly adopted technique to achieve the desired calibration. In this method, the delay cells are put into a ring to form a DCO [17] as shown in Figure 4.8. The DCO outputs are counted by divider and counter circuits. The output phase is then compared with a reference clock by early/late detector. The result is then used to adjust the DCO frequency. SAR approach is commonly adopted to adjust the DCO setting to minimize the number of steps needed.
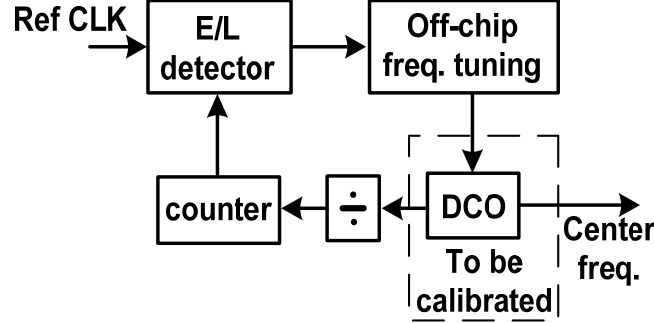
Figure 4.8. Counter based delay calibration adopted by [17].

To quantitatively understand this counter based delay calibration approach, the waveform illustration is shown in Figure 4.9. Suppose the delay of a single delay cell is T_d. The delay cells can form a K-stage ring oscillator ($T_{OSC}=2KT_d$) to drive a counter for a known period (T_{Gate}). The resulting count within T_{Gate} is

$$T_{Gate} = (N \pm 1) \times 2KT_d , \qquad\qquad (4.1)$$

where N is the resulting integer count number. Given a count uncertainty of ± 1 due to the edge uncertainty at the beginning and ending period of T_{Gate}, the resulting timing error could be within the range of ± 3.6 ns with 3 stages ring oscillator and T_d of 600 ps. This timing error can be reduced with larger number of count (N), i.e. longer T_{Gate}. This results in a trade-off between calibration accuracy and time. In order to differentiate delay difference as small as 5 ps within accuracy of 0.5 ps, N as large as 7200 is needed. Also at least two cycles of counting might be required to correctly estimate the delay. This will result in calibration time in excess of 51.84 μs for just one delay calibration. To calibrate the beamforming scan angle from -45° to 90° with 1° step and UWB center frequency of 3.5, 4, and 4.5 GHz, very long delay calibration time will be needed.
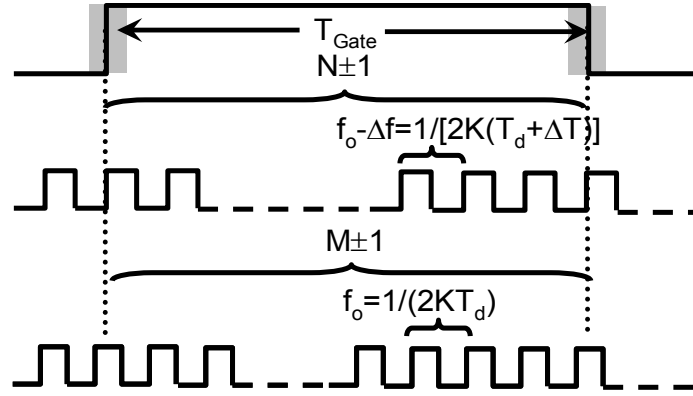
Figure 4.9. Counter based delay calibration waveform.

To shorten the calibration time, PLL based delay calibration could be adopted to calibrate the true time digital beamforming delay [23], as shown in Figure 4.10. The edge uncertainty and frequency truncation error existing in counter

based calibration is eliminated. Accurate calibration could be achieved within the PLL settling time. However, the always on PLL results in very large quiescent current.

In our design, the beamforming subsystem requires large delay range as well as fine delay resolution. Besides beamforming delay, the PVT variations of the transmitter center frequency also have to be compensated through the digital calibration. Therefore, we have to calibrate beamforming delay cells (T_1 and T_2) and UWB transmitter delay cell (T_3) with large delay range, and three PLLs are needed, which may occupy a lot of area and consume very large power. Besides area and power problem, when compared to DLL, PLL has cycle to cycle jitter and is less stable.
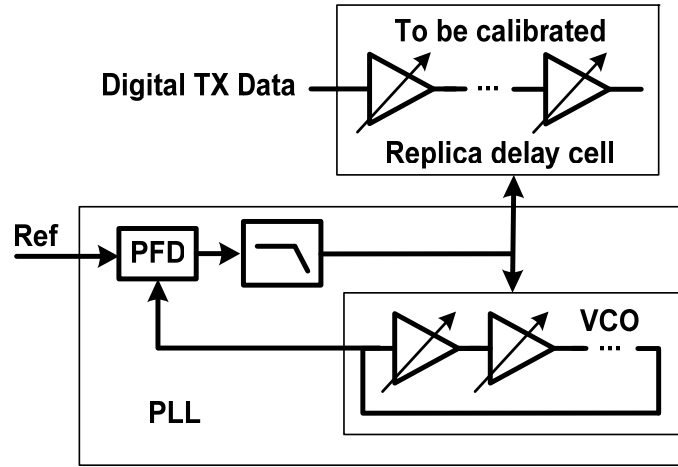
Figure 4.10. PLL based delay calibration in [23].

B. *ΔΣ DLL Based Delay Calibration Process*
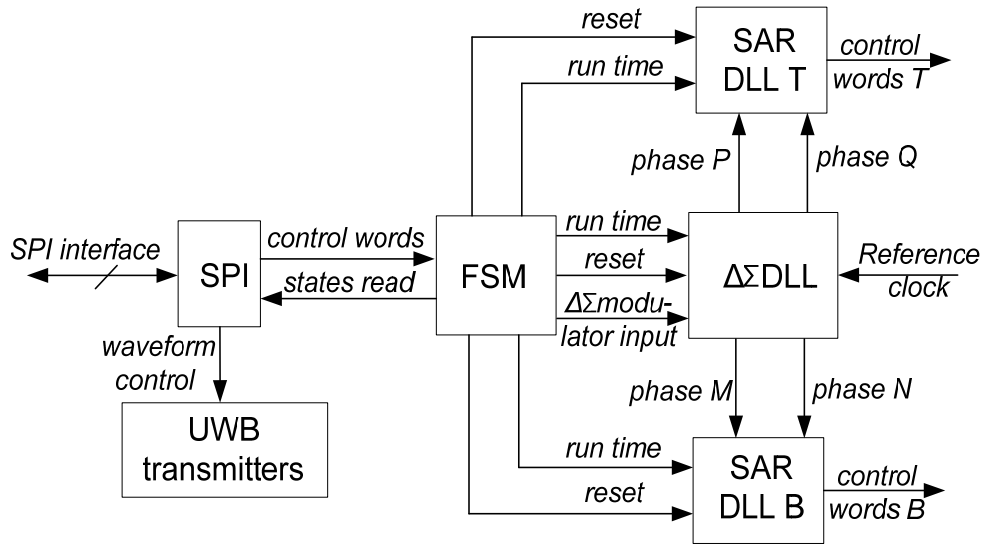
Figure 4.11. The calibration system architecture.

There is a trade-off between calibration time and accuracy for traditional delay calibration methods, so we have to propose a new delay calibration system. Our proposed calibration system architecture is shown in Figure 4.11. It contains SPI, FSM, $\Delta\Sigma$ DLL, SAR DLL for beamforming delay calibration (denoted as SAR DLL B) and SAR DLL for UWB transmitter center frequency calibration (denoted as SAR DLL T). Calibration system plays an important role in the whole system operation for beamforming delay subsystem and the center frequency of the UWB transmitter. To save the limited number of IO pads, all the digital control words are input or output through SPI. The $\Delta\Sigma$ DLL has a reference clock input, and could provide time windows for UWB transmitter calibration SAR DLL and beamforming delay calibration SAR DLL. These two SAR DLLs have the replica delay line of UWB transmitter and beamforming delay circuit respectively. Off-line calibration is adopted, so their power consumption is not critical.

$\Delta\Sigma$ DLL is adopted because it can provide accurate timing with fine delay resolution and good jitter performance [40]. Two SAR DLLs are employed to

provide tuning control for beamforming delay cell (T_1 or T_2) and UWB pulse generator delay cell (T_3). For beamforming, 5-stage delay cells are used with each delay cell covers from 300 ps to 720 ps. For UWB pulse generator, 10 stage delay cells are used with each delay cell having delay ranges from 222 ps to 285 ps. Hence, the total delay from these two SAR delay chain will cover from 1.5 ns to 3.6 ns.

To relax the $\Delta\Sigma$ DLL design, the whole delay range is divided into three smaller pieces, 1.5ns - 2ns, 2ns - 3ns and 3ns - 3.6ns. In the proposed calibration, two delay edges from $\Delta\Sigma$ DLL are chosen to form the timing window to calibrate these delay pieces for the SAR DLLs to lock in. These pieces of delay are provided by time window of (P5-P2), (P7-P2) and (P9-P2) respectively. P2, one of the delay edges from $\Delta\Sigma$ DLL, will be input to a chain of digitally controlled delay cells (T_1, T_2 or T_3). So the delayed output will then be compared through a SAR controller with another delay edges (P5, P7 or P9) from $\Delta\Sigma$ DLL. The SAR controller will generate the control words corresponding to the desired delay. In this way, the beamforming path delay (T_1 or T_2) and UWB pulse generator delay (T_3) are calibrated.
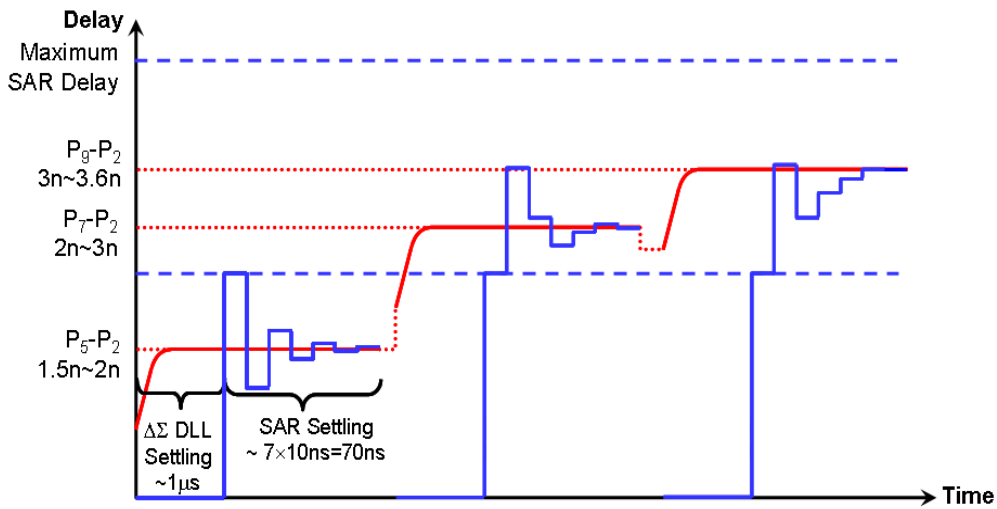
Figure 4.12. $\Delta\Sigma$ DLL based calibration process.

The whole calibration process is shown in Figure 4.12. To calibrate the first delay piece, the ΔΣ DLL is turned on first. After it settles down, its output phases (P5-P2) will be used as time window for SAR DLL to lock in. The SAR DLL will then adjust its own delay chain to match the delay difference of P5-P2. Once the SAR DLL settles, the delay control corresponding to the desired delay would be found and the calibration will move on to calibrate subsequent delay setting. The process will repeat until all the digital delay setting corresponding to the desired delay has been found. As mentioned earlier, different delay difference from ΔΣ DLL will be used to calibrate different delay range. In this implementation, 200 MHz reference is used for ΔΣ DLL which allows larger loop bandwidth and faster settling time of 1 μs. The SAR controller is running at 100 MHz and it takes 7 cycles (70 ns) to obtain the desired delay controlling words. Hence, the total calibration time is less than 1.1 μs.

Therefore the total calibration time as shown in Figure 4.12 is shortened to 1.07 μs which is about 48 times faster than counter based approach. It also attains higher accuracy (theoretically < 0.035 ps, as will be discussed later) by avoiding the edge uncertainty. These are achieved at the expense of larger area (7% of total die area). It should be pointed out that large area incurred by FSM is not considered as it is mainly consumed by the storage registers needed for various delay settings. Same amount of area would be needed by counter based approach. However, this area could be reduced with advanced technology or by employing SRAM generator. There is no additional power penalty for the proposed technique as off-line calibration is adopted.
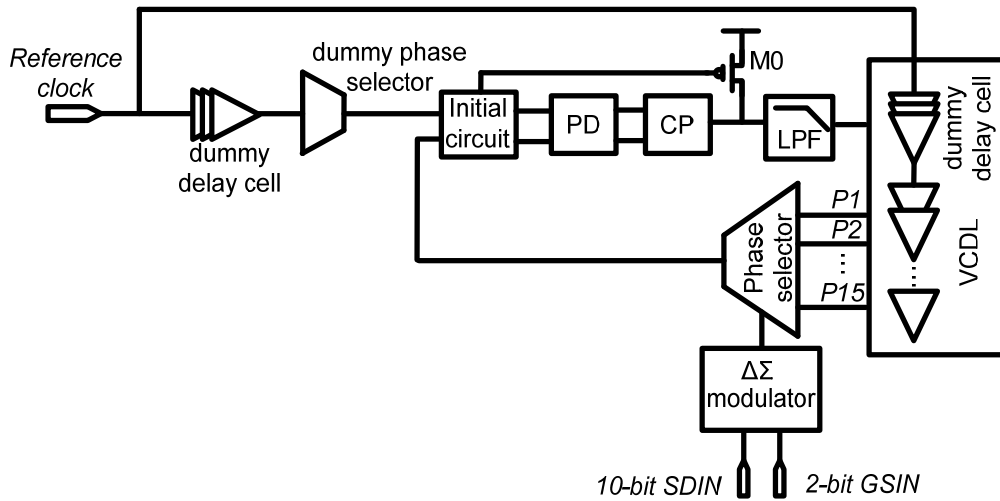
Figure 4.13. The structure of ΔΣ DLL.

Normally an ordinary DLL compares reference clock with the delayed phase by PD. It locks to one period of the reference clock and can provide the required delay based on the reference clock period. However, ΔΣ DLL employs ΔΣ modulator to dynamically select the multi-phase feedback clocks produced by the ΔΣ DLL and then fed its selection to the PD, as shown in Figure 4.13. The resulting action would be an average clock phase that matches the input reference period. Therefore, ΔΣ DLL has the capability to generate a fractional delay without the need of additional phase interpolator. It also eliminates the requirement of a long delay chain to produce delay with very fine resolution. For example with a reference clock frequency of 200 MHz, and with a delay line consisting of 15 delay cells, by using the output phases from delay cells 7 to 14 and averaging the phases with a ΔΣ modulator, very fine delay resolution (theoretically < 0.035 ps, shown later) can be achieved.
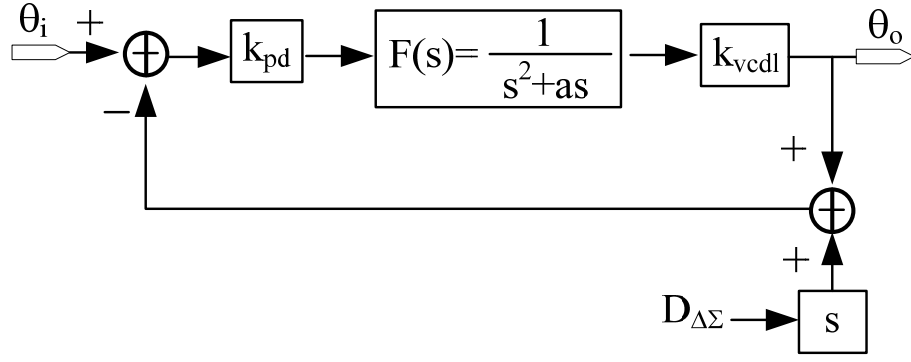
Figure 4.14. The linear model of $\Delta\Sigma$ DLL.

To illustrate the operation principle of this $\Delta\Sigma$ DLL, its linear model is shown in Figure 4.14. The $\Delta\Sigma$ modulator introduces quantization noise in the form of delay. In the core loop, K_{pd} is the gain of phase detector. The loop filter F(s) typically adopts integrator to achieve zero static phase offset with phase step input. Here a second order loop filter is adopted to suppress the first order $\Delta\Sigma$ modulator quantization noise. The voltage controlled delay line has delay gain of K_{vcdl}. Therefore, the core loop transfer function could be expressed as

$$H(s) = \frac{G(s)}{1+G(s)} = \frac{k_{pd}k_{vcdl}}{s^2 + as + k_{pd}k_{vcdl}}, \tag{4.2}$$

where G(s)= K_{pd} F(s) K_{vcdl}, it is the open loop transfer function. The selection of these parameters will be shown in detail later in the loop filter part.

C. The $\Delta\Sigma$ Modulator
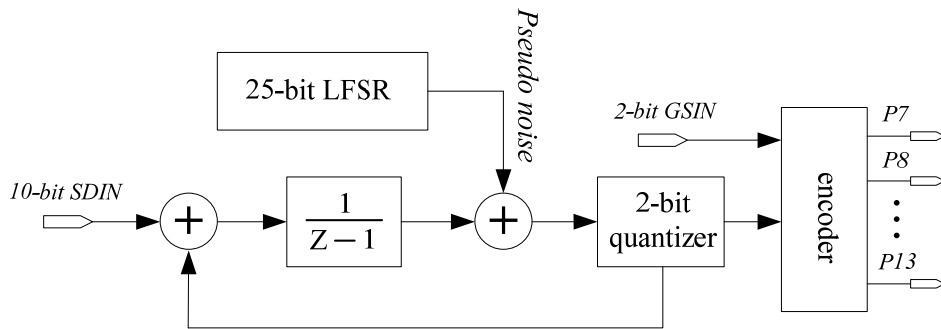
Figure 4.15. The first order $\Delta\Sigma$ modulator.

A first order ΔΣ modulator with a 2-bit quantizer is used in this design as shown in Figure 4.15. To generate an average value, it can switch between 4 phases of the multi-phase feedback clock. The ΔΣ modulator has two sets of inputs. The 2-bit group selection input *GSIN* could choose the group of clock phases for averaging. 10-bit input *SDIN* decides the average value. Due to the wide delay range required for calibration, we employ 4 different groups (controlled by *GSIN*) of multi-phase feedback clock, i.e. P7-P10, P8-P11, P9-P12 and P10-P13.

Due to the poor randomization of first order ΔΣ modulator, a pseudo-random noise generator is introduced within the modulator to achieve the desired noise shaping shown in Figure 4.16. The noise shaping would be higher if we adopt higher order ΔΣ modulator. Higher order modulator is not adopted here to simplify the loop filter design.
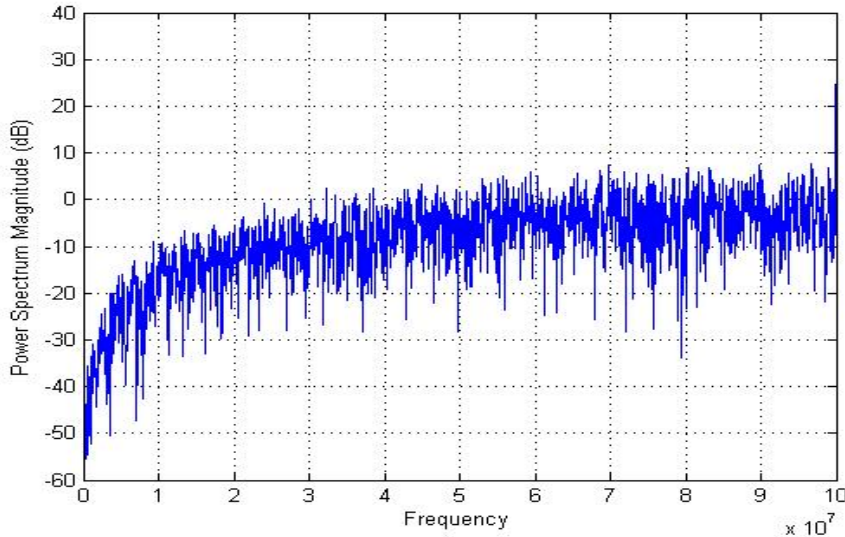
Figure 4.16. The first order ΔΣ modulator spectrum.

Similar precautions mentioned in [40] are taken to minimize delay cell mismatch. The 10-bit *SDIN* determines the average number (*N*) of delay cells that the input clock goes through and thus the desired delay of VCDL could be generated. The average N value can be estimated as follows:

$$N = 8 + GSIN + \frac{-2^8 + SDIN}{2^9},$$
(4.3)

where *GSIN* varies from 0 to 3, and *SDIN* varies from 0 to (2^{10}-1). The synthesized *N* value ranging from 7.5 to 12.5 with minimum step of 2^{-9} could thus be achieved. The delay of VCDL delay cell is given as

$$T_{delay} = \frac{T_{ref}}{N},$$
(4.4)

where T_{ref} is 5 ns (f_{ref} is 200 MHz). With *N* varying from 7.5 to 12.5, the delay cells delay can then be tuned from 400 ps to 667 ps. So the phase difference of (P5-P2) could generate time window covering 1.5 ns – 2 ns; the phase difference of (P7-P2) could generate time window covers 2 ns – 3 ns; the phase difference of (P9-P2) could generate time window covers 3 ns - 3.6 ns. By using these three different set of phase difference, we could thus calibrate delay ranging from 1.5 ns to 3.6 ns. As the two consecutive *SDIN* inputs determine the achievable delay step and given that the delay is inversely proportional to *N*, the worst delay step occurs when two consecutive *SDIN* inputs give rise to smallest *N* value as

$$T_{step} = \frac{T_{ref}}{8 + GSIN + \frac{-2^8 + (SDIN+1)}{2^9}} - \frac{T_{ref}}{8 + GSIN + \frac{-2^8 + SDIN}{2^9}}.$$
(4.5)

The value is in the range of smaller than 0.035 ps, which is much smaller than the desired beamforming delay step of 10 ps.

A 25-bit linear feedback shift register (LFSR) based pseudo-random generator is added before the quantizer input to achieve better randomization for the ΔΣ

modulator.

D. Voltage Controlled Delay Line (VCDL) and Phase Selector

The schematic of the VCDL with phase selectors is shown in Figure 4.17. A total of 15-stage delay cells with phase selectors are used to construct the VCDL, although we only employ the feedback clock phases from P7 to P13. Several dummy delay cells are added to eliminate the loading effect of the delay cells. Every delay cell is followed by a phase selector. Only one phase could be selected every clock cycle. The P14 and P15 stages are used to improve matching. All these efforts will minimize the phase mismatches between P7 and P13 and lead to better delay accuracy.
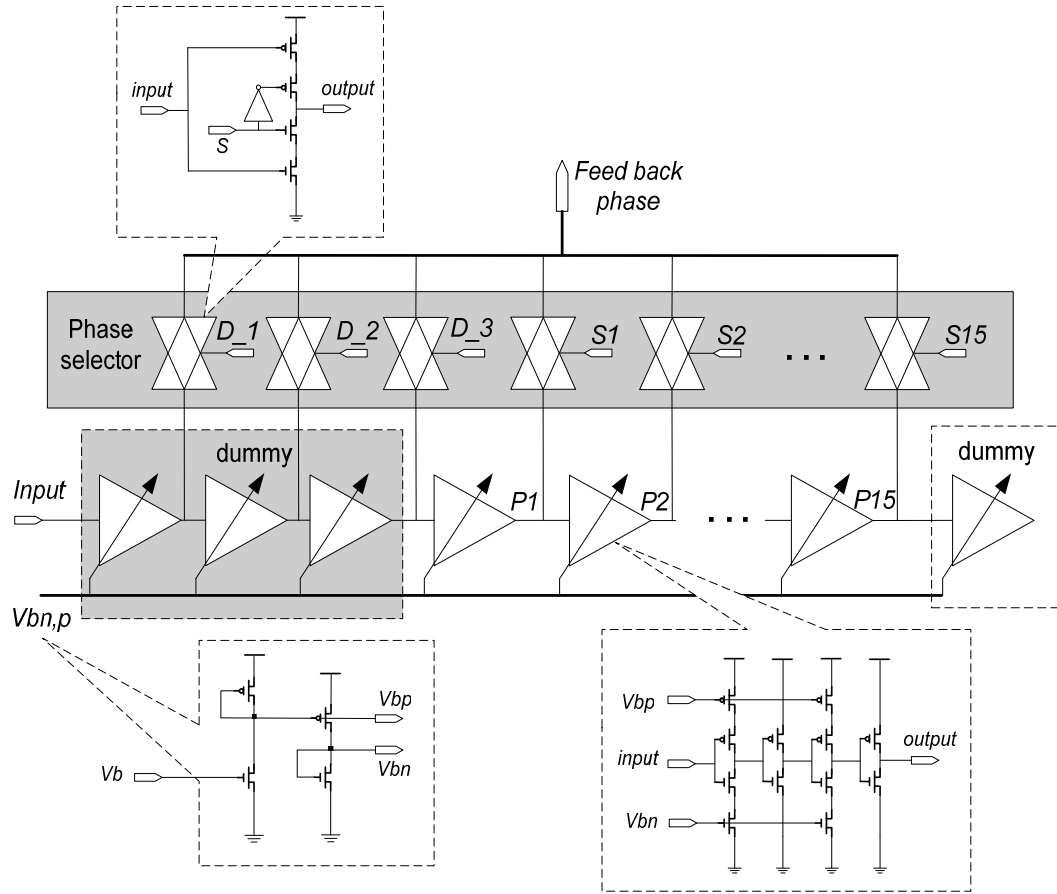
Figure 4.17. VCDL and phase selector.
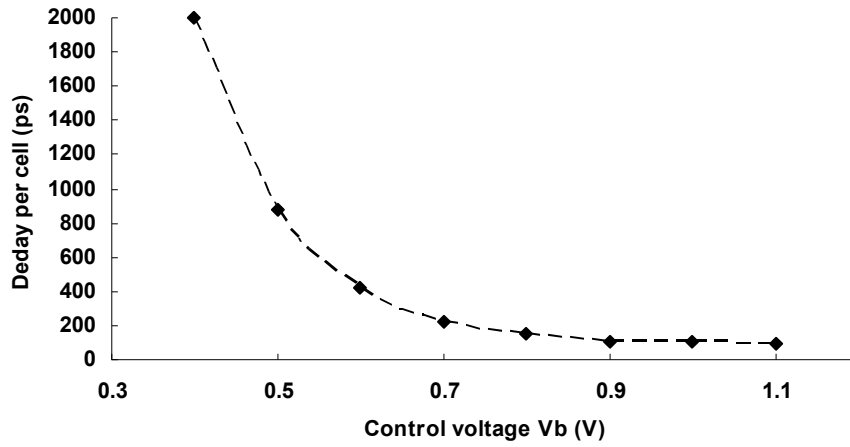
Figure 4.18. The generated delay per cell under control voltage *Vb*.

The delay control voltage *Vb* comes from the loop filter. It is then mapped into Vbn and Vbp to provide current control for the current starving inverter as shown in Figure 4.17. Identical phase selector is adopted after every delay cell to ensure good phase matching. The generated delay per cell under control voltage *Vb* is shown in Figure 4.18.

E. *Phase Detector and Startup Circuit*
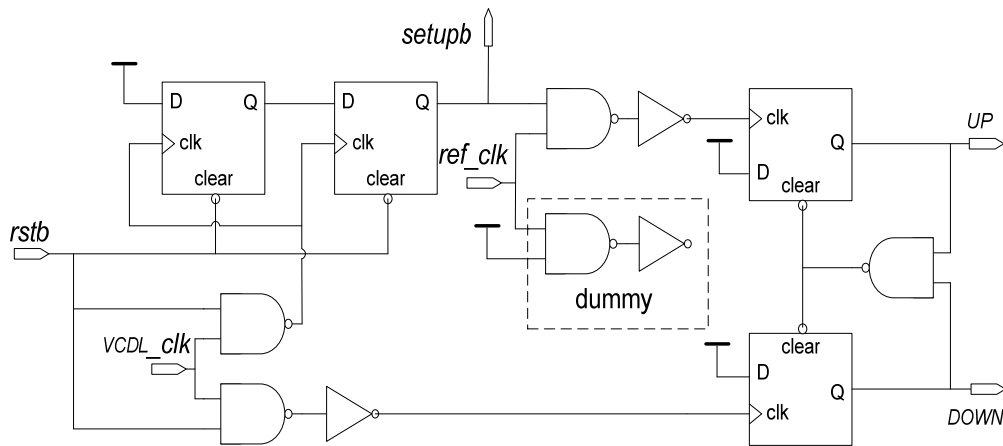
Figure 4.19. Phase detector and startup circuit.

For DLL, anti-harmonic locking detection circuit is commonly adopted to avoid harmonic locking problem [40], but it will incur additional complexity in control. Another method is to set the circuit initial condition by a startup control circuit [48] as shown in Figure 4.19. Initially, *setupb* will be kept low by *rstb*. This low *setupb* ties up transistor M0 in the system structure (in Figure 4.13) to make the delay line generate smallest delay. Therefore, the harmonic locking problem is avoided initially, and the anti-harmonic locking blocks could be eliminated.

Two D Flip-flops are included in the phase detector to eliminate the initial phase comparison. This is because the feedback clock is only available after two reference clock cycle. To eliminate dead zone issue, 250 ps delay is built into the feedback NAND gate. This will help reducing the reference spur at the output.

F. Charge Pump and Loop Filter

The charge pump is shown in Figure 4.20. Transmission gate is introduced to match the additional delay along the UP signal path due to inverter. High swing cascode is employed to minimize the charge pump mismatch between the PMOS and NMOS. At the same time, this charge pump design mitigates charge injection errors induced by the parasitic capacitance of the switches and current source transistors [49].
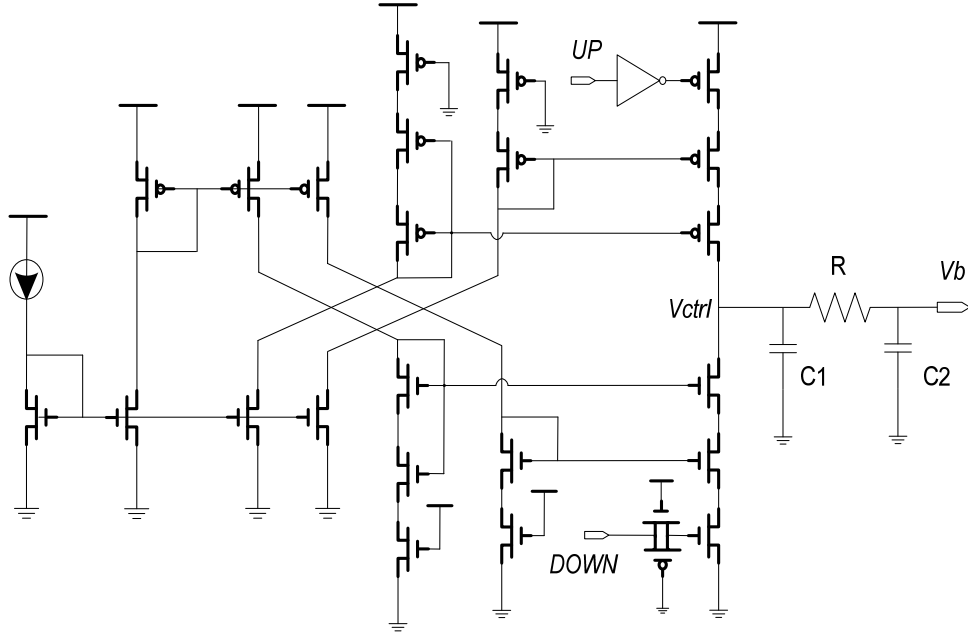
Figure 4.20. Schematic of charge pump with loop filter.

The loop filter is a passive second order filter network consisting of a resistor and two capacitors as indicated in Figure 4.20. Second order filter is adopted to suppress noise due to first order $\Delta\Sigma$ modulator noise shaping as shown previously. The transfer function of the loop filter is given by

$$F(s) = \frac{V_{CTRL}}{I_{CP}} = \frac{1}{s^2(C_1C_2R) + s(C_1 + C_2)}. \tag{4.6}$$

By assuming that the two poles are far apart (this is valid because $C_1 \gg C_2$), the two poles can be estimated by

$$\omega_{P1} = \frac{F_{REF}K_{VCDL}I_{CP}}{C_1}, \tag{4.7}$$

and

$$\omega_{P2} = \frac{1}{RC_2}. \tag{4.8}$$

The first pole determines the loop bandwidth and thus the jitter performance as well as the settling time of DLL. Smaller loop bandwidth will result in better

jitter performance with slower response. Given a charge pump current of 1 mA, a reference frequency of 200 MHz and delay gain (K_{VCDL}) of 4.25 ns/V, a capacitor (C_I) of 50 pF will result in loop bandwidth of 2.7 MHz. Far away second pole is then chosen through by selecting C_2 to be ten times smaller than C_I and R of 12 kΩ

$$f_{BW} = \frac{\omega_{P1}}{2\pi} = 2.7 MHz \tag{4.9}$$

G. SAR DLL Structure
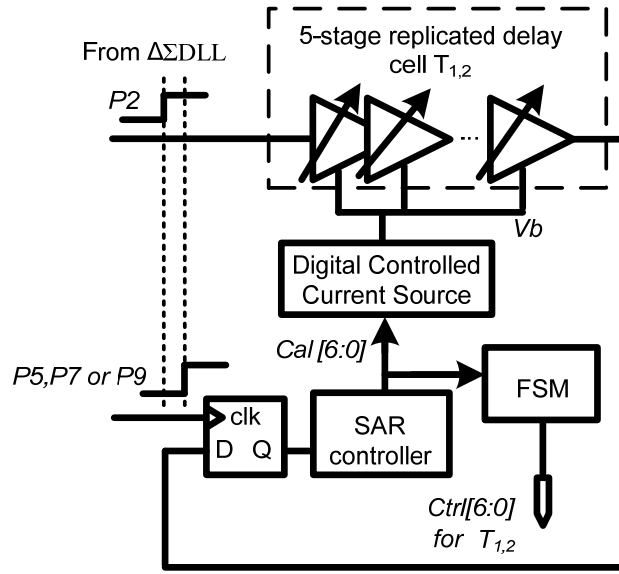
(a)
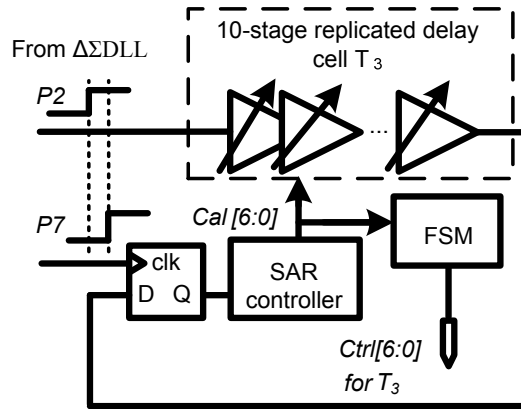
(b)

Figure 4.21. The architecture of SAR DLL: (a) For beamforming delay calibration; (b) For UWB pulse center frequency calibration.

The architectures of SAR DLL adopted in this design are shown in Figure 4.21. The architecture is similar for both beamforming delay and UWB pulse generator. They only differ in the number of delay stages used and the phase difference coming from ΔΣ DLL.

SAR DLL only requires N-step to finish the search and could thus result in fast locking time. Once locked, its delay control word will be stored in FSM for subsequent control of beamforming path delay or UWB generator delay.

H. FSM
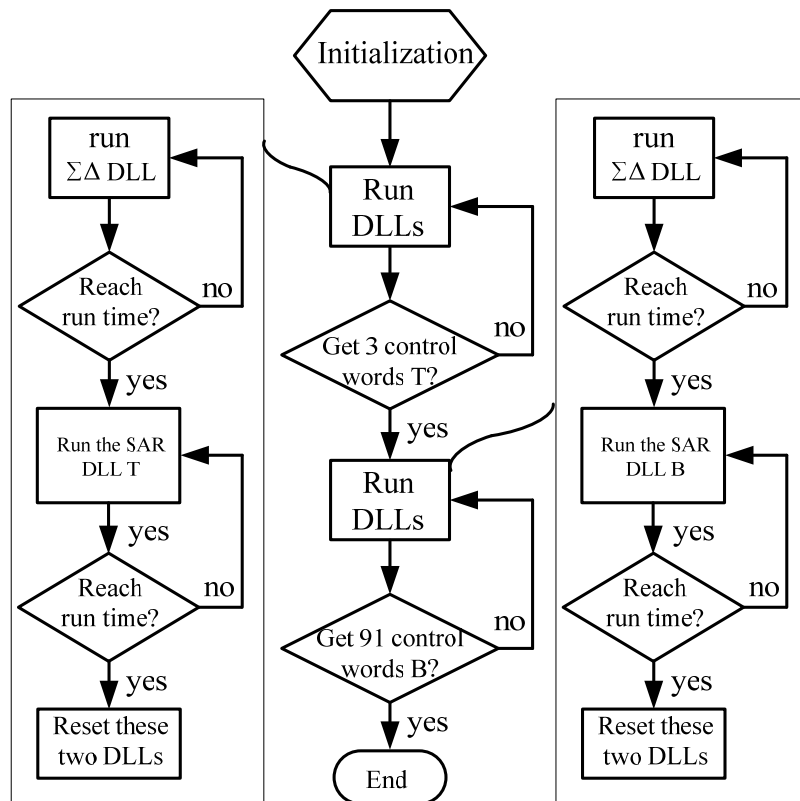
Figure 4.22. The flow chart of FSM.

The flow chart of FSM is shown in Fig. 4.22. After initialization, the calibration will kick start to calibrate the 3 delay control words needed for UWB pulse generator first. The calibrated 3 delay control words will be stored in registers for subsequent use. Once the UWB pulse generator calibration is done, the FSM will move on to beamforming delay path calibration. Here 91 delay control words will be calibrated. It should be pointed out that 46 control words used for 0-45° can be used for 0 - -45° by simply swapping the control word for T1 and T2. As mentioned earlier, ΔΣ DLL will need to settle before SAR DLL operates. Hence, the FSM will allocate a preset time interval for ΔΣ DLL to settle. The FSM will also turn off ΔΣ DLL and SAR DLL to maximize energy efficiency.

4.2.3.   UWB Transmitter Architecture

A. *The Consideration of UWB Transmitter for Beamforming*

As mentioned in the literature review part, there is a trade-off between energy efficiency and output power for different transmitter architectures. Ref [17] can achieve good energy efficiency due to its architectural simplicity. However, one critical issue with such approach is the pulse shrinking through buffer chains due to the narrow pulse width (111 ps). This often requires large buffers to speed up the rise/fall time to avoid pulse shrinking. The problem worsens with older technology as shown in Figure 4.23. From our study, with a poorer technology node at 0.13 μm, the technique fails to generate decent UWB pulse even by burning significant power.
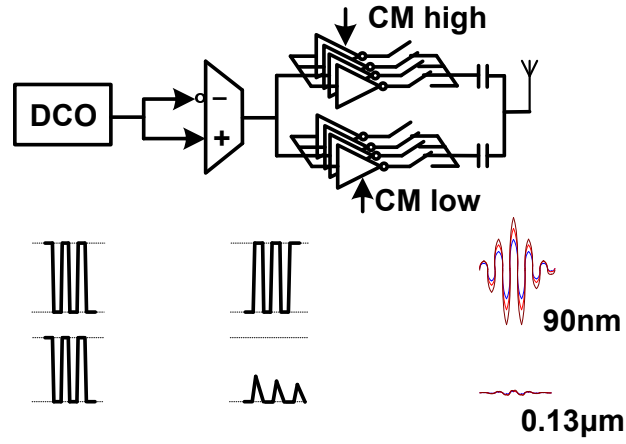
Figure 4.23. The UWB transmitter architecture in [17] and generated pulse shape in 90nm and 0.13μm process.

B. The Proposed UWB Transmitters

To overcome this pulse shrinking issue and achieve better energy efficiency, we propose to send the delay edges instead of pulses to the PA, as shown in Figure 4.24. The UWB pulse is only generated through edge combining at the digital PA locally. This relaxes the rising/falling time and thus driving strength requirement, and results in better transmitter energy efficiency. The highly repetitive structure also eases the layout design. With programmable digital PA, the tunable UWB pulses could be generated.
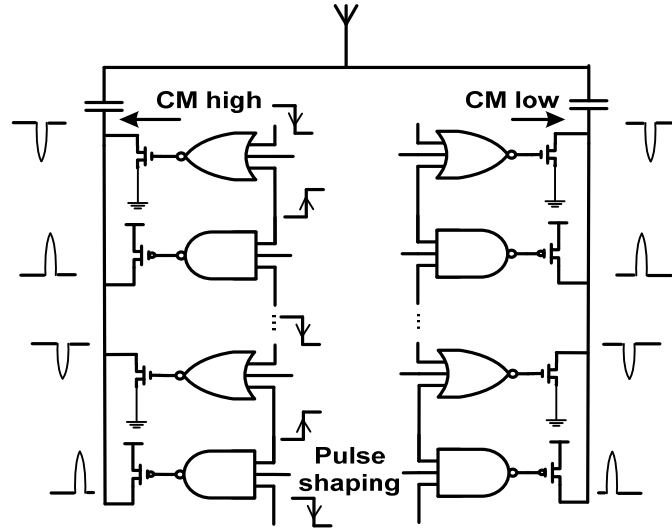
Figure 4.24. The structure of propsed UWB transmitter.

The whole circuit is shown in Figure 4.25. It mainly consists of two branches of identical programmable digital PA and a 7-bit digitally controlled delay line which could generate delayed edges. This compact structure minimizes the variation of the four UWB transmitter outputs.

The input triggering signal is first sent through a chain of digitally controlled delay line (DCDL). The resulting delay edges are then combined through NOR or NAND gate locally to drive the PA. Short pulses will be formed at the digital PA output. The dual digital PAs are composed of upper and lower pulse generators.

Figure 4.25. The structure of UWB transmitter.

Similar to [17], dual capacitively-coupled technique with pre-charge transistors is also employed to connect the dual digital PAs for AC signal. The dual digital PAs are biased to GND and VDD with pre-charge and pre-discharge transistors respectively. Through ac coupling, the combined pulse from the dual digital PAs will suppress low frequency components. The pre-charge and pre-discharge transistors will be turned off by pre-charge signal

generator when the pulses are generating to eliminate short circuit current.

To provide pulse shaping capability, each locally generated pulse has eight identical pulse generators with corresponding control words C<N:N+7> in parallel. Therefore, eight levels of amplitude tuning are provided to make the pulse shape tunable. The DCDL comprises five delay cells (T_3). Each delay cell has two digitally controlled 7-bit current starved inverters for center frequency tuning. The delay line control is obtained from the calibrated delay control discussed earlier.

4.2.4. PSDC Circuit

A. The Architecture of PSDC Circuit

With the proposed UWB pulse generation circuit, the resulting 10 pulses with 8 different levels of amplitude control for each pulse will result in billion combinations. Fortunately, UWB pulse shape is well known and we do not have to exhaust all the combinations. However, due to the imperfection of circuits, parasitic, loading and filtering effect, the resulting UWB pulse might differ from the designated pulse shape. Therefore, PSD measurement and pulse shape tuning needs to be provided to compensate for potential pulse shape distortion. It has been observed that a good UWB pulse shape has PSD with small low frequency components. FCC spectral mask requires a ratio of at least 34dB between the peak of transmitted spectrum (3.5-4.5GHz) to the spectrum at lower frequency. Therefore, we proposed PSDC circuit to measure such ratio to determine the quality of the resulting UWB spectrum. The obtained information can then be feedback to the FPGA to fine tune the NPG and PPG units in the digital PA and thus the spectrum. The idea is illustrated

conceptually in Figure 4.26.
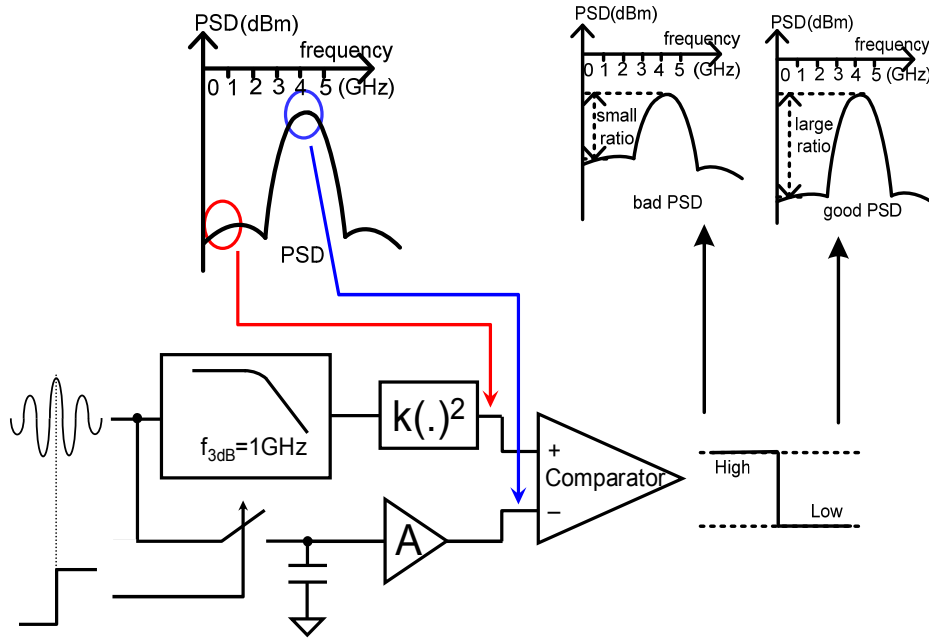
Figure 4.26. The PSDC principle.

A replica UWB transmitter is included to mimic the actual transmitter output. Its output is fed into two separate paths for energy detection at two different frequency bands, e.g. a low frequency band of less than 1GHz and a high frequency band at center frequency. For low frequency path, the energy is extracted through a lowpass filter ($f_{3dB} \approx 1GHz$) followed by an energy detector. For peak transmitted energy, instead of employing a bandpass filter, we use track-and-hold circuit to capture the peak of the UWB pulse, which bears certain correlation with the peak transmitted energy. This is feasible because we know the exact occurrence of the peak in UWB transmitter. The gain along both paths is adjusted such that a ratio of at least 34 dB between the two is observed when the resulting UWB spectrum is good. The two path signals are compared with a comparator.

As shown in Figure 4.26, good UWB pulses trigger the comparator to output a low state when the gain along the low frequency path is adjusted properly. To obtain a reasonable gain setting for low frequency path, we generate a stream of UWB pulses with different pulse shapes by adjusting the control words in both UWB pulse generator and digital PA. These pulses contain certain percentage of good UWB pulses. By starting with a low gain value, we count the number of "Low" in the comparator output for a given stream of UWB pulses. If the percentage of "Low" roughly matches the percentage of the good pulses in UWB pulses stream, the gain setting is said to be proper. Otherwise, the gain needs to be increased until a match is found. Then an optimum pulse shape could be found among different pulse shape combinations.

B. The Implementation of PSDC Circuit

The actual implementation is shown in Figure 4.27. For the low frequency energy extraction path, simple RC low pass filter and differential amplifier with resistive load are employed and both have a bandwidth of about 1 GHz. The signal is then passed to a squarer and integrator for energy detection. To maintain differential path for better common mode noise rejection, an identical path with zero input is duplicated.
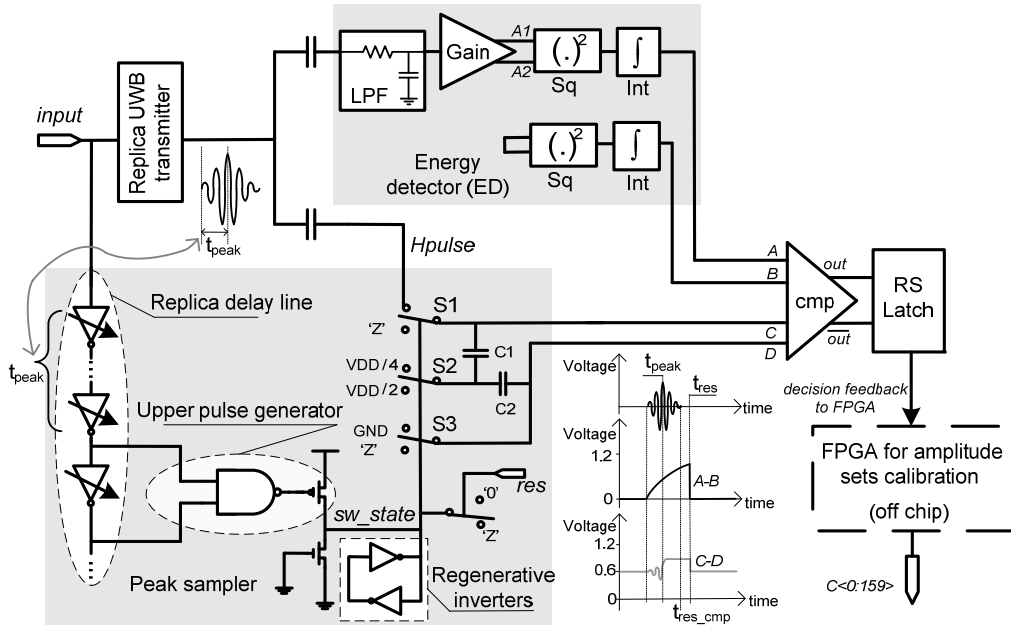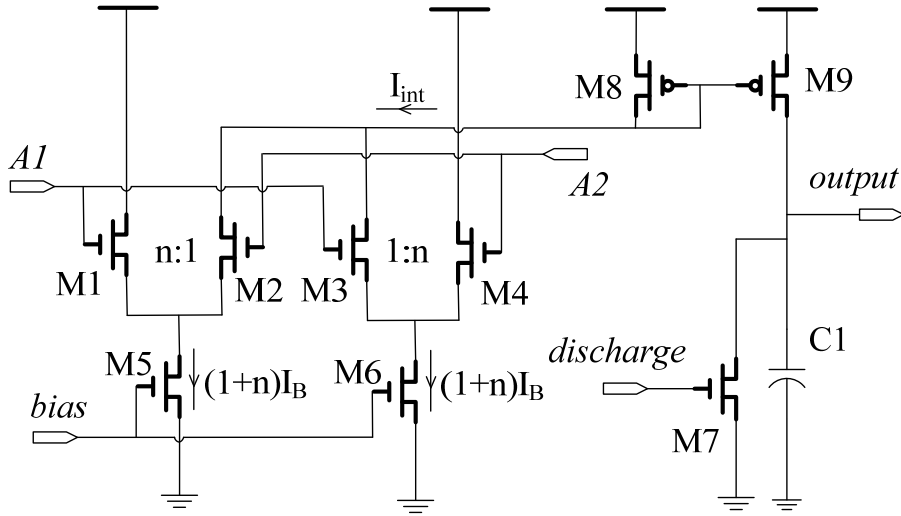
Figure 4.27. The PSDC circuit.

Figure 4.28. The squarer and integrator circuits in PSDC.

The low pass filter and gain stages are simple. The design of squarer circuit is worth mentioning here. The detail schematic of squarer and integrator circuit in PSDC is shown in Figure 4.28. The output current of squarer I_{int} is determined by

$$I_{int} = I_{D2} + I_{D3}. \qquad (4.10)$$

91

This current should be related to the differential input voltage V_d, which is shown in Figure 4.28 as

$$V_d = V_{A2} - V_{A1},$$

(4.11)

where V_{A2} is determined by

$$V_{A2} = \sqrt{\frac{2I_{D2}}{k_N}}.$$

(4.12)

Ideal long channel NMOS current to voltage characteristic is used here. k_N =$(W/L)\mu_n C_{ox}$, μ_n is electron mobility, and C_{ox} is gate capacitance. (W/L) is the form factor of M2, while M1 is n times bigger. In the same way, we can get the V_{A1} as

$$V_{A1} = \sqrt{\frac{2I_{D1}}{nk_N}}.$$

(4.13)

Since the current output of M1 drain is

$$I_{D1} = (n+1)I_B - I_{D2},$$

(4.14)

then the Equation 4.11 becomes

$$V_d = \sqrt{\frac{2I_{D2}}{k_N}} - \sqrt{\frac{2[(n+1)I_B - I_{D2}]}{nk_N}}$$

$$\approx \sqrt{\frac{2I_{D2}}{k_N}} - \sqrt{\frac{2I_B}{k_N}}.$$

(4.15)

From this equation, we could get the current output of M2 drain is

$$I_{D2} = \frac{k_N}{2}(\sqrt{\frac{2I_B}{k_N}} + V_d)^2.$$

(4.16)

Same analysis from Equation 4.12 to Equation 4.16 could be applied to transistor M3 and M4, and we could get

$$I_{D3} = \frac{k_N}{2}(\sqrt{\frac{2I_B}{k_N}} - V_d)^2.$$

(4.17)

Therefore, the output current of squarer I_{int} is

$$I_{int} = I_{D2} + I_{D3} = k_N V_d^2 + 2I_B.$$

(4.18)

The square function is achieved as shown in this equation. The key assumption in the whole deduction is that the large size of transistor M1 and M4 compared to M2 and M3 as approximated in Equation 4.15. However n times larger transistor size results in n times larger current, so n = 10 is adopted considering this trade-off.

Larger width of M2 and M3 will generate more gain, but larger size also incurs worse parasitic which limit the frequency. Therefore, 5 μm is chosen as the width of M2 and M3, resulting in k_N of about 2 mA/V^2.

After squaring, the energy is integrated on C1. The integrator in another dummy path will get integrate I_B. The resulting difference is the $k_N V_d^2$ which will be sent to one of the differential input pair (*A, B*) of the comparator. The difference of *A* and *B* in Figure 4.27 indicates the lower band power. The low band power detector acts just like a sub-1 GHz receiver based on energy collection.
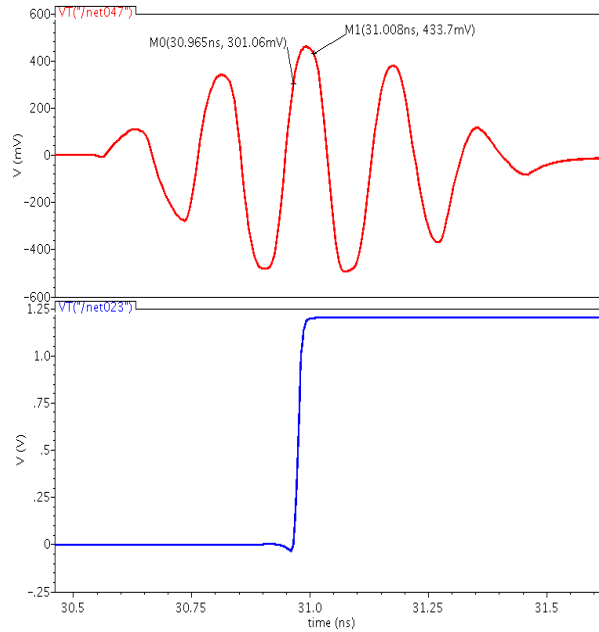
Figure 4.29. The UWB pulse and the switch signal.

The proposed peak voltage extractor using track and hold circuit will suffer from synchronization issue due to timing uncertainty arise from path mismatch. To study this issue, Monte Carlo simulation has been run to investigate the sampling time variation due to device variation. From the study, it is found that the sampling time will vary from 30.965 ns to 31 ns as shown in Fig. 4.29 and 4.30. This will result in the sampled voltage variation from 300 mV to 450 mV. This variation can be compensated by adjusting the gain along lower frequency path.
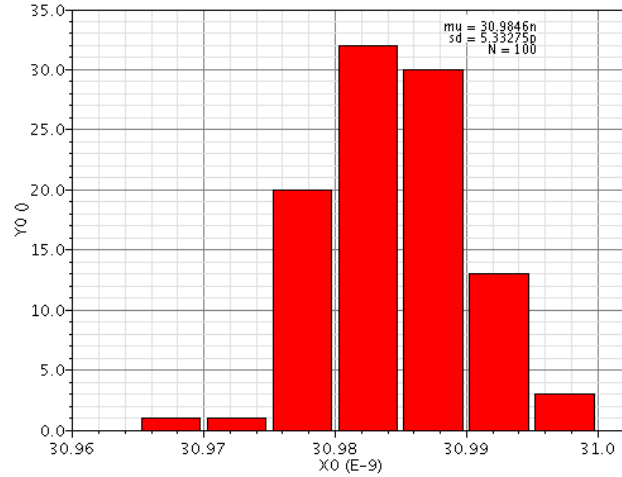
Figure 4.30. The Monte-Carlo simulation of the switch signal.

Therefore, the second branch can sample the peak of UWB signal for the extraction of peak transmitted energy. The *sw_state* is initially reset to zero quickly through *res*. After which, the two regenerative inverters will help maintain the zero state. This zero state will result in the tracking of input signal through capacitor C1 and C2 by closing S1, S2 and S3 at relevant position as shown. The middle of capacitor C1 and C2 is biased to VDD/4 initially. At the exact occurrence of peak signal (t_{peak}), a short pulse is produced through NAND gate to pull *sw_state* to high. The high state is then

maintained by the regenerative inverters again. This high state will now switch the S1, S2 and S3 position such that the peak input signal will be captured by C1 and C2. The captured signal will form another differential pair input (*C, D*) of the comparator.

4.3.   Measurement Results

Fabricated in 0.13 μm CMOS technology, the UWB beamforming transmitter including I/O pads occupies an area of 3 mm × 2.4 mm as shown in Figure 4.31. As illustrated, the four transmitter channels are layout symmetrically around the center of the chip, including their I/O. The beamforming delay chain is centralized to minimize delay mismatch between each path. The delay and PSD calibrations are then placed at both sides of the chip.
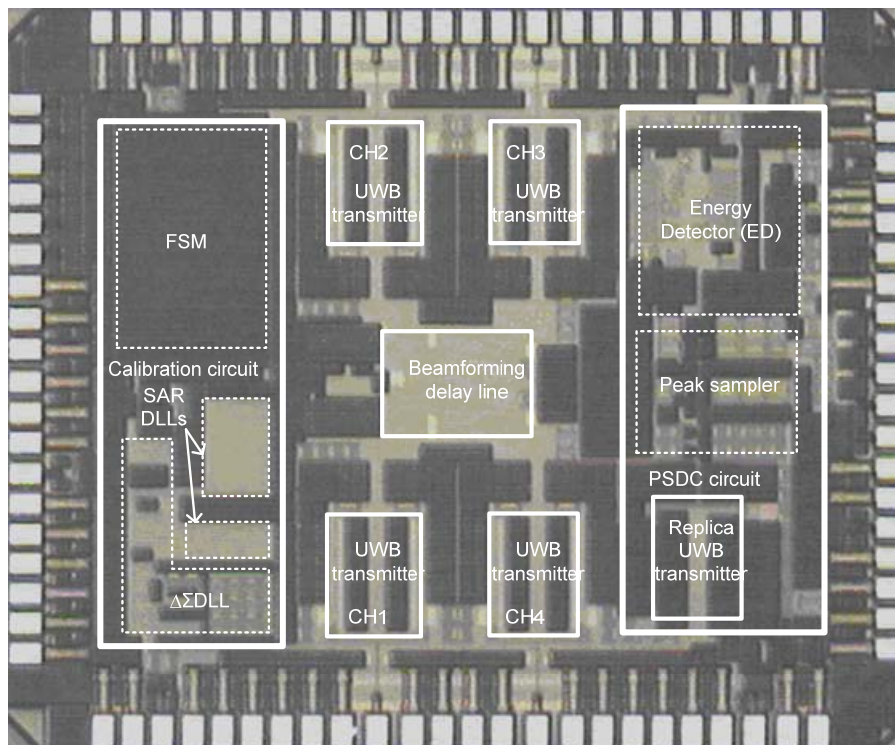
Figure 4.31. Die photo of beamforming transmitter.

Figure 4.32 shows the measurement setup. The 4-channel outputs are also placed symmetrically on the PCB to ensure path matching. The cables connecting them to the antennas are also identical. The whole chip with serial-peripheral interface (SPI) is fully programmable through a laptop and FPGA. A 200MHz reference needed for calibration is provided using Agilent 8133A pulse generator. Measurement with antenna spacing of 18 cm and 30 cm are carried out. To measure the beamforming pattern, the receiver antenna is placed at 2 m away from the transmitters. The received signal is first amplified through two cascaded UWB band LNAs before sending to the spectrum analyzer.
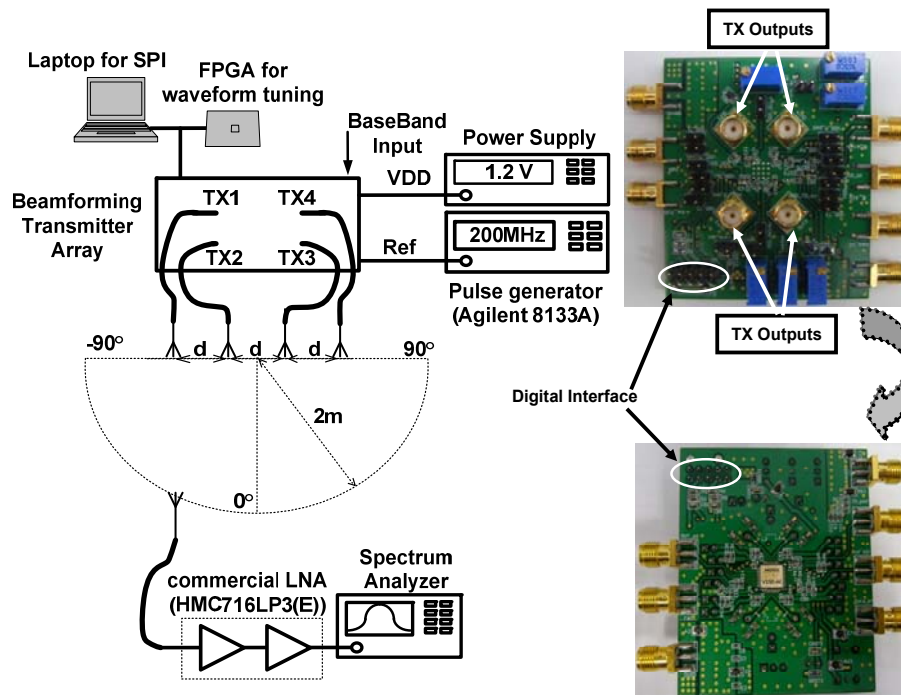
Figure 4.32. Measurement setup.
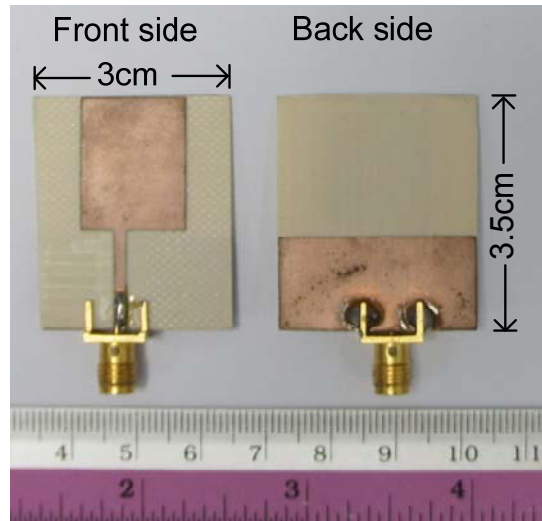
Figure 4.33. The geometry of a single antenna.

Patch antennas as shown in Figure 4.33 with dimension of 3 cm × 3.5 cm are used in the measurement. Its frequency response, characterized by Agilent 8753ES S-parameter vector network analyzer, is shown in Figure 4.34 and Figure 4.35. As illustrated, the antenna has good impedance matching ($S_{11} <$ -10 dB) across the desired 3-5 GHz band.

Figure 4.34. The S_{21} measurement of a single antenna.

S₁₁

Ref: 0dB

10dB/div

CENTER 3 000.000 000 MHz   SPAN 5 999.980 000 MHz
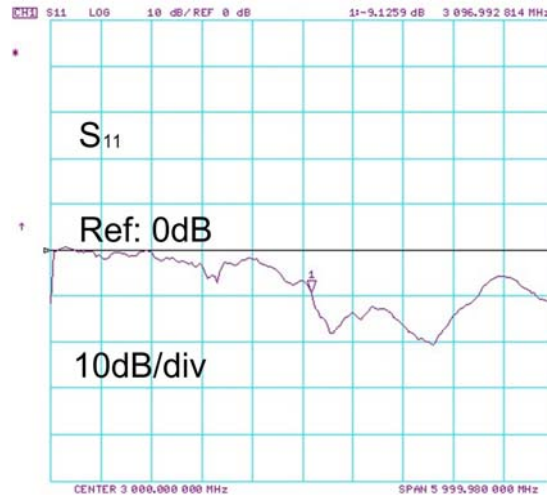
(b)

Figure 4.35. The S$_{11}$ measurement of a single antenna.

For radiation pattern characterization of a single antenna, spectrum analyzer is used to measure the energy at different scanning angle. The collected energies at different scanning angles are then normalized by the maximum energy and are plotted in linear scale on polar plot to establish the radiation pattern. The omni-directional radiation pattern is obtained by only activating one transmitter. As shown in Figure 4.36, the radiation pattern approaches a half-circular form.
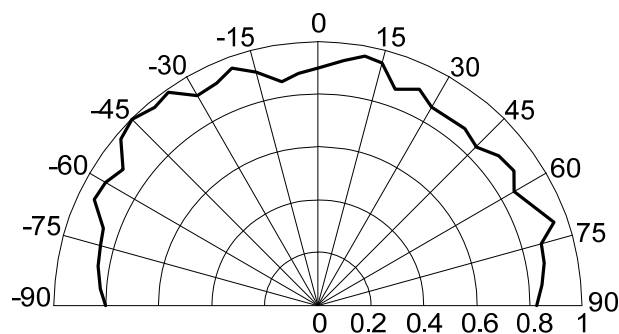
Figure 4.36. The pattern of a single antenna.
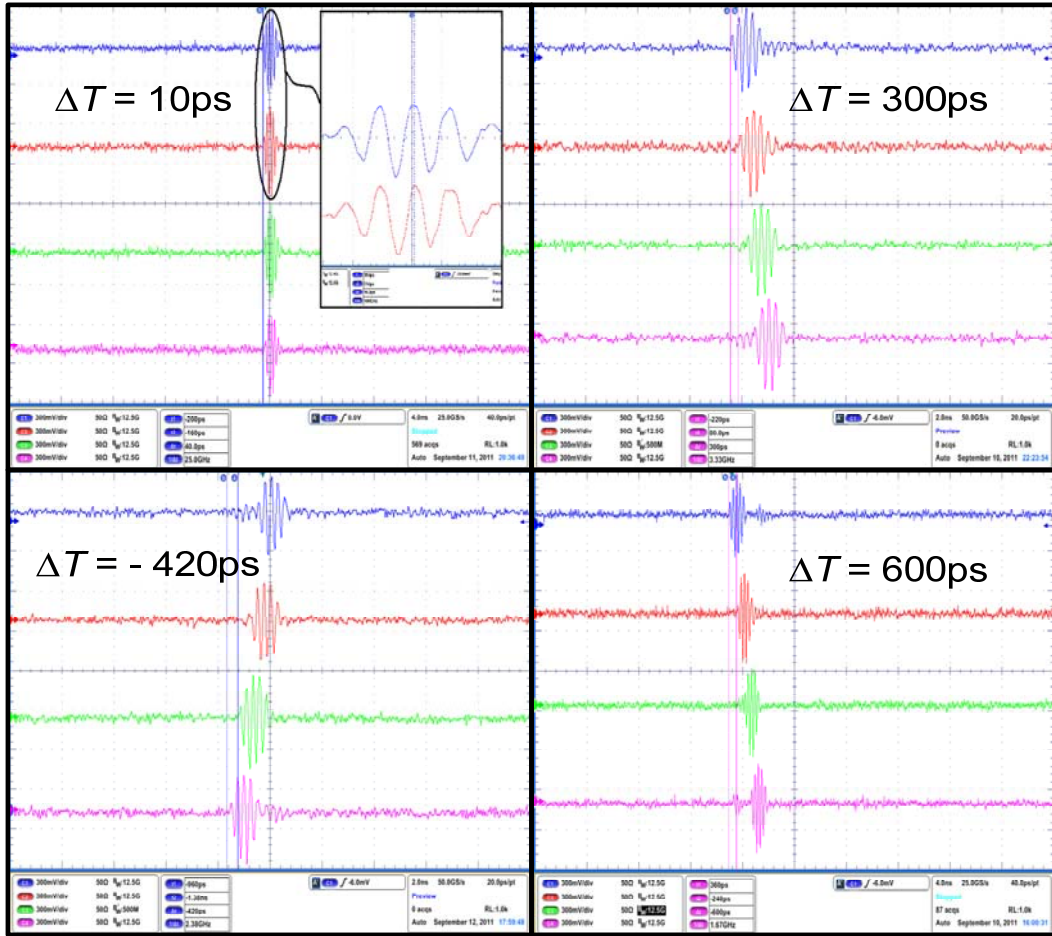
Figure 4.37. The measured waveforms.

The measured time domain UWB pulse waveforms are shown in Figure 4. 37. It is clear that path delay ranging from -420 ps to 600 ps with step as small as 10 ps is achieved. With antenna spacing of 18cm, this corresponds to scanning range of from -45° to 90° and scanning resolution of 1°. Although we try to match closely the four beamforming paths with careful chip and PCB layout, path mismatches which gives rise to delay offset between the paths are still observed. This is due to other factors such as die position variation within the package, bonding wires variation and etc, which are beyond our control. From the measurement done across 10 chips, 4 chips attain delay offset of less than 10ps as illustrated in Figure 4.38. These chips generate good beamforming patterns. To further minimize the delay offset and increase the yield, additional

independently tunable delay can be introduced along each path in the future.
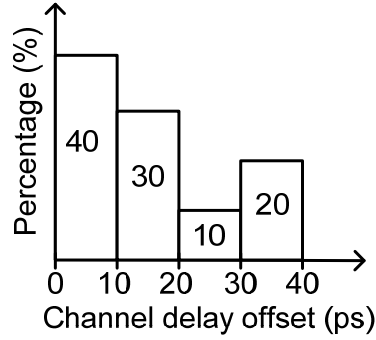
Figure 4.38. Distribution of maximal channel delay offset (ps).

Due to the I/O pin constraints, we cannot characterize the digital controlled delay cells and $\Delta\Sigma$ DLL individually. The default control setting, calibration, and calibrated control are all done through the FSM. To cover phase range from -45° to 90° in 1° step, only 91 delay control setting covering 0° to 90° is needed. -45°-0° can be easily obtained by swapping control setting for T_1 and T_2 corresponding to 0°-45°.

The measurement results of different chips for delay calibration for UWB center frequency are shown in Figure 4.39. The different chips' beamforming delay calibration circuit performance is shown in Figure 4.40.
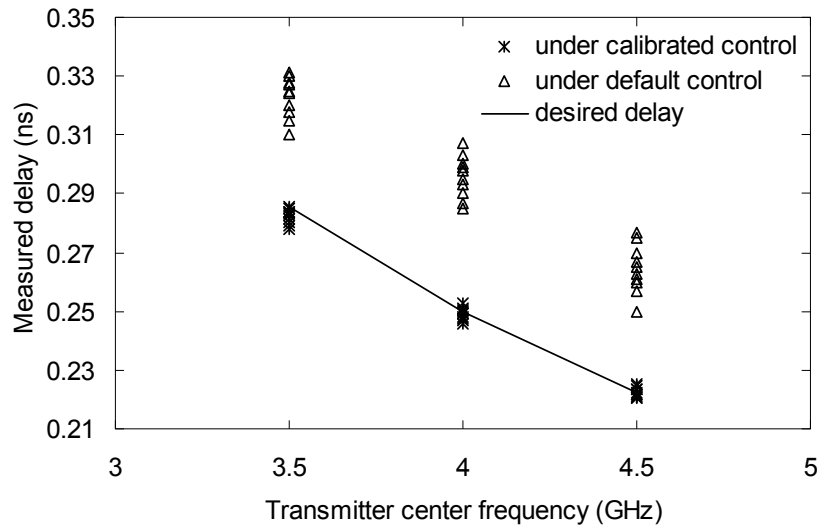
Figure 4.39. The delay calibration circuit performance of different chips for UWB center frequency
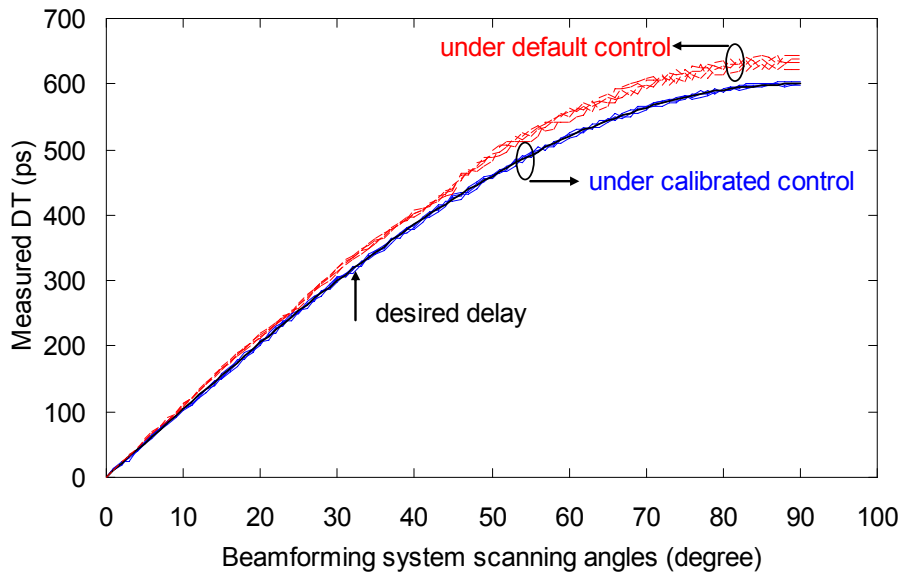
Figure 4.40. The delay calibration circuit performance of different chips for Beamforming delay.

Under default delay setting, the delay corresponds to the three frequency settings is off by 27% in the worst case in Figure 4.39. After calibration, accurate delay down to 3.5% (worst case) is observed. Due to the limited

number of I/O pads, the calibrated delay cannot be measured directly. However, by comparing the achievable beamforming path delay between default settings and calibrated settings, its functioning can be verified as shown in Figure 4.40.

The functioning of PSDC is also verified. PSDC could detect the ratio of UWB pulse peak to the lower frequency band energy. We first send a stream of different waveform control words from the FPGA, then we count the number of the comparator output "low". The tunable factor in this testing is the lower frequency band energy. To detect higher ratio than our desired 34 dB, proper gain at the lower frequency energy detector has to be set. Because this gain is mainly determined by the bias of the integrator, with relatively larger bias at the integrator in lower band energy detector to allow only a few UWB pulses to turn the comparator output down.

The functioning of PSDC is shown in Figure 4.41. When the ratio is less than 34 dB, the resulting spectrum violates the FCC mask and the comparator output is high. The comparator output only returns to low when the ratio exceeds 34 dB, which indicates a good UWB spectrum.

The measured PSD centered at 3.5, 4 and 4.5 GHz is also shown in Figure 4.42. The widening of spectrum at higher frequency is due to the narrowing of the overall UWB pulse width. If the center frequency is 3.5 GHz, the pulse width is 5 times 1/3.5 (ns), because there are five up and five down pulses. When the center frequency becomes 4.5 GHz, the pulse width becomes 5 times 1/4.5 (ns). Without scrambling circuits, there are many spikes on the spectral.
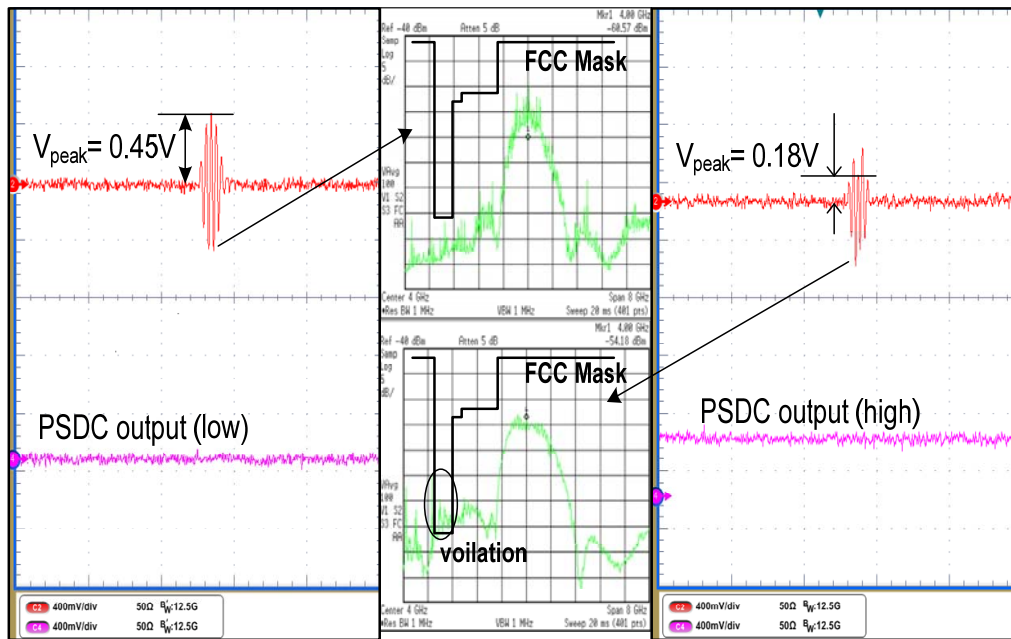
Figure 4.41. PSDC circuit performance.
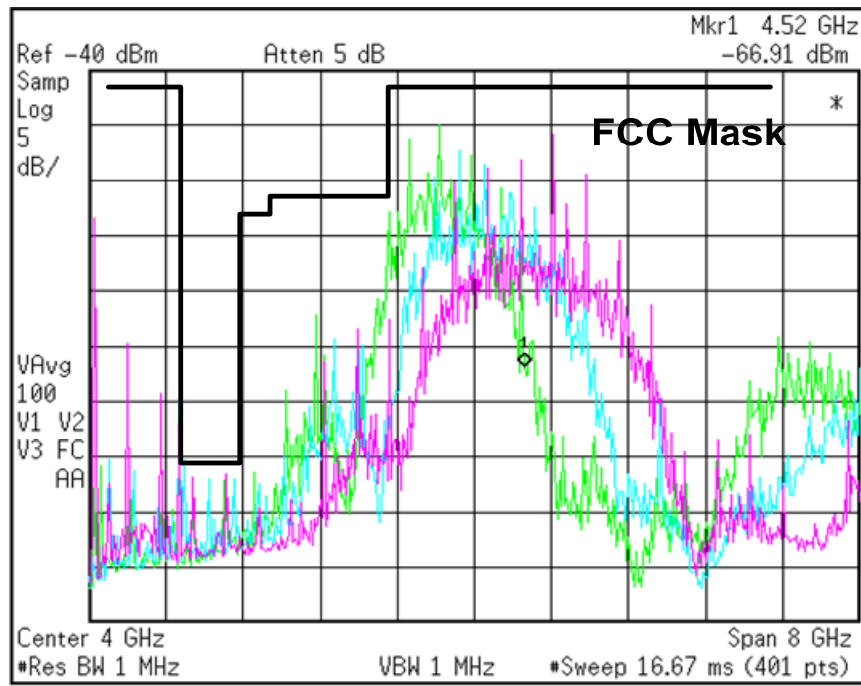
Figure 4.42. Measured PSD at three UWB center frequency bands of 3.5, 4
and 4.5 GHz.

The measured radiation patterns with 18 cm and 30 cm antenna spacing are shown in Figure 4.43-4.51.

(a)

(b)
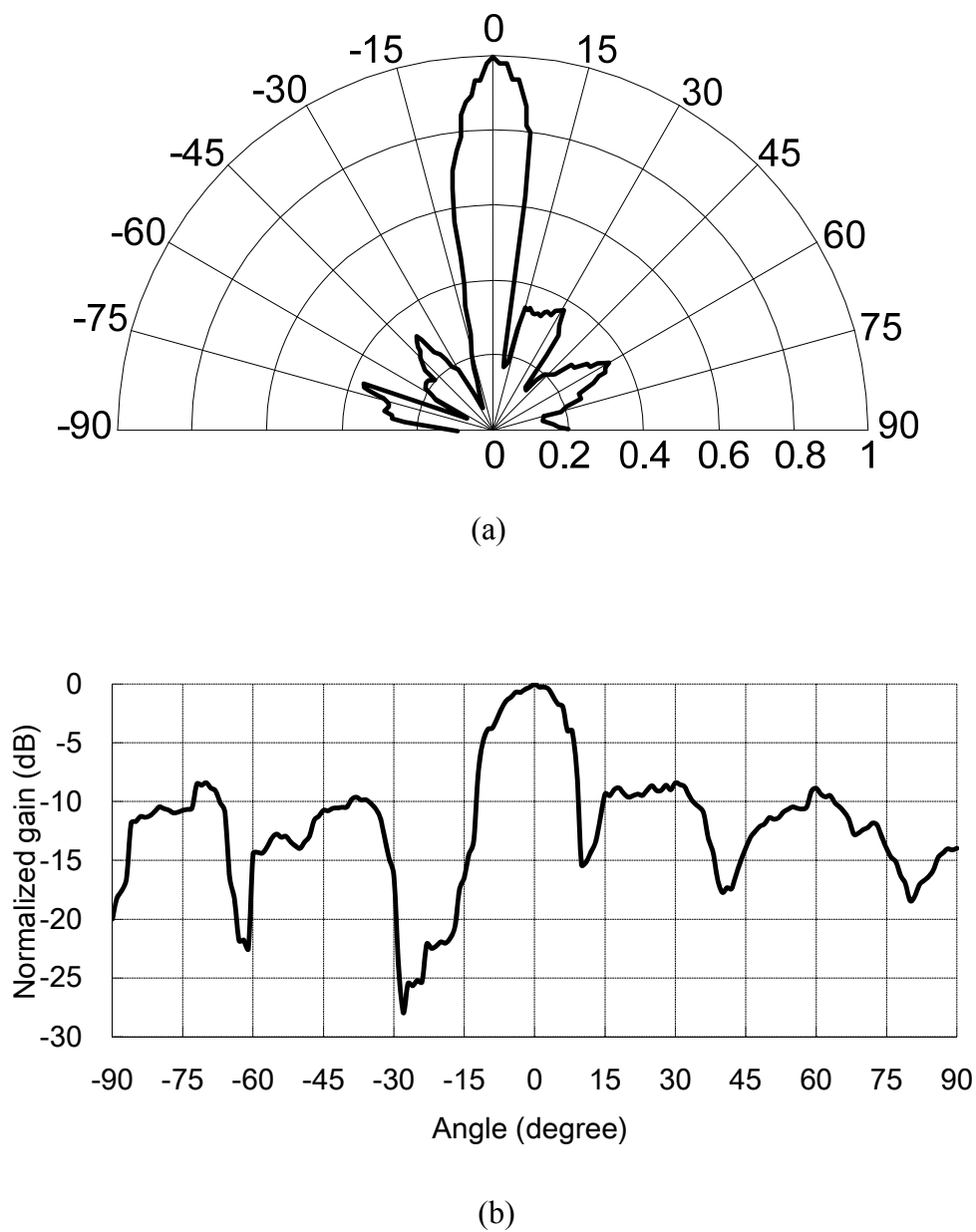
Figure 4.43. (a) Measured radiation pattern 0° @ 18cm antenna spacing; (b) Measured radiation pattern 0° @ 18cm antenna spacing in dB scale.
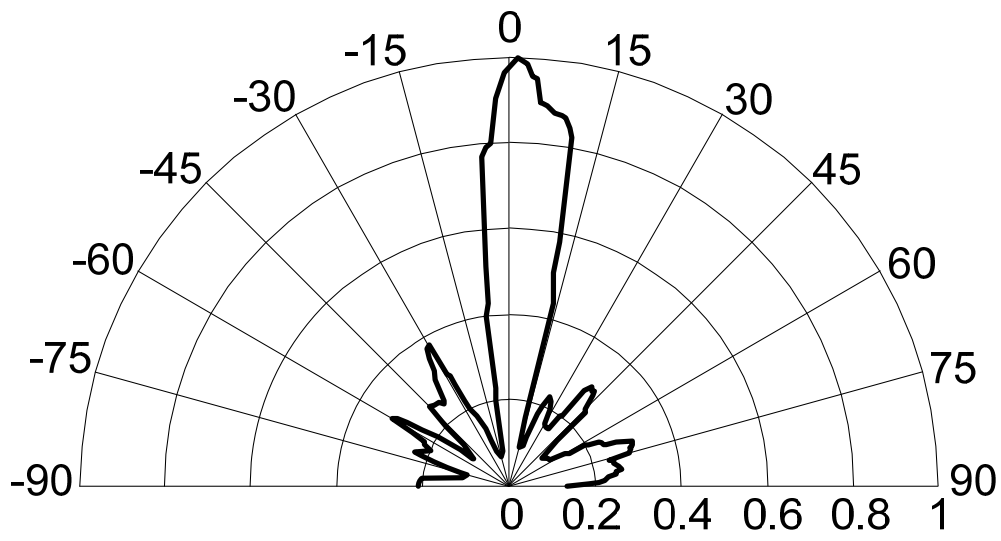
(a)
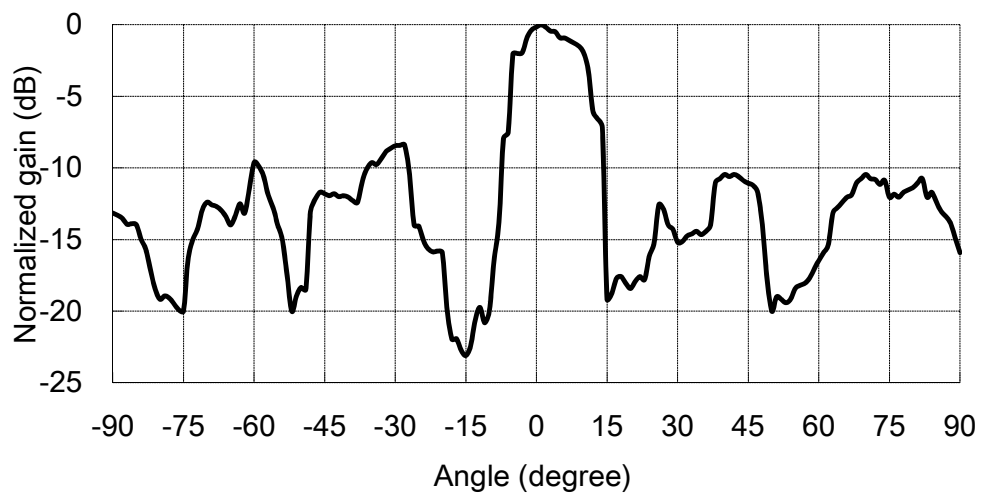
(b)

Figure 4.44. (a) Measured radiation pattern 1° @ 18cm antenna spacing; (b) Measured radiation pattern 1° @ 18cm antenna spacing in dB scale.
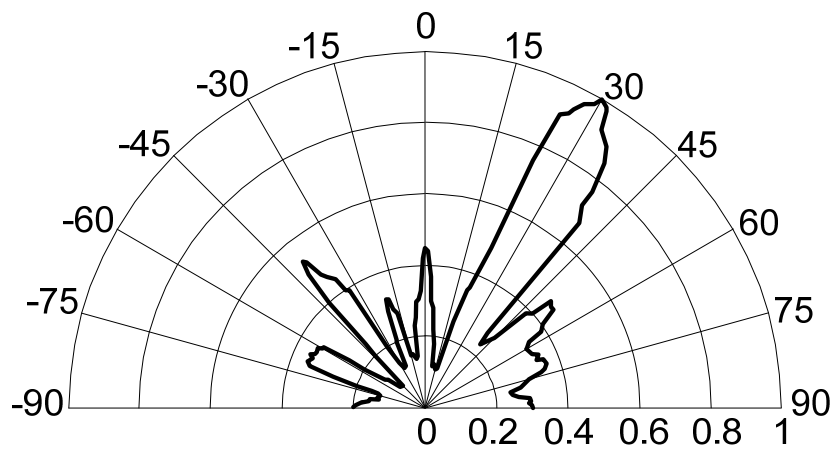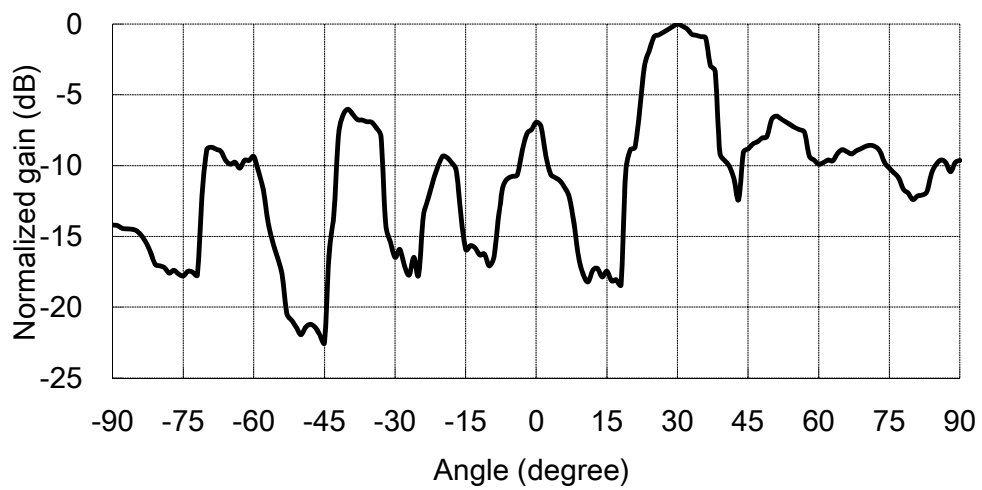
Figure 4.45. (a) Measured radiation pattern 30° @ 18cm antenna spacing; (b) Measured radiation pattern 30° @ 18cm antenna spacing in dB scale.
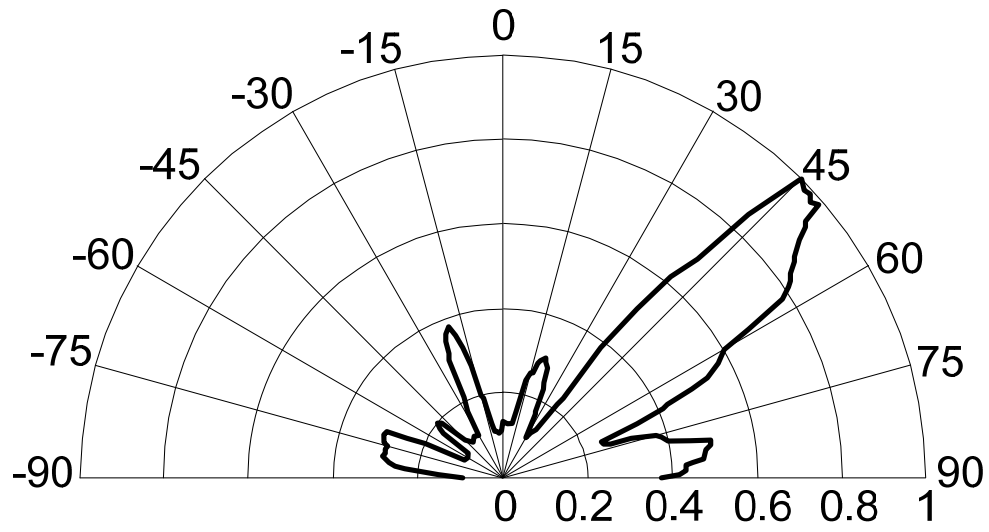
(a)
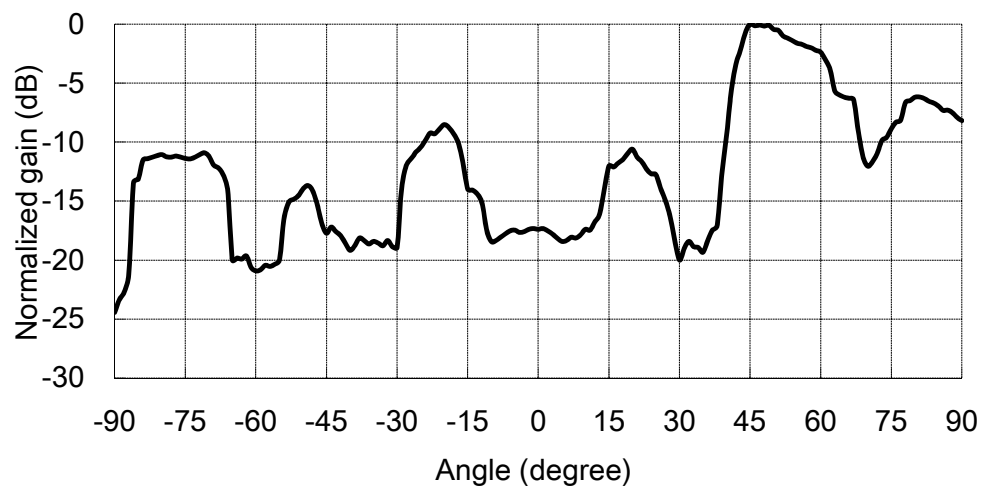
(b)

Figure 4.46. (a) Measured radiation pattern 45° @ 18cm antenna spacing; (b) Measured radiation pattern 45° @ 18cm antenna spacing in dB scale.
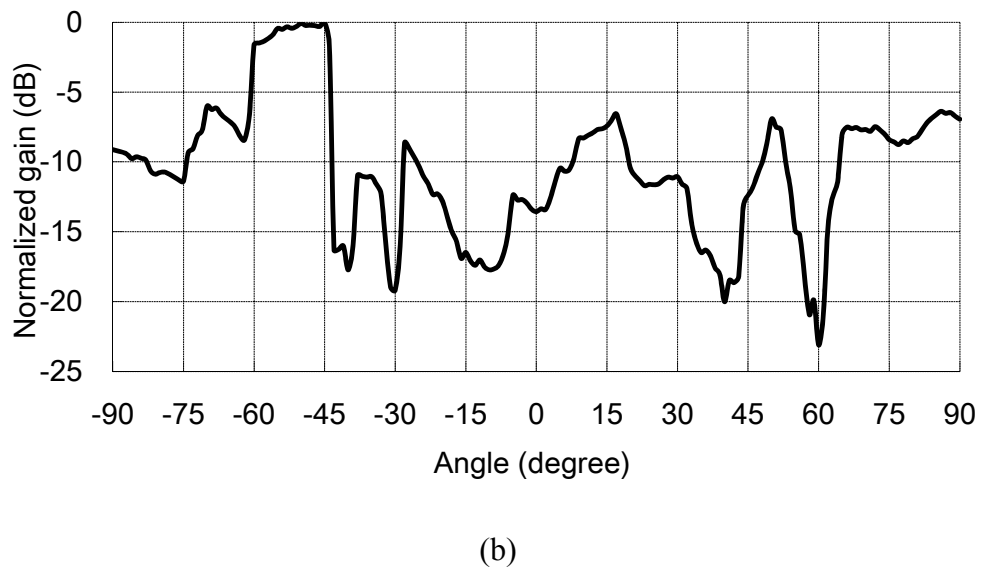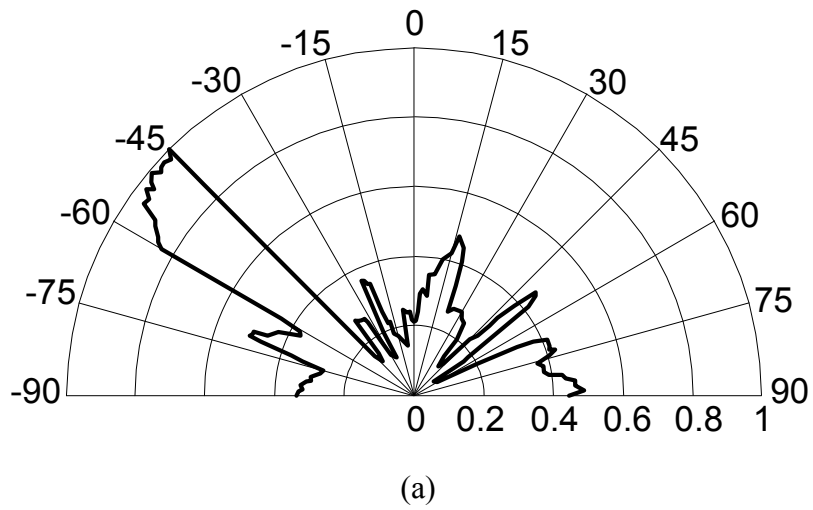
Figure 4.47. (a) Measured radiation pattern -45° @ 18cm antenna spacing; (b) Measured radiation pattern -45° @ 18cm antenna spacing in dB scale.
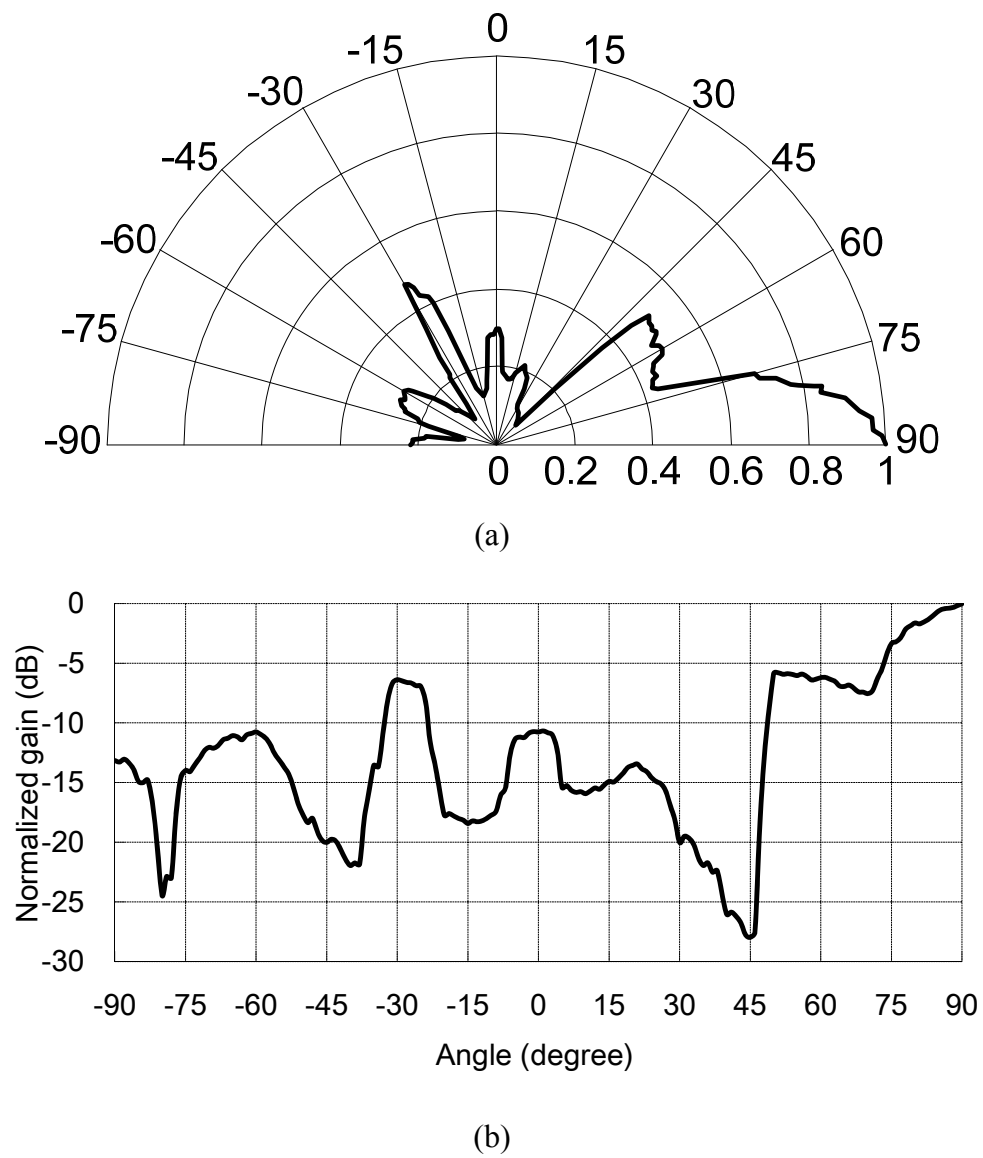
Figure 4.48. (a) Measured radiation pattern 90° @ 18cm antenna spacing; (b) Measured radiation pattern 90° @ 18cm antenna spacing in dB scale.
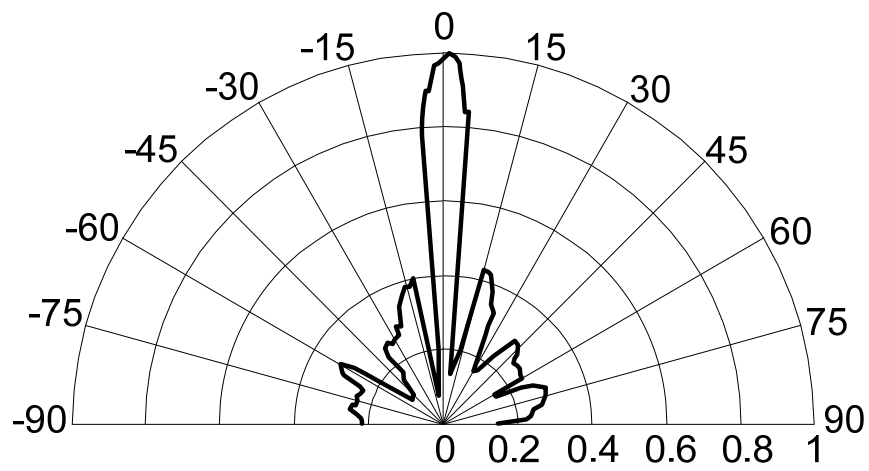
(a)
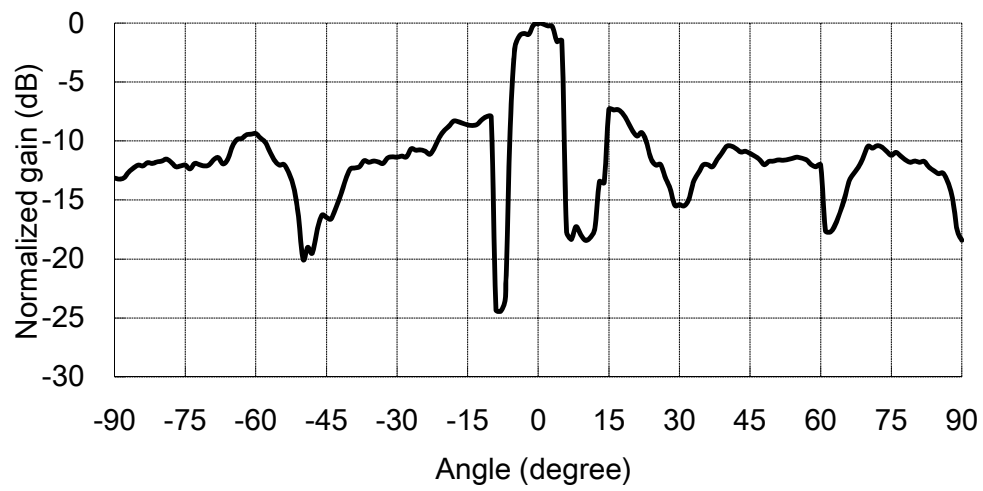
(b)

Figure 4.49. (a) Measured radiation pattern 0.4° @ 30cm antenna spacing; (b) Measured radiation pattern 0.4° @ 30cm antenna spacing in dB scale.
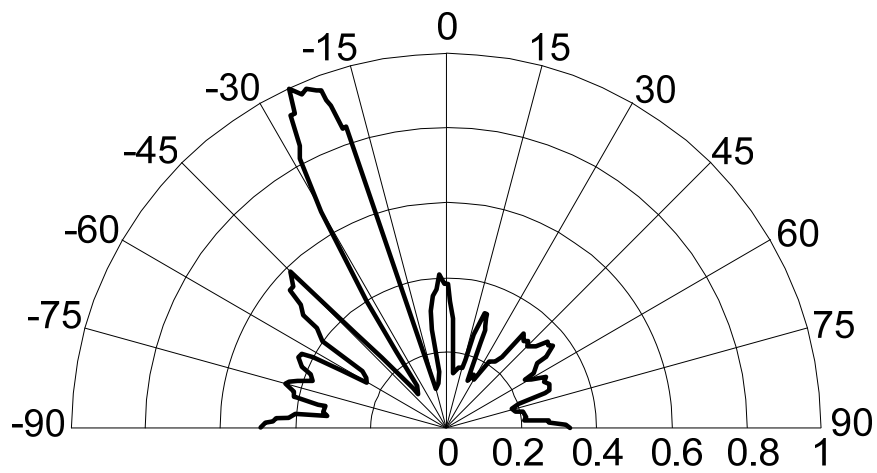
(a)
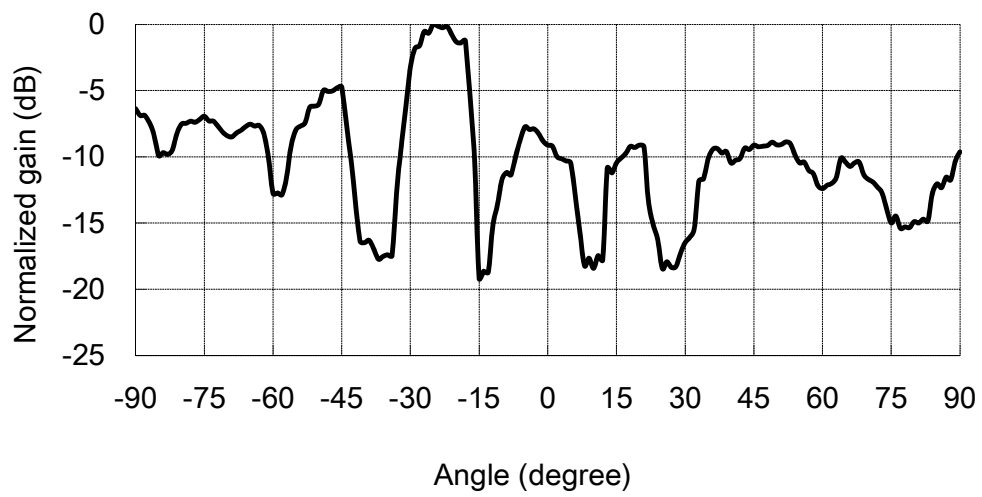
(b)

Figure 4.50. (a) Measured radiation pattern -25° @ 30cm antenna spacing; (b) Measured radiation pattern -25° @ 30cm antenna spacing in dB scale.

(a)

Angle (degree)

(b)
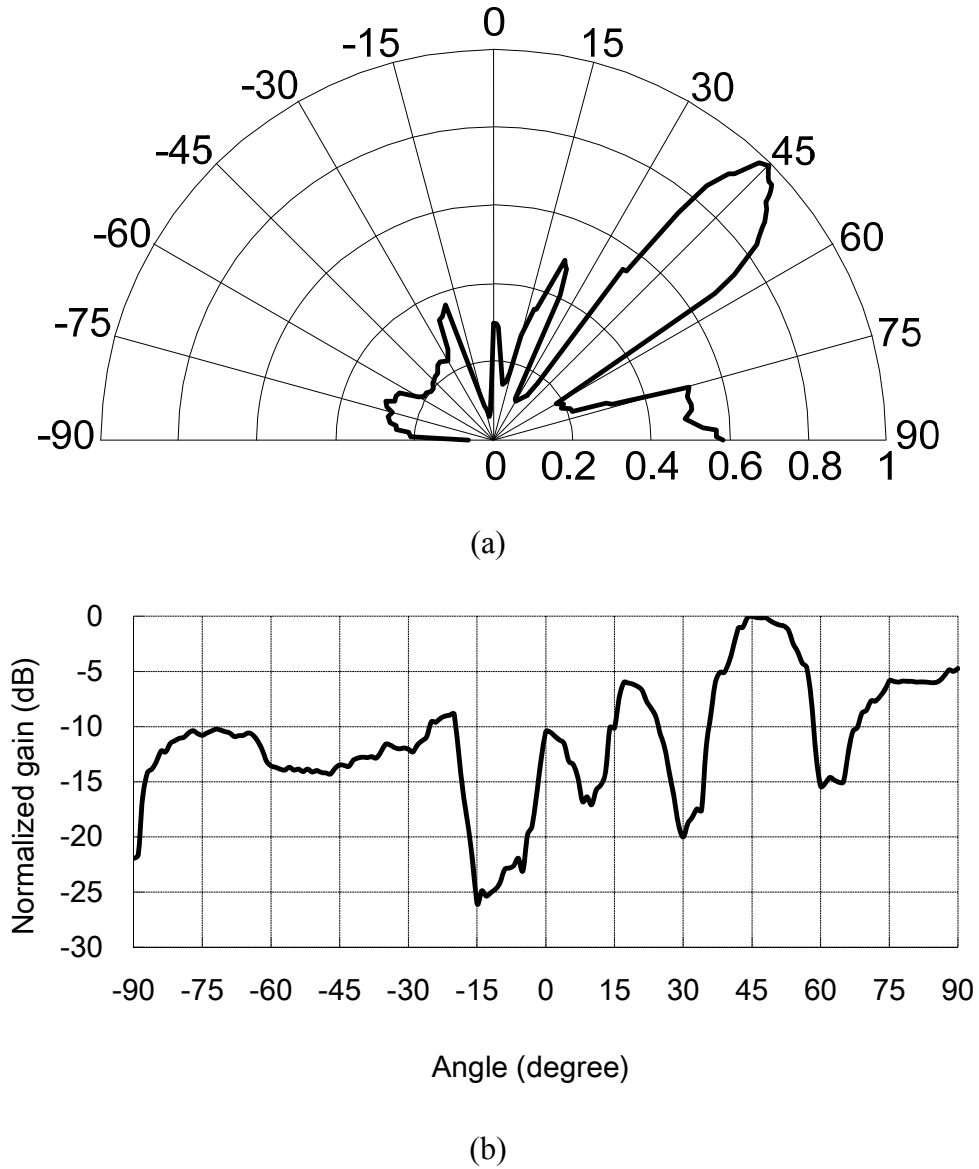
Figure 4.51. (a) Measured radiation pattern 45° @ 30cm antenna spacing; (b) Measured radiation pattern 45° @ 30cm antenna spacing in dB scale.

The antenna spacing is chosen to be the same as [23] and [50] to facilitate comparison. It is clear that the scanning range covers from -45°-90° at scanning resolution of 1° with 18 cm antenna spacing. The scanning range reduces to -25°-45° with 30 cm antenna spacing. However, the scanning resolution improves to 0.4°. As pointed out in [11], the side lobes in the radiation patterns could be tuned by shaping the signal waveform in time

domain. Figure 4.44 and 4.49 shows the rectangular plot of radiation pattern in dB scale for 1° (d=18 cm) and 0.4^o (d=30 cm), exhibiting a -3 dB bandwidth of 20° and 13°, respectively.

The proposed UWB beamforming transmitter is compared to other reported works and the results are summarized in Table 4.1 (a). With the proposed vernier delay chain and $\Delta\Sigma$ DLL calibration, we achieve similar if not wider scanning range coverage as well as an order of magnitude improvement in scanning resolution. In addition, due to the full digital architecture, the proposed beamforming transmitter only consumes 8 mA under 1.2 V supply which is at least about 10 times lower than those reported ones. The power consumption in Table 4.1 (a) corresponds to the data rate of 80 Mbps. It has a static power consumption of 5.9 mW and a portion that scaled with data rate at rate of 46 pJ/pulse, as shown in Figure 4.52. Note that the reported power in [23] with only the beamforming path delay subsystem is consuming around 100 mW.
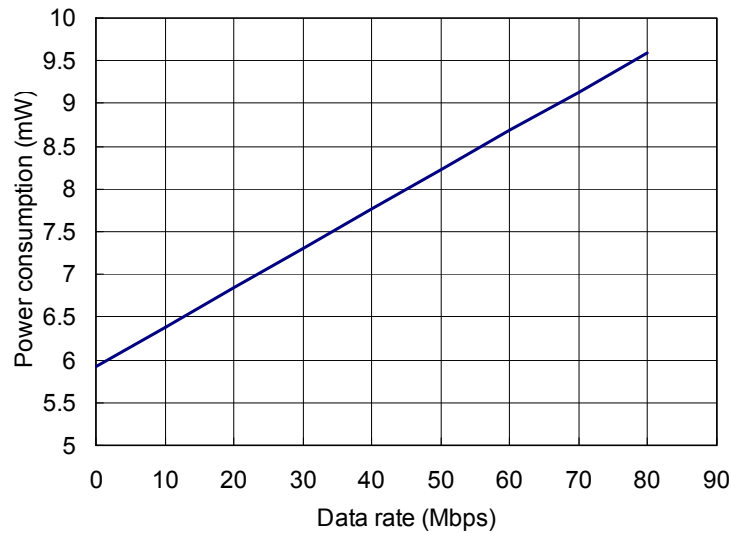
Figure 4.52. The beamforming transmitter power consumption at different data rate.

Table 4.1 (a) UWB beamformer performance comparison; (b) UWB transmitter performance comparison.

(a)

UWB beamformers performance comparison				
Reference	Z. Safarian, RFIC, Jun. 2008	M. Y. Chia, MTT, Jun. 2006	This work	
Technology	0.13μm	0.25μm	0.13μm	
No. of Channels	4	11	4	
Operation Frequency (GHz)	0~6	3~10	3~5	
Maximum Delay (ps)	880	500	700	
Delay Step (ps)	180	100	**10**	
Phase Resolution	10°	9°	**0.4°**	**1°**
Phase Range	-60°~60°	9°~59°	-25°~45°	**-45°~90°**
Antenna Spacing(cm)	30	18	30	18
Operating Power (mW)	-	100	**9.6**	

(b)

UWB transmitters performance comparison						
Reference	Y. Zheng, ISSCC, Feb. 2010	P.P. Mercier, JSSC, Jun. 2009		S.Soldà, JSSC, Jun. 2011	Y. Park, JSSC, May 2011	This work
Technology	0.18μm	90nm		0.13μm	65nm	0.13μm
Supply (V)	1.8	1		1.35	0.9	1.2
Standby power (μW)	-	123		-	170	**7.2**
Operation Frequency (GHz)	3~5	2.1~5.7		7.25~8.5	3.1~5	3~5
Data Rate (Mbps)	1	1.6[1]	249.6[1]	5	50	10~80
E_{dTX} (pJ/pulse)	920	103	17.5	186	12	**10**
E_{pTX} (pJ)	23	2	0.1	13.2	0.1	1.5
θ_{TX} (%)	2.5	2	0.6	7	0.83	**7.5[2]**

1 Every symbol contains 16-pulse-burst
2 A factor of 0.5 is introduced to account for 50% OOK modulation in our TX

Individual transmitter performance is also compared with other reported state-of-the-art in Table 4.1 (b). We use Agilent 8133A signal generator to provide both data clock and pseudo random data pattern.

Although energy per pulse (E_{dTX}) is a popular measure for UWB transmitter performance, it could be misleading if the antenna pulse energy (E_{pTX}) is not considered. This is because significantly higher power will be consumed to generate higher E_{pTX} due to larger buffer driving strength, which in turns worsens the power efficiency due to loading. For fair comparison, [14] proposed to combine E_{dTX} and E_{pTX} to form efficiency (θ_{TX}). From the table, although we did not report the highest E_{pTX}, we attain the best E_{dTX} and θ_{TX} due to the proposed locally edge combined pulse generation technique. We would also like to point out that this is achieved even with poorer technology node at 0.13 μm.

CHAPTER 5 0.1-10 GHZ UWB BEAMFORMING RECEIVER

5.1 Introduction
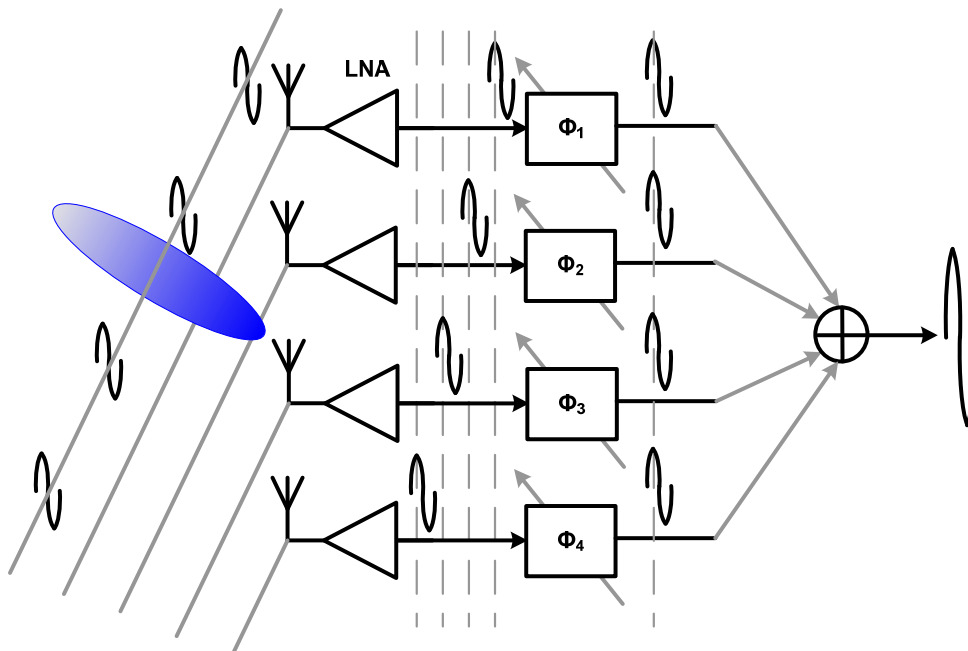
Figure 5.1. Beamforming receiver principle illustration.

IR UWB beamforming system is attractive for radar and imaging application. The IR UWB beamforming transmitter is presented in Chapter 4, while this chapter will show an IR UWB beamforming receiver. As illustrated in Figure 5.1, the signals in the air along a particular direction can add up coherently in a beamforming receiver system, and lead to beamsteering in that direction. Imaging radar could be realized based on the received signal direction and strength. This also enables directional communication and minimizes the

interference to and from other narrow band systems [8]. As mentioned, UWB beamforming receiver also provides an additional degree of freedom in choosing the antenna spacing [7] and achieves higher depth resolution and range resolution at the same time [11].

Like beamforming transmitters, beamforming receiver can also be classified into IF, RF and LO phase shift architectures [10] [24] depending on the phase shifter location. However, LO phase shift receiver is only suitable for narrow band system. UWB beamforming receiver will suffer from large area and power penalty if IF phase shift receiver architecture is adopted, because the later path combination implies duplication of many blocks from LNA down to baseband. Therefore, only RF phase shift architecture is suitable for UWB beamforming receiver. Depending on phase shifter implementation, UWB beamforming receiver could be further categorized into passive [7], [11], [25] or active [26] phase shifter based architectures.

Active phase shifter based architectures needs active inductor to provide wide band phase shift. However, active inductor consumes large power and is difficult to operate for frequency higher than 3 GHz [26]. Therefore, passive LC delay element is favored to provide wide band phase shift [7], [11], [25]. Path sharing beamforming receiver was proposed in [7], [11], [25], as shown in Figure 5.2. The main advantage of the path-sharing receiver architecture is the reduction of the maximum required delay for each variable true time delay element. It reduces the total required delay by 3 times for 4-channel beamformer, and therefore is able to lead to a significant reduction in chip area. However, to simplify the path sharing, only one unit delay element is used, which result in phase resolution of only 9º. In addition, high Q inductor and additional intermediate buffers are needed to minimize the cascade losses. Therefore, there is a trade-off between area and power consumption for active

and passive phase shifters.
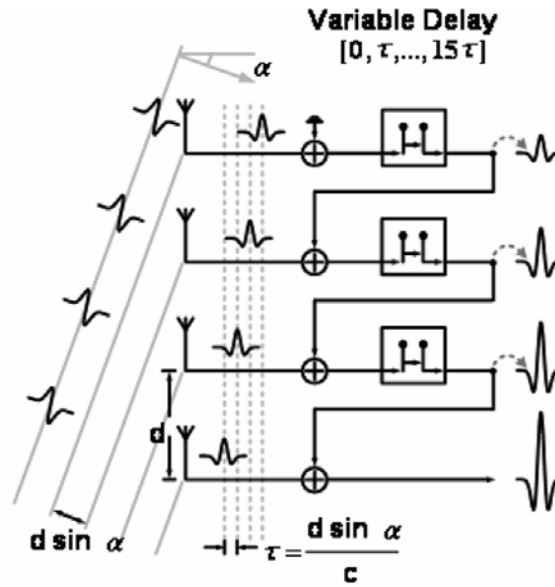
Figure 5.2. Path sharing beamforming receiver architecture [7], [11], [25].
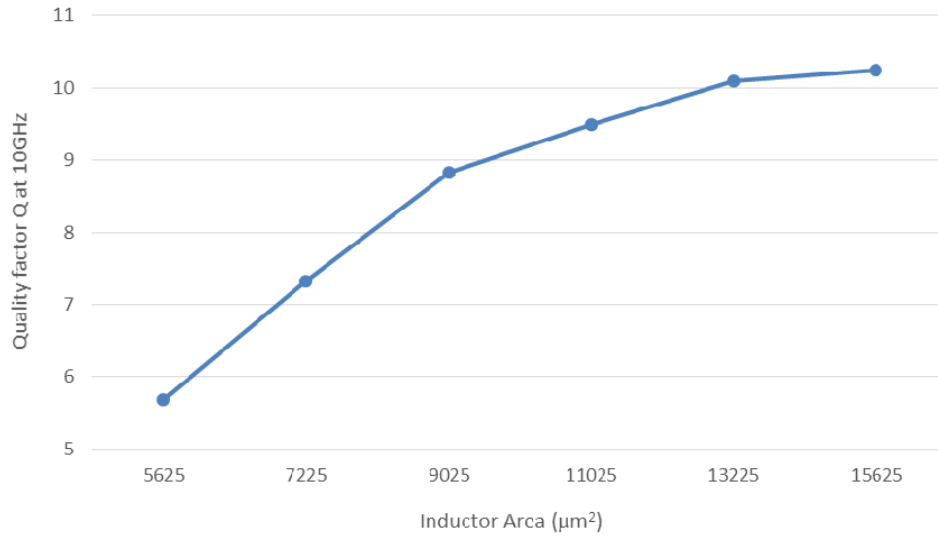
Figure 5.3. The relationship between inductor Q and area.

To achieve finer delay resolution, smaller unit delay is needed. Coupled with

the high-Q requirement, this often results in excessive area for multi-channel beamforming receiver design even with path sharing. As shown in Fig. 5.3, to improve the inductor Q by 2 times would require about 3 times larger area. This prompts us to relook at the phase shifter design and rethink about trade-off between high Q and insertion loss. In this implementation, we adopt Q compensation through current reuse buffer. This allows us to have lower Q inductor without significant insertion loss and power penalty. Eventually, this will lead to very area efficient UWB beamforming receiver architecture.

5.2 System Architecture
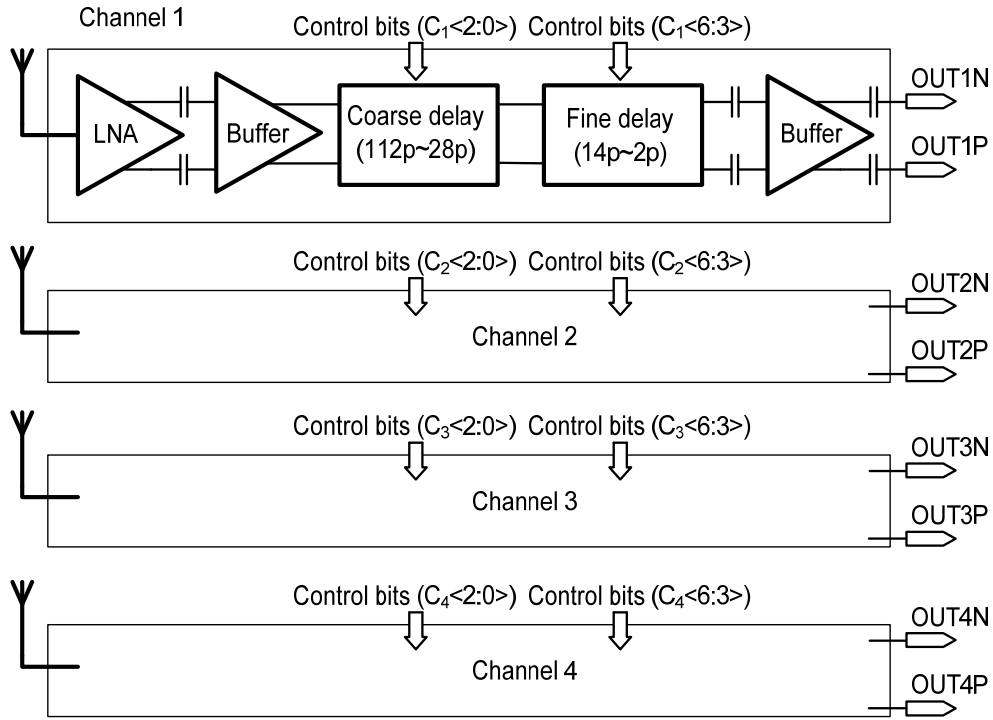
Figure 5.4. The proposed 4-channel UWB beamforming receiver architecture.

The proposed 4-channel UWB beamforming receiver is shown in Figure 5.4.

Along each path, after signal amplification by LNA, the signal will experience different delay determined by the programmable phase shifter. To avoid excessive power penalty, path sharing is not adopted to eliminate intermediate buffers. In addition, 3-bit coarse delay element coupled with 4-bit fine delay element is adopted to achieve fine delay resolution without the need of excessive inductors. The 3-bit coarse delay element will generate delay from 0 ps-196 ps in step of 28 ps. Whereas the 4-bit fine delay element will generate delay from 0-30 ps in step of 2 ps. In combination, the phase shifter can provide delay ranging from 0 ps - 225 ps in step of 2 ps. The achieved delay resolution is 7 times better than [7], [11], [25].

Although the amount of inductor has been cut down significantly, the area is still excessive for multi-channel implementation. From our investigation, we found that the inductor Q does not affect delay significantly but only incur higher insertion loss. In this implementation, we thus adopt inductor with lower Q to achieve the desired delay. To compensate for the loss, two additional buffers are inserted at the beginning and end of the phase shifter. Current reuse structure is adopted to maximize the gain without too much power penalty. This results in both an area and power efficient UWB beamforming receiver architecture. The circuit implementation details will be discussed next.

5.3 Circuit Implementation

5.3.1.   Noise Canceling and Current Reuse LNA
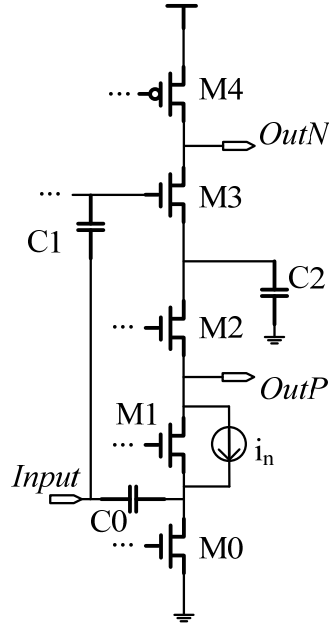
Figure 5.5. The proposed noise canceling and current reuse LNA (biasing not shown).

The inductor-less LNA circuit is shown in Figure 5.5. To have a maximal power transfer, the input impedance Z_{in} is designed to match to the source impedance, R_s. This LNA includes a common gate stage containing M0, M1 and M2 and a common source stage consisting of M3 and M4. C2 is a large bypassing capacitor to create an AC ground. Large power has to be consumed by LNA to lower the noise and enlarge the bandwidth. Considering this trade-off, noise canceling with current reuse structure is proposed. Active balun is needed as the input is preferably single-ended to minimize the IO needed for multi-channel implementation. Therefore, the proposed current reuse LNA incorporates both noise cancellation and active balun functions. On the other hand, differential processing is generally preferred, especially for LC phase shifter, which could introduce undesirable ringing effect. The resulting gain is given by

$$A_{CG} = R_{OutP}/R_s. \tag{5.1}$$

The differential gain is larger than 15 dB while the 3 dB bandwidth is more than 10 GHz, as shown in Figure 5.6.
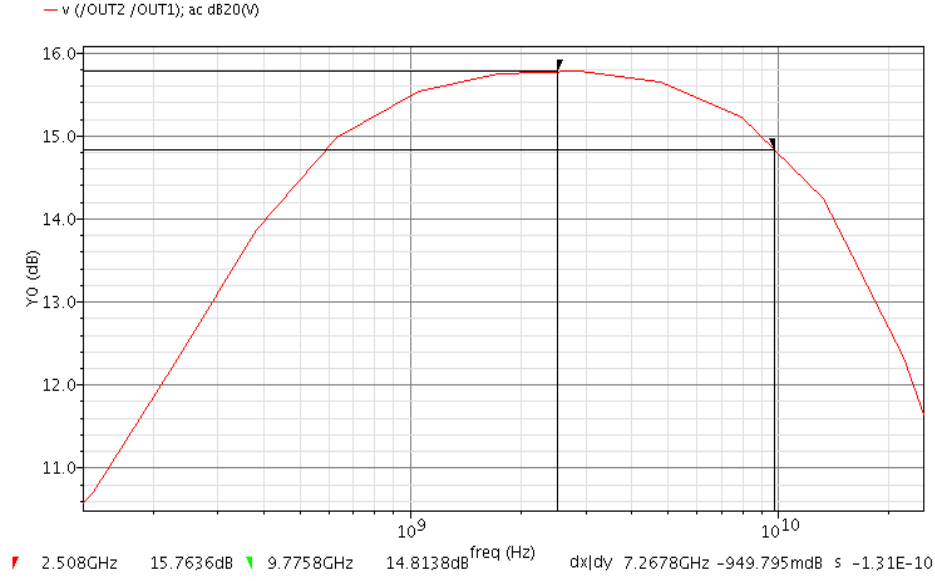
Figure 5.6. The frequency response of the proposed LNA.

Similar noise-cancelling concept [51-56] is adopted for this LNA. The noise generated by the input matching transistor M1 can be represented by a current source i_n, as shown in Figure 5.5. It generates noise voltage at common gate stage output

$$V_{n,OutP}=i_n R_{OutP}, \tag{5.2}$$

where R_{OutP} is the impedance at node $OutP$. M1 noise voltage at common source stage output is

$$V_{n,OutN}=R_s i_n A_{CS}. \tag{5.3}$$

$V_{n,OutP}$ is equal to $V_{n,OutN}$ under the condition of Equation (5.1). For differential output, this noise component will then be cancelled. Therefore, the input matching, balanced output and noise cancelling could be achieved at the same time. The simulated S_{11} is smaller than -8 dB in the 0.1-10 GHz range, as shown in dashed line in Figure 5.7. It achieves 4.6-5.1 dB noise figure in simulation as shown in Figure 5.8.
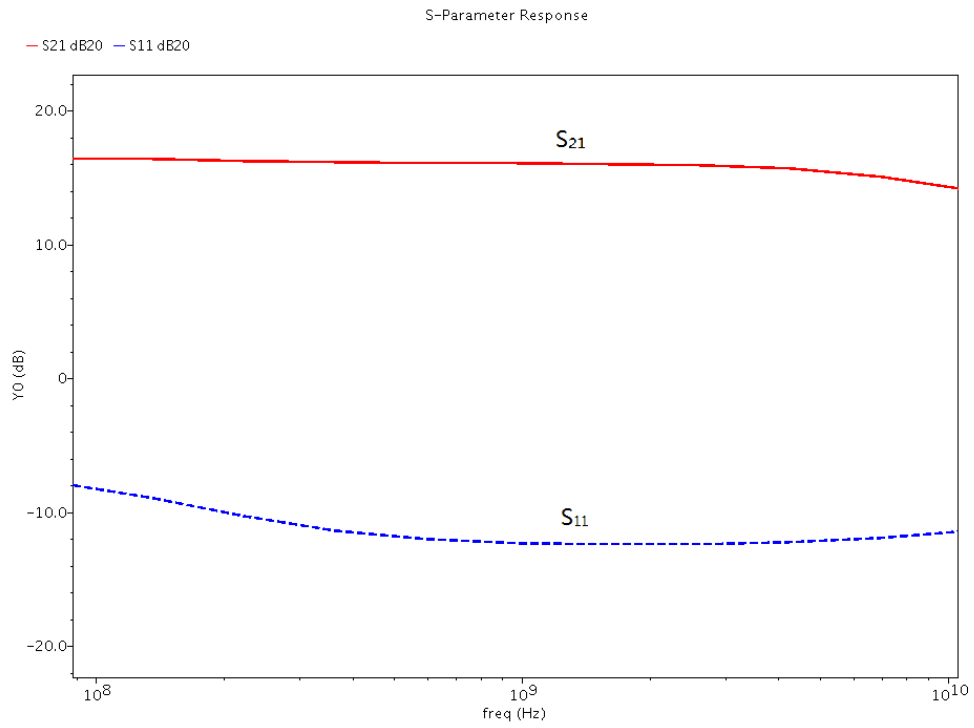
Figure 5.7. The simulated S_{11} and S_{21} of the proposed LNA.
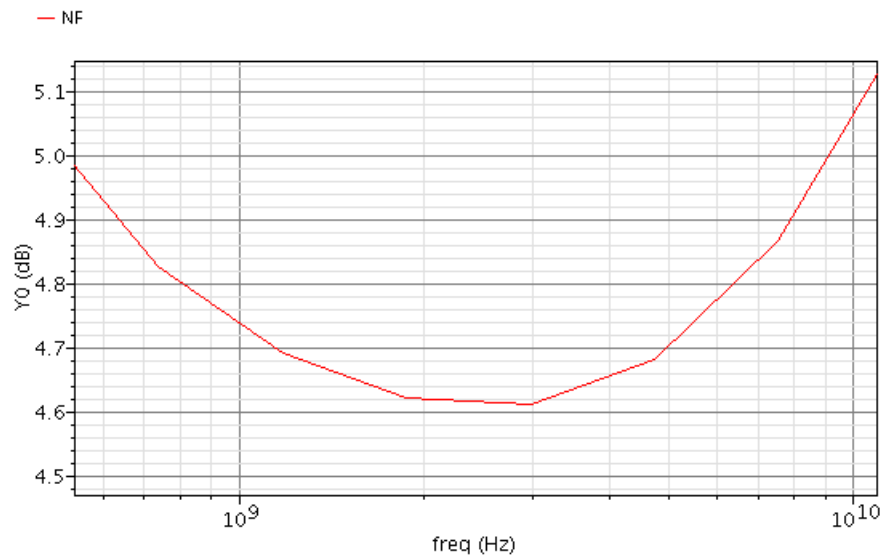
Figure 5.8. The simulated noise performance of the proposed LNA.

This LNA consumes small current of 5.4 mA under 1.5 V supply thanks to the current reuse structure. However, there might be concerns about its nonlinearity due to small voltage headroom caused by transistors stack. To study this issue, both IIP3 and P1dB are simulated. As shown in Figure 5.9, the P1dB is about -5 dBm, and the IIP3 is around 1 dBm. Both are large enough for our system.
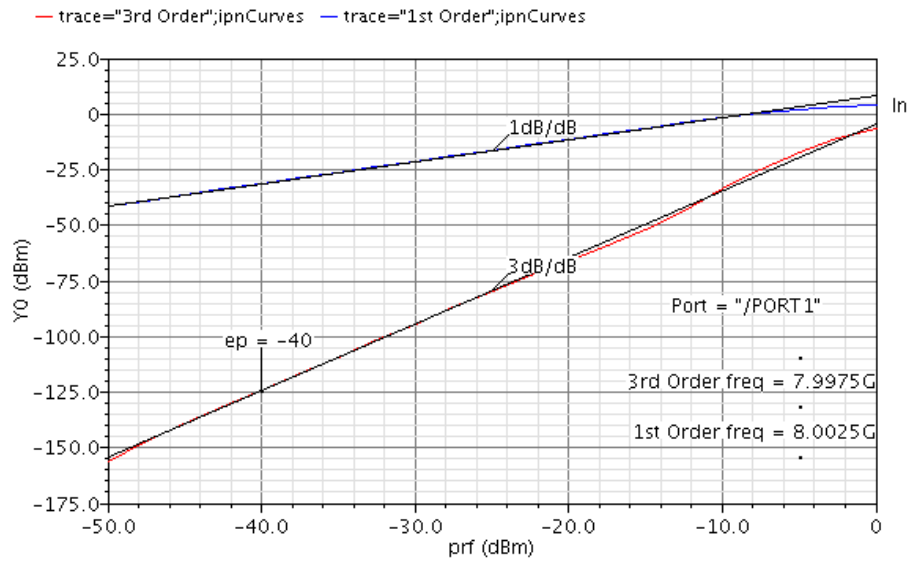
Figure 5.9. The IIP3 and P1dB simulation of the proposed LNA.

Table 5.1   LNA performance summary and comparison with others

	Technology (nm)	BW (GHz)	Gain (dB)	NF (dB)	IIP3 (dBm)	Power (mW)	FOM (dB)
[53]	65	1-11	10.5	2.7-3.3	-3.5	13.7	2.05
[51]	250	0 -1.6	10-14	1.9-2.4	0	35	-7.59
[54]	65	0.2-5.2	13-15.6	3-3.5	0	21	3.1
[55]	130	0.2-3.8	19	2.8-3.4	-4.2	5.7	7.47
[56]	130	2-9.6	11	3.6-4.8	-7.2	19	-13.58
Ours	65	0.1-10	14.8-15.7	4.6-5.1	1	9.6	12.4

The LNA performance is summarized and compared with other wideband LNAs as shown in Table 5.1. The FOM in [57] is adopted.

$$FOM = 20\log_{10}\frac{IIP3[mW]\times Gain[lin]\times BW[GHz]}{Power[mW]\times(NF[lin]-1)} \tag{5.4}$$

Compared with others, our LNA has a high gain over a wide bandwidth. With current reuse technique, our LNA also achieves low power. Therefore, we obtain the best FOM.

5.3.2. True Time Delay Line
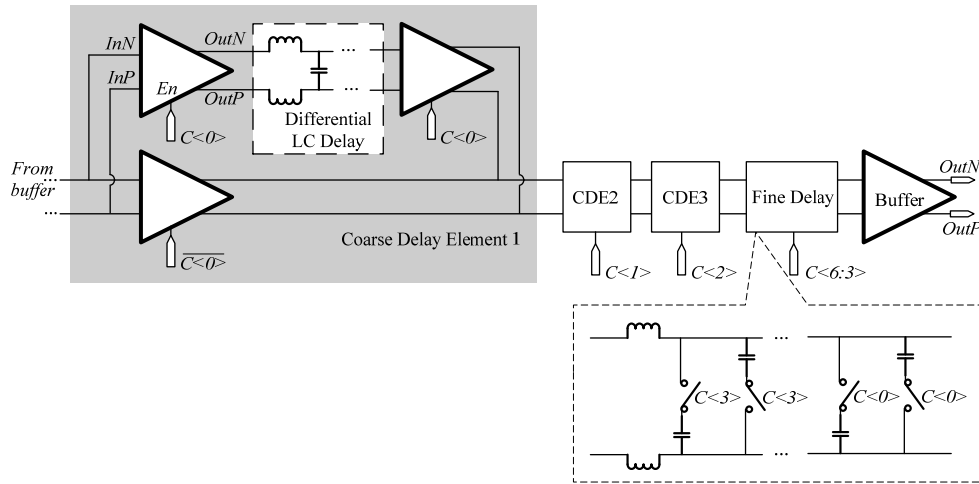
Figure 5.10. The true time delay line circuit.

The variable true-time-delay elements are crucial in each channel to compensate the propagation delay of the incoming signal. To better suppress common mode and supply noise, the fully differential true time delay line structure is adopted, as shown in Figure 5.10. To limit the array spatial scanning within a discrete number of directions, it is convenient and meaningful to realize variable time delay elements with discrete delay settings.

The desired settings for the delay are stored in on-chip shift registers that are programmed through serial peripheral interface. To increase the delay range, large area will be consumed. Considering the trade-off between area and delay range, 7-bit delay line is designed to cover 225 ps delay range in 2 ps delay step. The L-C delay cells are implemented as quasi-distributed differential transmission line. The generated delay is about

$$T_d = n\sqrt{LC},$$
(5.5)

where n is the number of LC sections. The impedance of the delay line is

$$Z_0 = \sqrt{L/C}.$$
(5.6)

The coarse delay element impedance is designed to be 100 Ω. The fine delay element impedance varies from 50 Ω to 400 Ω.
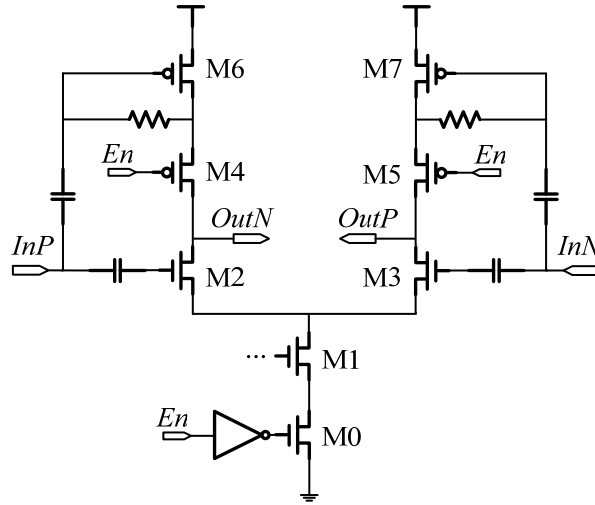
Figure 5.11. The path-select amplifier.

The fully differential path-select amplifier also adopts current reuse architecture as shown in Figure 5.11. Path-select amplifier is used to enable or disable the coarse delay element and compensate for the insertion loss due to the passive L-C delay cell. To minimize reflection, constant impedance could

be maintained by the path-select amplifier whether the coarse delay element is enabled or not.

5.4 Simulation Results
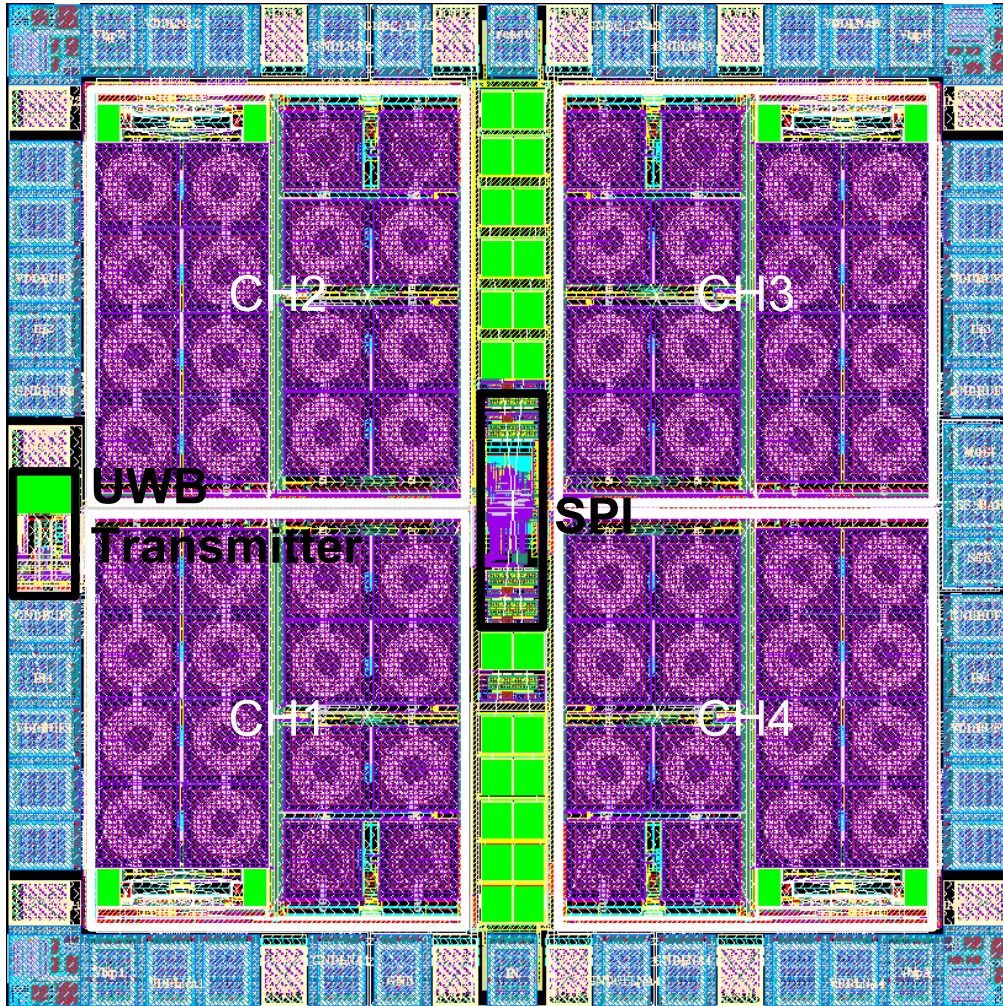
Figure 5.12. The floor plan of the proposed beamforming receiver circuit.

Implemented in 65 nm CMOS technology, the UWB beamforming receivers and a UWB transmitter system occupies total area of 1.44 mm^2 including IO pads as shown in Figure 5.12. Actually, it also includes a UWB transmitter

which has the same structure as the 3-5 GHz one in Chapter 4, so its circuits are not discussed here. The simulated UWB pulses and its spectrum are shown in Figure 5.13. Its center frequency is around 5 GHz. Its bandwidth is about 10 GHz. Due to the power efficient digital circuit and short pulse duration, it achieves energy efficiency of 2.5 pJ/pulse.
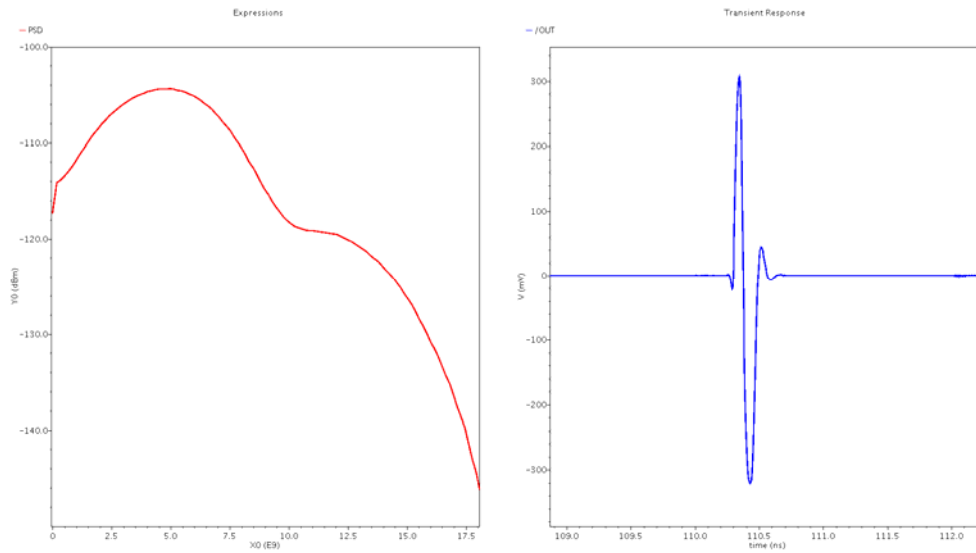
Figure 5.13. The simulated UWB pulse and its spectrum.

The whole beamforming receiver consumes 180 mA. The simulated four channel waveforms at different delay settings are shown in Figure 5.14. The delay difference could be varied from -75 ps to 75 ps with delay step of about 2 ps. If the antenna spacing is 3 cm, this time delay covers scanning angle from -48º to 48º with 1º resolution.

(a)

(b)

(c)
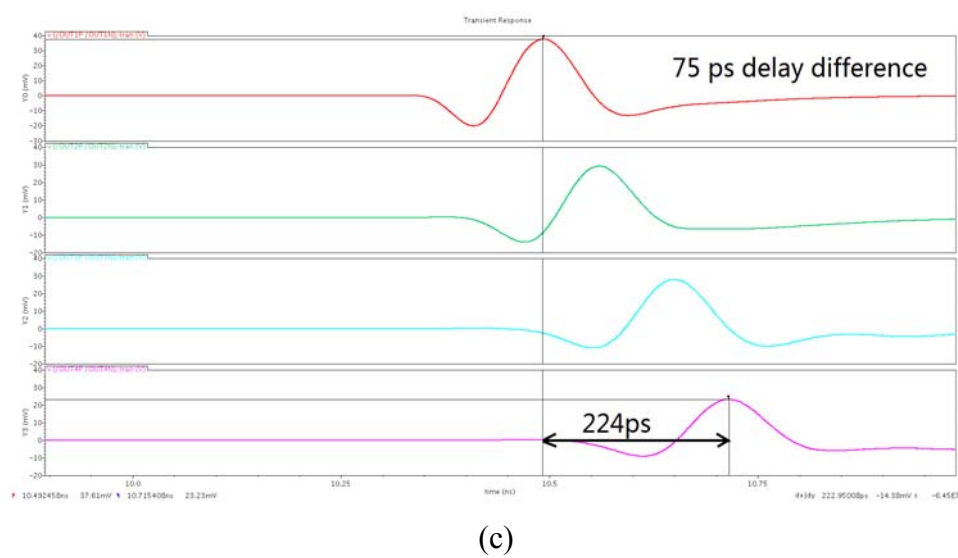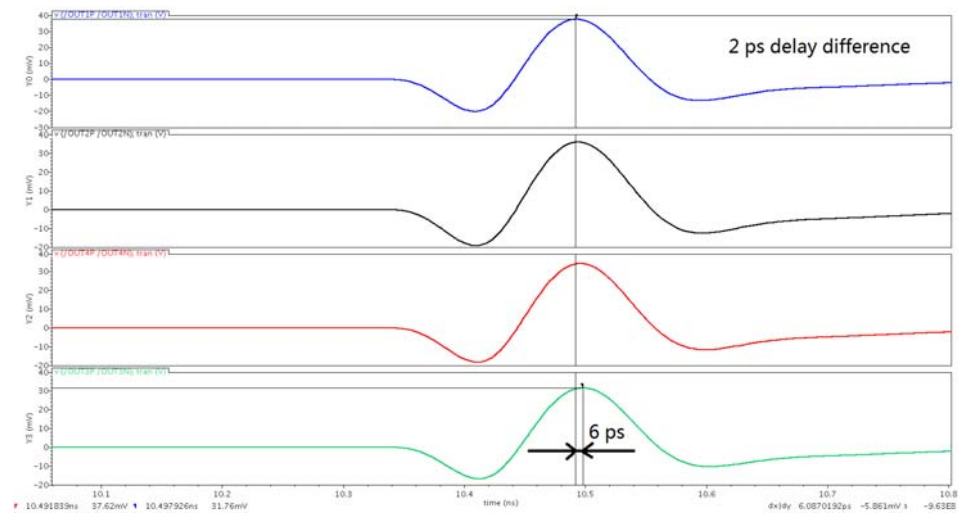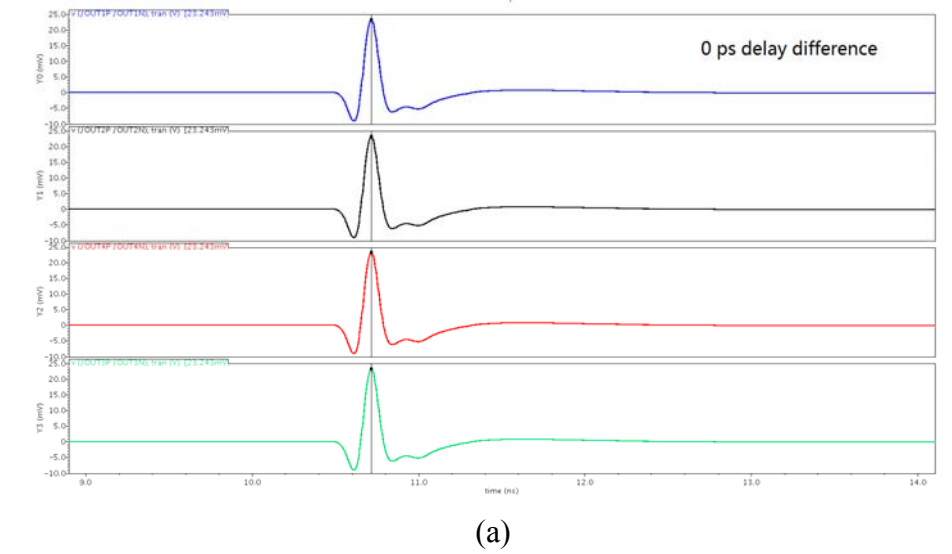
Figure 5.14. Adjacent channel delay difference: (a) 0 ps; (b) 2 ps; (c) 75 ps.

The performance is summarized and compared with other reported state-of-the-art in Table 5.2. This work adopts passive L-C based delay with Q compensation to allow compact implementation. It achieves much wider frequency range compared to active phase shifter architecture. Compared with other passive delay, this works achieves about 7 times smaller area. By minimizing number of intermediate buffers and path-select amplifiers, and employing current reuse technique to maximize the gain for a given power, we achieve the lowest power consumption.

Table 5.2   Beamforming receiver performance summary and comparison with others

Works	T.S. Chu, JSSC, Dec. 2007	S.K. Garakoui, ISSCC, Feb. 2012	This Work (Simulation)
Technology	130nm	140nm	65nm
Technique	L-C	G_m-C	L-C
RF front end performance per channel			
Gain	10dB	15dB	15dB
Noise figure	2.9-4.8dB	8-10dB	4.6-5.1dB
Amplitude variation vs. f	±1dB	±0.4dB	±1dB
Delay resolution	15ps	14ps	2ps
Maximum delay	225ps	550ps	225ps
Power consumption	40mA@1.5V	50mA@1.8V	5.4mA@1.5V
Complete 4-channel performance			
Beam direction resolution	3.5bit	4.7bit	5.2bit
Bandwidth	18G	3G	10G
Power consumption	370mA@1.5V	250mA@1.8V	180mA@1.5V
Die area	10mm^2	1mm^2	1.44mm^2

CHAPTER 6 **CONCLUSION AND FUTURE WORK**

6.1. Conclusion

This thesis presents research on IR-UWB focuses on three aspects. The first one studies the sub 1 GHz UWB transceiver. The second focuses on 3-5 GHz UWB beamforming transmitter design. The third one investigates the 0.1-10 GHz beamforming receiver.

For sub 1 GHz UWB transceiver, we propose auto threshold detection to eliminate the manual threshold tuning that commonly plagues OOK IR-UWB. Implemented in 0.35 μm, it achieves 100 pJ/bit during transmission and 600 pJ/bit during receiving.

For UWB beamforming transmitter design, we propose relative delay approach both to enhance phase resolution and to minimize power consumption. Novel $\Delta\Sigma$ DLL based calibration is proposed which achieves fast calibration time. PSDC is also proposed to allow automatic spectrum tuning. The transmitter achieves good energy efficiency of 10 pJ/bit.

For UWB beamforming receiver design, we propose Q-compensated inductors with current reuse LNA and buffers. The maximal delay difference for the 4-channel beamforming system is about 225 ps. It occupies small area of 1.44 mm^2, about 7 times smaller than other passive beamformer.

6.2. Future Work

The sub 1 GHz UWB transceiver was tested with ECG recording chips connected by cables. In the future, these two systems could be integrated together on the same chip. Then the system size will be much more compact. The overall cost will also be much smaller.

The beamforming transmitter is realized as 4-channel linear array. To increase the scanning ability to two dimension (2-D), planar array could be designed in the future. 2-D UWB beamforming is attractive for imaging radar. However, to design planar phase array, much more complicated delay control between different channels is needed.

The beamforming receiver has been taped out. It has to be tested in the future.

Reference

[1] X. Zou, X. Xu, L. Yao, and Y. Lian, "A 1-V 450-nW fully integrated programmable biomedical sensor interface chip," *IEEE Journal of Solid-State Circuits*, vol. 44 no. 4, pp. 1067-1077, 2009.

[2] W.S. Liew, X. Zou, and Y. Lian. "A 0.5-V 1.13-µW/channel neural recording interface with digital multiplexing scheme," *Proceedings of European Solid-State Circuits Conference (ESSCIRC)*, pp. 219-222, 2011.

[3] S. Min, S. Shashidharan, M. Stevens, T. Copani, S. Kiaei, B. Bakkaloglu, and S. Chakraborty. "A 2mW CMOS MICS-band BFSK transceiver with reconfigurable antenna interface," *Radio Frequency Integrated Circuits Symposium (RFIC), 2010 IEEE*, pp. 289-292, 2010.

[4] "*First report and order: Revision of part 15 of the commission's rules regarding ultra-wideband transmission systems*", Federal Communications Commission, Government Printing Office, Washington, DC, ET Docket. pp. 98-153.

[5] I. Aoki, S.D. Kee, D.B. Rutledge, and A. Hajimiri, "Fully integrated CMOS power amplifier design using the distributed active-transformer architecture," *IEEE Journal of Solid-State Circuits*, vol. 37 no. 3, pp. 371-383, Mar. 2002.

[6] A. Natarajan, A. Komijani, X. Guan, A. Babakhani, and A. Hajimiri, "A 77 GHz phased-array transceiver with on-chip antennas in silicon: transmitter and local LO-path phase shifting," *IEEE Journal of Solid-State Circuits*, vol. 41 no. 12, pp. 2807-2819, 2006.

[7] J. Roderick, H. Krishnaswamy, K. Newton, and H. Hashemi, "Silicon-based ultra-wideband beam-forming," *IEEE Journal of Solid-State Circuits*, vol. 41 no. 8, pp. 1726-1739, 2006.

[8] A. Hajimiri, H. Hashemi, A. Natarajan, X. Guan, and A. Komijani, "Integrated phased array systems in silicon," *Proceedings of the IEEE*, vol. 93 no. 9, pp. 1637-1655, 2005.

[9] A. Natarajan, A. Komijani, and A. Hajimiri, "A fully integrated 24-GHz phased-array transmitter in CMOS," *IEEE Journal of Solid-State Circuits*, vol. 40 no. 12, pp. 2502-2514, 2005.

[10] H. Hashemi, X. Guan, and A. Hajimiri. "A fully integrated 24 GHz 8-path phased-array receiver in silicon," *IEEE International Solid-State Circuits Conference (ISSCC)*, pp. 390-392, 2004.

[11] T.S. Chu, J. Roderick, and H. Hashemi, "An integrated ultra-wideband timed array receiver in 0.13 μm CMOS using a path-sharing true time delay architecture," *IEEE Journal of Solid-State Circuits*, vol. 42 no. 12, pp. 2834-2850, 2007.

[12] F. Zhang, A. Jha, R. Gharpurey, and P. Kinget, "An agile, ultra-wideband pulse radio transceiver with discrete-time wideband-IF," *IEEE Journal of Solid-State Circuits*, vol. 44 no. 5, pp. 1336-1351, 2009.

[13] Y. Zheng, S.X. Diao, C.W. Ang, Y. Gao, F.C. Choong, Z. Chen, . . . C. Heng. "A 0.92/5.3 nJ/b UWB impulse radio SoC for communication and localization," *IEEE International Solid-State Circuits Conference (ISSCC)*, pp. 230-231, 2010.

[14] S. Soldà, M. Caruso, A. Bevilacqua, A. Gerosa, D. Vogrig, and A. Neviani, "A 5 Mb/s UWB-IR Transceiver Front-End for Wireless Sensor Networks in 0.13 μm CMOS," *IEEE journal of solid-state circuits*, vol. 46 no. 7, pp. 1636-1647, 2011.

[15] V.V. Kulkarni, M. Muqsith, K. Niitsu, H. Ishikuro, and T. Kuroda, "A 750 Mb/s, 12 pJ/b, 6-to-10 GHz CMOS IR-UWB transmitter with embedded on-chip antenna," *IEEE Journal of Solid-State Circuits*, vol. 44 no. 2, pp. 394-403, 2009.

[16] D. Lachartre, B. Denis, D. Morche, L. Ouvry, M. Pezzin, B. Piaget, . . . P. Vincent. "A 1.1 nj/b 802.15. 4a-compliant fully integrated uwb transceiver in

0.13μm cmos," *IEEE International Solid-State Circuits Conference (ISSCC)*, pp. 312-313,313 a, 2009.

[17] P.P. Mercier, D.C. Daly, and A.P. Chandrakasan, "An energy-efficient all-digital UWB transmitter employing dual capacitively-coupled pulse-shaping drivers," *IEEE Journal of Solid-State Circuits*, vol. 44 no. 6, pp. 1679-1688, 2009.

[18] M. Tabesh, J. Chen, C. Marcu, L. Kong, S. Kang, A.M. Niknejad, and E. Alon, "A 65 nm CMOS 4-element sub-34 mW/element 60 GHz phased-array transceiver," *IEEE Journal of Solid-State Circuits*, vol. 46 no. 12, pp. 3018-3032, 2011.

[19] K. Raczkowski, W. De Raedt, B. Nauwelaers, and P. Wambacq. "A wideband beamformer for a phased-array 60GHz receiver in 40nm digital CMOS," *IEEE International Solid-State Circuits Conference (ISSCC)*, pp. 40-41, 2010.

[20] S. Kishimoto, N. Orihashi, Y. Hamada, M. Ito, and K. Maruhashi. "A 60-GHz band CMOS phased array transmitter utilizing compact baseband phase shifters," *Radio Frequency Integrated Circuits Symposium (RFIC)*, pp. 215-218, 2009.

[21] A. Valdes-Garcia, S.T. Nicolson, J.W. Lai, A. Natarajan, P.Y. Chen, S.K. Reynolds, . . . B. Floyd, "A fully integrated 16-element phased-array transmitter in SiGe BiCMOS for 60-GHz communications," *IEEE Journal of Solid-State Circuits*, vol. 45 no. 12, pp. 2757-2773, 2010.

[22] A. Natarajan, A. Komijani, and A. Hajimiri. "A 24 GHz phased-array transmitter in 0.18 μm CMOS," *IEEE International Solid-State Circuits Conference (ISSCC)*, pp. 212-594 Vol. 1, 2005.

[23] M.Y.W. Chia, T.H. Lim, J.K. Yin, P.Y. Chee, S.W. Leong, and C.K. Sim, "Electronic beam-steering design for UWB phased array," *IEEE Transactions on Microwave Theory and Techniques*, vol. 54 no. 6, pp. 2431-2438, 2006.

[24] H. Hashemi, X. Guan, A. Komijani, and A. Hajimiri, "A 24GHz SiGe Phased-Array Receiver - LO Phase Shifting Approach," *IEEE TMTT*, vol. 53 no. 2, pp. 614-626, Feb., 2005.

[25] T.S. Chu and H. Hashemi. "A CMOS UWB camera with 7x7 simultaneous active pixels," *IEEE International Solid-State Circuits Conference (ISSCC)*, pp. 120-121, February, 2008.

[26] S.K. Garakoui, E.A.M. Klumperink, B. Nauta, and F.F.E.V. Vliet. "A 1-to-2.5GHz Phased-Array IC Based on gm-RC All-Pass Time-Delay Cells," *IEEE International Solid-State Circuits Conference (ISSCC)*, pp. 80-82, 2012.

[27] S. Gueorguiev, S. Lindfors, and T. Larsen, "A 5.2 GHz CMOS I/Q modulator with integrated phase shifter for beamforming," *IEEE Journal of Solid-State Circuits*, vol. 42 no. 9, pp. 1953-1962, 2007.

[28] M. Fakharzadeh, M.R. Nezhad-Ahmadi, B. Biglarbegian, J. Ahmadi-Shokouh, and S. Safavi-Naeini, "CMOS phased array transceiver technology for 60 GHz wireless applications," *IEEE Transactions on Antennas and Propagation*, vol. 58 no. 4, pp. 1093-1104, 2010.

[29] I.D. O'Donnell and R.W. Brodersen. "A 2.3 mW baseband impulse-UWB transceiver front-end in CMOS," *Symposium on VLSI Circuits.* , pp. 200-201, 2006.

[30] C.H. Yang, K.H. Chen, and T.D. Chiueh. "A 1.2 V 6.7 mW impulse-radio UWB baseband transceiver," *IEEE International Solid-State Circuits Conference (ISSCC)*, pp. 442-608 Vol. 1, 2005.

[31] A. Mazzanti, M.B. Vahidfar, M. Sosio, and F. Svelto. "A reconfigurable demodulator with 3-to-5GHz agile synthesizer for 9-band WiMedia UWB in 65nm CMOS," *IEEE International Solid-State Circuits Conference(ISSCC)*, pp. 412-413,413 a, 2009.

[32] L. Zhou, Z. Chen, C.-C. Wang, F. Tzeng, V. Jain, and P. Heydari. "A 2gbps rf-correlation-based impulse-radio uwb transceiver front-end in 130nm cmos," *Radio Frequency Integrated Circuits Symposium (RFIC)*, pp. 65-68, 2009.

[33] J. Keignart, N. Daniele, and P. Rouzet. "UWB channel modeling contribution from CEA-LETI and STMicroelectronics," *IEEE P802.15 Working Group for WPANs*, pp. NA, 2002.

[34] A.F. Molisch, "Ultrawideband propagation channels-theory, measurement, and modeling," *IEEE Trans.Veh. Technol.*, vol. 54 no. 5, pp. 1528-1545, 2005.

[35] C. Hu, R. Khanna, J. Nejedlo, K. Hu, H. Liu, and C.P. Y., "A 90 nm-CMOS, 500 Mbps, 3–5 GHz Fully-Integrated IR-UWB Transceiver With Multipath Equalization Using Pulse Injection-Locking for Receiver Phase Synchronization," *IEEE Journal of Solid-State Circuits*, vol. 46 no. 5, pp. 1076-1088, 2011.

[36] F.S. Lee, D.D. Wentzloff, and A.P. Chandrakasan. "An ultra-wideband baseband front-end," *Radio Frequency Integrated Circuits Symposium (RFIC)*, pp. 493-496, 2004.

[37] T.H. Lee, *The design of CMOS radio-frequency integrated circuits*2004: Cambridge university press.

[38] Y. Moon, J. Choi, K. Lee, D.K. Jeong, and M.K. Kim, "An all-analog multiphase delay-locked loop using a replica delay line for wide-range operation and low-jitter performance," *IEEE Journal of Solid-State Circuits*, vol. 35 no. 3, pp. 377-384, 2000.

[39] R. Kreienkamp, U. Langmann, C. Zimmermann, T. Aoyama, and H. Siedhoff, "A 10-Gb/s CMOS clock and data recovery circuit with an analog phase interpolator," *IEEE Journal of Solid-State Circuits*, vol. 40 no. 3, pp. 736-743, 2005.

[40] S.J. Cheng, L. Qiu, Y. Zheng, and C.H. Heng, "50–250 MHz ΔΣ DLL for Clock Synchronization," *IEEE Journal of Solid-State Circuits*, vol. 45 no. 11, pp. 2445-2456, 2010.

[41] A. Efendovich, Y. Afek, C. Sella, and Z. Bikowsky, "Multifrequency zero-jitter delay-locked loop," *IEEE Journal of Solid-State Circuits*, vol. 29 no. 1, pp. 67-70, 1994.

[42] R.J. Yang and S.I. Liu, "A 40–550 MHz harmonic-free all-digital delay-locked loop using a variable SAR algorithm," *IEEE Journal of Solid-State Circuits*, vol. 42 no. 2, pp. 361-373, 2007.

[43] T. Atit, I. Hiroki, I. Koichi, T. Makoto, and S. Takayasu. "1-V 299μW flashing UWB transceiver based on double thresholding scheme," *Symposium on VLSI Circuits*, pp. 202-203, 2006.

[44] T. Terada, S. Yoshizumi, M. Muqsith, Y. Sanada, and T. Kuroda, "A CMOS ultra-wideband impulse radio transceiver for 1-Mb/s data communications and±2.5-cm range finding," *IEEE Journal of Solid-State Circuits*, vol. 41 no. 4, pp. 891-898, 2006.

[45] C. Kim and S. Nooshabadi. "A DTR UWB transmitter/receiver pair for wireless endoscope," *IEEE Asian Solid-State Circuits Conference (A-SSCC)*, pp. 357-360, 2009.

[46] S. Patnaik, N. Lanka, and R. Harjani. "A dual-mode architecture for a phased-array receiver based on injection locking in 0.13μm CMOS," *IEEE International Solid-State Circuits Conference (ISSCC)*, pp. 490-491,491 a, 2009.

[47] M. Maymandi-Nejad and M. Sachdev, "A monotonic digitally controlled delay element," *IEEE Journal of Solid-State Circuits*, vol. 40 no. 11, pp. 2212-2219, 2005.

[48] H.H. Chang, J.W. Lin, C.Y. Yang, and S.I. Liu, "A wide-range delay-locked loop with a fixed latency of one clock cycle," *IEEE Journal of Solid-State Circuits*, vol. 37 no. 8, pp. 1021-1027, 2002.

[49] J.G. Maneatis, "Low-jitter process-independent DLL and PLL based on self-biased techniques," *IEEE Journal of Solid-State Circuits*, vol. 31 no. 11, pp. 1723-1732, 1996.

[50] Z. Safarian, T.S. Chu, and H. Hashemi. "A 0.13μm CMOS 4-channel UWB timed array transmitter chipset with sub-200ps switches and all-digital timing circuitry," *Radio Frequency Integrated Circuits Symposium (RFIC)*, pp. 601-604, 2008.

[51] F. Bruccoleri, E.A. Klumperink, and B. Nauta, "Wide-band CMOS low-noise amplifier exploiting thermal noise canceling," *IEEE Journal of Solid-State Circuits*, vol. 39 no. 2, pp. 275-282, 2004.

[52] S.C. Blaakmeer, E.A. Klumperink, D.M. Leenaerts, and B. Nauta, "Wideband balun-LNA with simultaneous output balancing, noise-canceling and distortion-canceling," *IEEE Journal of Solid-State Circuits*, vol. 43 no. 6, pp. 1341-1350, 2008.

[53] K.-H. Chen and S.-I. Liu, "Inductorless wideband CMOS low-noise amplifiers using noise-canceling technique," *IEEE Transactions on Circuits and Systems I*, vol. 59 no. 2, pp. 305-314, 2012.

[54] S. Blaakmeer, E. Klumperink, B. Nauta, and D. Leenaerts. "An inductorless wideband balun-LNA in 65nm CMOS with balanced output," *33rd European Solid State Circuits Conference (ESSCIRC)*, pp. 364-367, 2007.

[55] H. Wang, L. Zhang, and Z. Yu, "A wideband inductorless LNA with local feedback and noise cancelling for low-power low-voltage applications," *IEEE Transactions on Circuits and Systems I*, vol. 57 no. 8, pp. 1993-2005, 2010.

[56] Q. Li and Y.P. Zhang, "A 1.5-V 2–9.6-GHz inductorless low-noise amplifier in 0.13-μm CMOS," *IEEE Transactions on Microwave Theory and Techniques*, vol. 55 no. 10, pp. 2015-2023, 2007.

[57] M. Okushima, J. Borremans, D. Linten, and G. Groeseneken. "A DC-to-22 GHz 8.4 mW compact dual-feedback wideband LNA in 90 nm digital CMOS," *IEEE Radio Frequency Integrated Circuits Symposium (RFIC)*, pp. 295-298, 2009.